ABSTRACT

Title of Thesis:	EVALUATION OF THE THERMOPHYSICAL PROPERTIES OF POLY(METHYL METHACRYLATE): A REFERENCE MATERIAL FOR THE DEVELOPMENT OF A FLAMMABILITY TEST FOR MICRO-GRAVITY ENVIRONMENTS
Degree Candidate:	Dipl.-Ing. Thomas Steinhaus
Degree and Year:	Masters of Science, 1999
Thesis Directed by:	Dr. Jose L. Torero, Assistant Professor Department of Fire Protection Engineering

A study has been conducted using PMMA (Poly(methyl methacrylate)) as a reference material in the development process of the Forced Flow and flame Spread Test (FIST). This test attempts to establish different criteria for material flammability for micro-gravity environments. The FIST consists of two tests, ignition and flame spread tests, that provide a series of material “fire” properties that jointly provide important information on the flammability of a material. This work deals with the former. PMMA was chosen as a reference material mainly because of its well characterized properties.

Evaluation of the ignition delay time as a function of a suddenly imposed external heat flux can be described by the following expression:

$$\frac{1}{\sqrt{t_{ig}}} = \frac{2}{\sqrt{\pi}} \frac{a}{\sqrt{\lambda \rho c_p}} \left(T_{ig} - T_{\infty}\right)$$

where the time t_{ig} is the measured ignition delay time and T_{ig} the minimum surface temperature at which piloted ignition can occur. The ignition temperature T_{ig} can be obtained from the experimental determination of a critical heat flux for ignition and the total convective heat transfer coefficient. And by assuming the absorptivity ("a") to be approximately unity, a material constant can be found, and is often referred to as the thermal inertia $\lambda \rho c_p$.

The ignition temperature T_{ig} is addressed by splitting the ignition process into the time required to initiate thermal decomposition of the material (t_p occurring at T_p) and the ignition delay time (t_{ig} occurring at T_{ig}).

The present work provides an independent evaluation of the evolution of the thermal properties ($\lambda \rho c_p$) of PMMA, as a function of temperature. The thermophysical properties ($\lambda \rho c_p$) were determined by using the time to ignition t_{ig} and time to pyrolysis t_p approached as obtained from the FIST. Discrepancies between these two approaches were resolved by defining a mixing time, t_m and a minimum average fuel

concentration for ignition, $Y_{f,L}$. Independent evaluation of the density, thermal conductivity and specific heat serve to correlate the values of $\lambda\rho c_p$ obtained from the FIST.

EVALUATION OF THE THERMOPHYSICAL PROPERTIES OF POLY(METHYL METHACRYLATE): A REFERENCE MATERIAL FOR THE DEVELOPMENT OF A FLAMMABILITY TEST FOR MICRO-GRAVITY ENVIRONMENTS

by

Dipl.-Ing. Thomas Steinhaus

Thesis submitted to the faculty of the Graduate School of the
University of Maryland at College park in partial fulfillment
Of the requirements for the degree of
Masters of Science
1999

Advisory Committee:

Professor Jose L. Torero, Chair
Professor James G. Quintiere
Professor James A. Milke

ACKNOWLEDGEMENTS

The past $1\frac{1}{2}$ years that I have spent in the United States to follow my research interests is finally coming to an end with the presentation of this study. Recounting that time makes me realize the tremendous experience I have gained while studying and working at the University of Maryland. The people to whom I want to express my gratitude had a great influence on that time and therefore deeply impacted my life. The first person I want to thank is Jose L. Torero. The opportunity he presented to me, as well as the guidance and friendship he gave me in that time is incredible. In my own words I would call it "unheimlich". I wish the world could be filled with these people, but unfortunately that is not the case. Secondly, I would like to thank my family for their encouragement in my wish to study abroad and their continued support for my education. Special thanks go to Alvaro Sifuentes, for his hard work, and the pleasure I had working with him. Finally, I want to mention those people who contributed in many different ways: Amalia, Anne, Brenda, Bryce, David, Dennis, Father Bob, Gilles (F), Grunda (N), Mark, Melissa, Michael (GB), Michele, The Mother Shippers & Co., Dr. J. Quintere, Rick, Santiago, Stephen, Thomas (D).

This work was funded by NASA Glenn Research Center under grant NAG-31961. I would like to recognize the support of Dr. Howard Ross.

TABLE OF CONTENTS

LIST OF TABLES

LIST OF FIGURES

NOMENCLATURE

Roman Letters		
Symbol	**Units**	**Description**
a / a_{λ}		Absorptance / Absorptance of a specified wavelength
a		Called the exponent of Mark-Houwink
A		Constant
c	$\frac{m}{s}$	Velocity of light
c_p	$\frac{J}{g\ K}$	Specific heat per gram
$\bar{c}_p$	$\frac{J}{g\ K}$	The mean specific heat capacity for the given temperature rise ΔT
C		Constant
C_1		Constant
C_2	$\frac{K^4 m^2}{W}$	Constant
C_p	$\frac{J}{mol\ K}$	Specific heat per mole
d	m	Sample thickness
e_1		Specific thermal expansivity for the liquid
e_g		Specific thermal expansivity for the under-cooled liquid
$\dot{E}$	$\frac{W}{m^2}$	Spectral radiant power
$\dot{E}_b$	$\frac{W}{m^2}$	Spectral radiant power of a black body
Erfc		Complement of the error function
F_{s-IR}		The view factor between the surface and the sensor
g	$\frac{m}{s^s}$	Specific gravity
h	J s	Planck's constant
h_c	$\frac{W}{m^2\ K}$	Convective Heat Transfer Coefficient

Roman Letters		
Symbol	**Units**	**Description**
h_m	kg/m^2s	Convective Mass transfer Coefficient
h_r	$\frac{W}{m^2\ K}$	Radiative Heat Transfer Coefficient (linearized)
h_t	$\frac{W}{m^2\ K}$	Total Heat Transfer Coefficient ($h_c + h_r$)
H_c	$\frac{J}{g}$	Heats of crystallization
H_f	$\frac{J}{g}$	Heats of melting
i		Polymer chain type
$I_{b,\lambda,T}$	$\frac{W}{m}$	Spectral radiant emittance of a black body
k		Constant
k	$\frac{J}{K}$	Boltzmann's constant
L	m	Characteristic Length Scale
L_v	$\frac{kJ}{g}$	Heat of Vaporization (kJ/g)
$L[\ ]$		Laplace Transformation
$\dot{m}_o^{'}$	$\frac{kg}{m\ s}$	Mass Flow Rate of Oxidizer per unit length
$\dot{m}_o^{''}$	$\frac{kg}{m^2\ s}$	Mass Flow Rate of Oxidizer per unit area
$\dot{m}_f^{'}$	$\frac{kg}{m\ s}$	Mass Flow Rate of Fuel per unit length
$\dot{m}_f^{''}$	$\frac{kg}{m^2\ s}$	Mass Flow Rate of Fuel per unit area
M	$\frac{kg}{kmol}$	Molecular weight
M_n	$\frac{kg}{kmol}$	Number average molecular weight
M_v	$\frac{kg}{kmol}$	Viscosity Molecular Weight Average

Roman Letters		
Symbol	**Units**	**Description**
M_w	$\frac{kg}{kmol}$	Weighted Molecular Weight Average
n	kmol	Number of chains
N		Total number of chains
p	$\frac{N}{m^2}$	Pressure
Pr		Prandtl Number
$\dot{q}$	W	Heat flux
$\dot{q}''_{i,cri}$	$\frac{kW}{m^2}$	Incident critical Heat Flux
$\dot{q}''_i$	$\frac{kW}{m^2}$	Incident Heat flux
$\dot{q}''_{IR}$	$\frac{kW}{m^2}$	Energy seen by the IR sensor
$\dot{q}''_{net}$	$\frac{kW}{m^2}$	Net heat flux
$\dot{q}''_s$	$\frac{kW}{m^2}$	Net surface heat flux at the surface
$\dot{Q}$	W	time rated heat flow
r / r_λ		Reflectance / reflectance of a specified wavelength
s		Laplace variable
t	s	Time
t / t_λ		Transmittance / transmittance of a specified wavelength
t_c	s	Characteristic time
t_{ig}	s	Ignition delay time
t_p	s	Pyrolysis time
t_m	s	Mixing time
t_i	s	Induction time
T	K or °C	Temperature
T_s	K or °C	Surface Temperature
T_{ig}	K or °C	Ignition Temperature
T_m	K or °C	Melting temperature
T_d	K or °C	Ultimate decomposition temperature
$\overline{T}$	K or °C	Characteristic temperature

Roman Letters		
Symbol	**Units**	**Description**
T_{∞}	K or °C	Ambient temperature
T_c	K or °C	Crystallization temperature
T_p	K or °C	Pyrolysis Temperature
ΔT	K or °C	Temperature rise
T_{s-IR}	K or °C	Surface Temperature measured by the infrared camera
T_g	K or °C	Glass transition temperature
U	$\frac{\sqrt{m}}{s}$	Constant
u	$\frac{m}{s}$	Velocity
u_c	$\frac{m}{s}$	Characteristic Velocity
V	m^3	Volume
ΔV_m	m^3	Melt expansion
w_i	kg	Total weight of an individual type of chain.
W	kg	Total weight
x		Cartesian coordinate
X		Property mass
X_{∞}		asymptotic value at very high molecular
y		Cartesian coordinate
Y_f		Fuel Mass fraction
$Y_{f,L}$		Lean Lower Flammability Limit Fuel Mass fraction
$Y_{f,stoic}$		Stoichiometric Fuel Mass fraction
z		Cartesian coordinate

Greek Letters		
Symbol	**Units**	**Description**
α	$\frac{m^2}{s}$	Thermal Diffusivity
β	$\frac{1}{K}$	Thermal expansion coefficient

Greek Letters		
Symbol	**Units**	**Description**
δ	m	Momentum Boundary Layer Thickness
$\delta(t)$	m	Thermal Penetration Distance
δ_t	m	Thermal Boundary Layer thickness
θ		Modified Temperature
$\overline{\theta}$		Transformed Temperature
$\varepsilon / \varepsilon_\lambda$		Emissivity / Emissivity of a specified wavelength
λ	$\frac{W}{m\,K}$	Thermal Conductivity
$\lambda \rho c_p$	$\frac{W^2 s}{m^4\,K^2}$	Thermal Inertia
ν	$\frac{m^2}{s}$	Kinematic Viscosity
ρ	$\frac{kg}{m^3}$	Density
σ		Stefan-Boltzmann Constant
η		Similarity Variable
τ	S	Time $t \geq t_p$
τ^*	s	Time shift

1. Introduction

The basic motivation for this work is are the raised safety issues that an accidentally occurring fire in a space-based facility poses on humans and equipment during long term space missions. Long term space missions, planned and currently conducted, such as the International Space Station (ISS), the Human Mission to Mars and other space facilities, are being designed with a life expectancy of 20 to 30 years. Knowing the given fact that there are combustible materials and sources of ignition present in theses space facilities, the probability of an accidental occurring fire in a space vehicle can not be disregarded [PalH-87, FaeG-89]. Furthermore, the enclosed nature of space facilities, their strong dependency on electronic components and their sensitivity towards products of combustion (radiation, particles, gases, etc.) leads to conclude that even a small fire will have tremendous impact and will cause serious damage to the facility. For all the above reasons, it is of critical importance to characterize and evaluate well, in what relates to their fire properties, materials which will be used in these space facilities.

The use of bench-scale standard test methods for the assessment of the material flammability, and their uses in real world scenarios, has been a subject of debate for many years [QuHH-86]. The literature shows that when evaluating different tests one can see, that no single test can determine the potential of a material to sustain a fire. Furthermore, it can be argued whether or not, for most fire scenarios, realistic scale tests such as the room corner test, are necessary to assess the fire performance of materials

[WilR-76]. Nevertheless, numerous attempts have been made to find a correlation between standard test results and the actual behavior of a fire [ParW-82, QuiJ-82, QuHW-83]. In most cases it has been shown, that complementary tests together with an adequate interpretation of the results are needed to properly assess the relationship between test results (from bench and full scale tests) and material behavior in a real fire scenario.

The "Flammability, Odor, Offgassing, and Compatibility Requirements Test Procedures for Materials in Environments that Support Combustion" is a NASA specification [NASA-81], that states the necessary flammability characteristics of all materials which are used in space vehicles or facilities. This document specifies that all materials, before they are qualified for the use in a space vehicle, are subjected to two tests. Those two tests are the:

1. Upward Flame Propagation Test and
2. Heat and Visible Smoke Release Rates Test.

Those two tests are expected to properly assess the flammability of a material under micro-gravity conditions. Growing controversy on the capability of these tests to properly assess material flammability is arising. The flammability assessment according to NASA specifications [NASA-81] focuses on the following basic principles:

A Attempting to provide a worst case scenario for the tested materials (Test 1),

B Measure heat release rate of the fuel (Test 2), and

C Thus attempt to define the "damage potential" of a fire.

The objective of the **"Upward Flame Propagation Test"** is to determine whether or not a test material, when exposed to a standard ignition source, will self extinguish and will not create burning debris, which than can ignite adjacent materials [NASA-81]. As it was mentioned above, theses tests shall be conducted under the worst case scenario (e.g. worst-case thickness and environment). Therefore the upward flame spread test was assumed to be the worst case scenario, where the flames coming from the burn region cover and preheat the surface of the test specimen above the burn area. The worst case material thickness, dependents on a combustibility study, with which the mounting conditions are chosen, so they meet the worst case criteria. Furthermore, the environmental oxygen concentration is chosen to meet the concentrations found in a spacecraft, which can be above and below that of the ambient oxygen concentrations. In the upward flame propagation test no forced flow is considered. The oxygen entrainment towards the flame is therefore only driven by buoyancy. The passing criteria for this test is, when a sample material is subjected to an ignition source, to self extinguish before propagation has reached 6 inches or ~15 cm. Everything longer means that the material has failed the test.

As inferred above, several factors make this test questionable, where the first is related to principal "A", "Attempting to provide a worst case scenario for the tested

materials (Test 1),". The question is, whether or not the upward flame spread really describes the most hazardous conditions encountered. It has been shown [OhVi-91] that test materials, which pass the upward flame propagation test would fail if they are exposed to an external radiant flux. A material exposed to an external heat source, such as that from an overheated electrical conductor, motor, lamp, etc., describes that case, in which the material would burn more readily due to the external radiation which preheats the material.

The objective of the **"Heat and Visible Smoke Release Rates Test"** is to provide supplemental information on the flammability of those materials that fail to meet the criteria of the upward flame propagation test. Furthermore this test is also required for non-metals that have an area greater than 4 ft^2 or 0.37 m^2 exposed to habitable environments on board of a spacecraft [NASA-81]. The objectives and test protocol correspond to those defined in the "Cone Calorimeter Test" (ASTM-E1354 or ISO5660). Extensive information about this test and its potential can be found in the literature e.g. [BaGr-92].

A detailed description of both above described test methods is provided in the NASA specification NASA-NHB 8060.1 [NASA-81], while an extensive list of tested the materials is provided in the "Materials Selection List for Space Hardware Systems" [MSFC-98].

Micro-gravity and normal gravity present significantly different conditions for a fire scenario. In normal gravity the natural convection is always present guaranteeing a minimum flow around the flame, even if the flame is small. In micro-gravity, the lack of buoyancy allows very low flow velocities around a flame. It is common for spacecraft HVAC systems to generate velocities no greater than 0.1 m/s. Under these conditions flames very often occur in a laminar form, which is different on earth, where most flames will become turbulent as the size of the fire increases.

Material testing should be representative of the conditions present in space facilities, mainly micro-gravity. The development of a new test methodology, the Forced flow Ignition and Flame Spread Test (FIST), that will attempt to provide more comprehensive information on material flammability for spacecraft applications represents the context for this work. The initial step in this development was the identification of an appropriate test method followed by different length scale considerations [LonR-98]. In that work, the effect of scale reduction on piloted ignition of PMMA (poly(methyl methacrylate)) is addressed by using the Lateral Ignition and Flame spread Test (LIFT) apparatus (ASTM E1321), and than develop a new flammability apparatus named FIST.

The overall objective of this research effort is to study poly(methyl methacrylate) as a reference material. This work will provide the background to better understand flammability characteristics of materials. The evaluation of the thermophysical properties of poly(methyl methacrylate) is conducted. These properties

are determined experimentally following the FIST methodology and through an extensive literature review.

In Chapter 2 the Methodology chapter, the methodology is described, how the mass and temperature versus time curves, pyrolysis time t_p and pyrolysis temperature T_p for different incident heat fluxes $\dot{q}''_i$ were obtained. Chapter 3 provides the theoretical background, for the Ignition Theory, Thermography, and Least Square Best Fit Analysis, which are essential for conducting this research as well as for the later analysis. Chapter 4, gives a broad introduction into the Material Properties of poly(methyl methacrylate), where the main focus lies on the determination of the thermophysical properties λ (thermal conductivity), ρ density, and c_p specific heat dependant on temperature. Chapter 5 analysis the acquired data and Chapter 6 provides some brief conclusions.

2. Methodology

Two test apparatus were used to determine the temperature evolution with time of the surface of a PMMA sample to a constant external heat flux. The main objective is to establish a criteria to identify the temperature for the onset of pyrolysis (T_p) and the time after sudden exposure at which it occurs (t_p). Two different temperature measurement techniques were used, infrared thermography and thermocouples, in an attempt to establish conclusive measurements of the surface temperature evolution ($T_s(t)$). The constraints imposed by the use of an infrared camera required the development of a different but equivalent experimental configuration.

2.1. Thermocouple Measurements

The experimental apparatus as presented in Figure 1 consists of a cone heater, as used in the "Oxygen Consumption Calorimeter" (ASTM E 1354) to provide an even distribution of the incident heat flux $\dot{q}''_i$. Centered underneath that cone heater the test specimen, here PMMA, was placed horizontally embedded, in an insulating material called "marinite". The insulating material, including the sample specimen, was placed on top of a scale. The purpose of the scale and, thus of the horizontal placement, is to determine the mass loss that will characterize the onset of pyrolysis.

The mechanical scale used was a model "P1200" from Mettler, which gave a precision of ±0.1g. Due to the nature of the scale, the data could not be recorded with a

computer, but was instead recorded with a video camera. It was observed that the overall mass loss in the whole process was of approximately 0.4g, therefore this scale could only produce a rough estimate of the mass evolution of the sample. Some of the preliminary data will correspond to this scale but, most of the data was obtained by means of a "Navigator Scale N02120" from Ohaus which is presented in Figure 1. This scale provided and accuracy of ±0.01g, which is more suitable for the here conducted tests and test specimen. This scale is capable of sending the weight measurements directly to a computer were they could be processed and recorded.

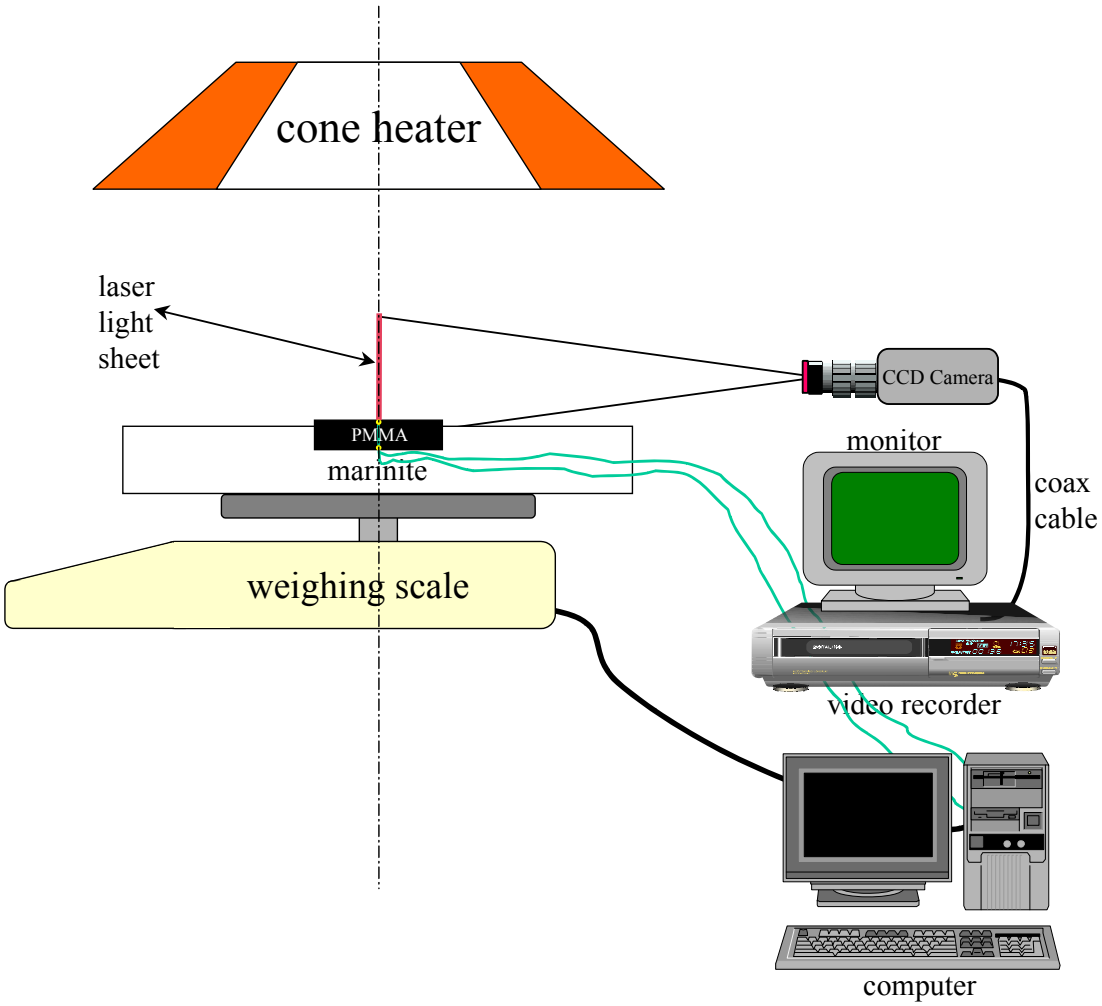

Figure 1 measurements with touching thermocouples (main view)

The determination of the onset of pyrolysis was achieved by placing a laser light sheet across the surface of the test specimen (PMMA) as shown in Figure 1 and Figure 3. This was done to illuminate particles coming out of the test specimen surface. The time where the first particles could be visualized was defined as the pyrolysis time, t_p. The (MMA) vapor emanating from the sample surface is large enough that, by means of a CCD camera, it can be detected as it emerges from the surface. The correspondence

between this observation and the actual onset of pyrolysis is not clear but it serves to define in a particular way this event, otherwise it is difficult to define.

The laser used for that purpose was a diode laser "SDL-7432 H1" from SDL. The laser provides up to 500 mW in a narrow band corresponding to 683nm. To obtain the appropriate laser light sheet, two lenses were required, as depicted in Figure 3. The diode laser does not produce a cylindrical light beam; instead, a divergent conical beam is created with a focal point somewhere inside the diode. To create a thin laser light sheet the optimal solution is to use two cylindrical lenses. One with a short focal length will be placed first and will create a beam of quasi-parallel rays in one of the directions and still divergent in the other. The second lens will attempt to correct for the divergence in the third dimension. Poor quality of the diode source does not allow for full correction, therefore the beam will only be thin in a finite region (Figure 2).

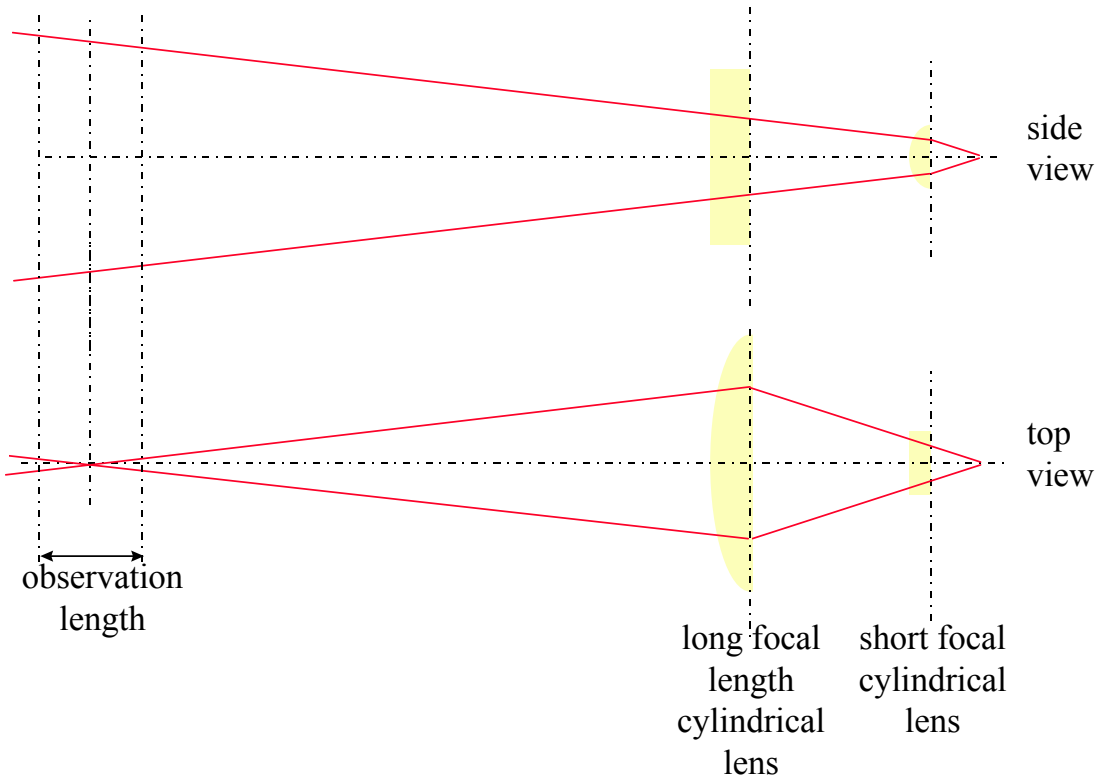

Figure 2 lens setup for laser light sheet

The CCD camera was set up perpendicular to the laser light to focus on the area of interest. The CCD output could be visualized by means of a monitor and recorded by means of a video recorder on a magnetic tape, as depicted in Figure 1. The used CCD camera was a "COHU 4915" from COHU. For better image processing and suppression of other light sources a filter that covered a wavelength band between 675 nm to 685 nm was placed in front of the camera lenses, letting only the wavelength of the used laser light through. This was done only to obtain light signals from the observation field, when vapor MMA particles crossed the laser light sheet. The time it took, from placing the sample under the cone up to the point, when particles were emanating (seen) above the test specimen (PMMA) surface was manually recorded, either direct during

the testing or later from the videotape. This time will be referred to as the pyrolysis times t_p.

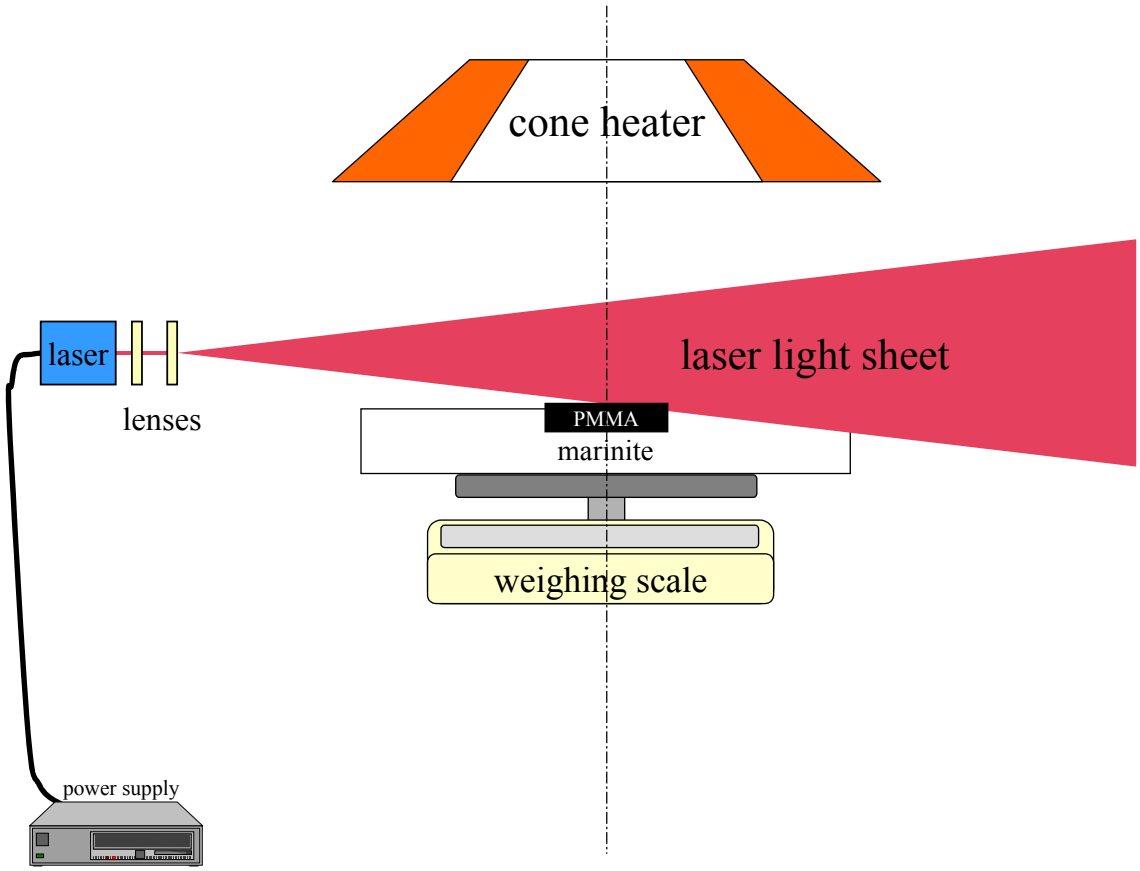

Figure 3 measurements with touching thermocouples (side view)

To obtain the temperatures at the exposed and unexposed (opposite) surface of tests specimen thermocouples were attached to and embedded in the surfaces as depicted in Figure 4 and Figure 5. Up to the test that will be labeled 79 the thermocouple placement 1, as depicted in Figure 4, was used. In that placement the thermocouple at the exposed surface was attached to the surface by carefully melting the PMMA, embedding the thermocouple into the molten PMMA so that the

thermocouple and thermocouple wires would lie slightly under the sample surface. The next step was to let the molten area cool down. The thermocouple at the unexposed surface was attached to the surface using tape.

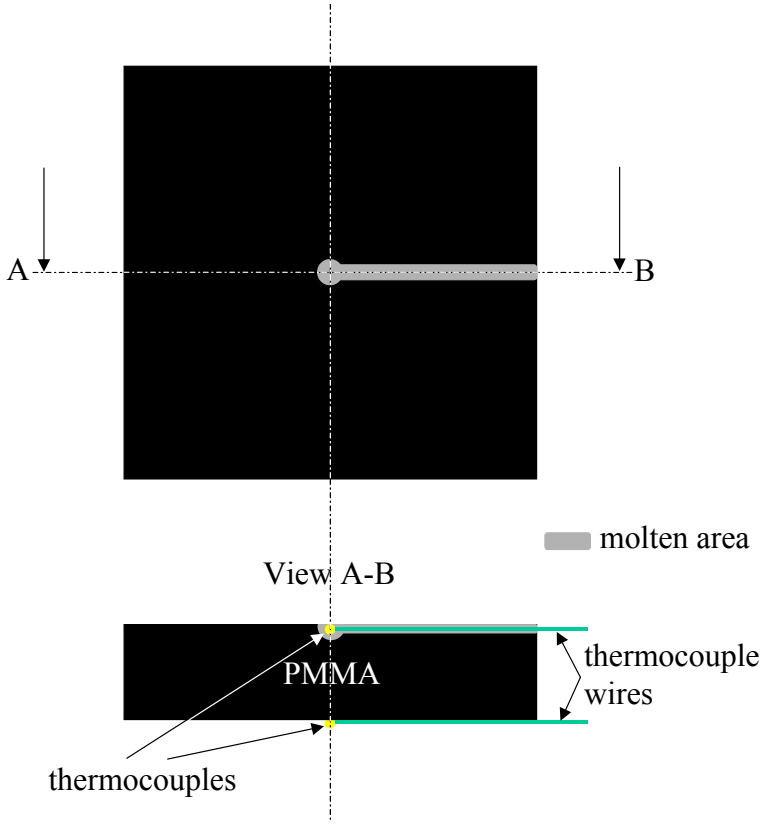

Figure 4 thermocouple placement 1

From test labeled 80 and higher, the thermocouple placement 2, as depicted in Figure 5, was used, because the thermocouple had a tendency to detach when using the thermocouple placement 1. In that placement a very small hole was drilled through the center of the PMMA sample. The thermocouple at the exposed surface placed on just underneath the surface by sticking it through the drilled hole from the unexposed surface. Then by carefully melting PMMA in the area around the thermocouple bead

and adding enough molten PMMA to embed the thermocouple under the sample surface to, so that hey were just covered with PMMA. The subsequent step was to let the molten area cool down. The thermocouple at the unexposed surface was attached as previously with tape to the back surface.

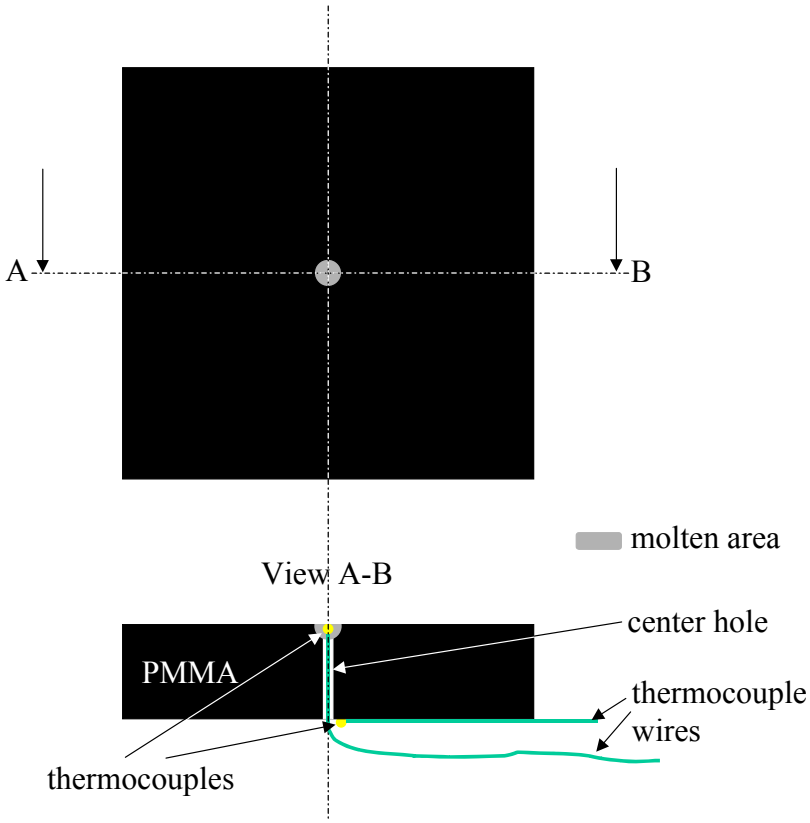

Figure 5 thermocouple placement 2

In both cases (the thermocouple placement 1 and 2) the temperature of the unexposed surface is measured to provide an estimate of the heat losses through the back of the sample (breakdown of the semi-infinite solid assumption).

The sample placement in the "maronite" sample holder can be generally done in the way, that the exposed surface of the sample is flush with the surface of the sample holder. For the conducted tests the sample surface was slightly higher than the sample holder surface (~1 mm), for easier alignment of the laser sheet and the fuel surface as shown in Figure 6.

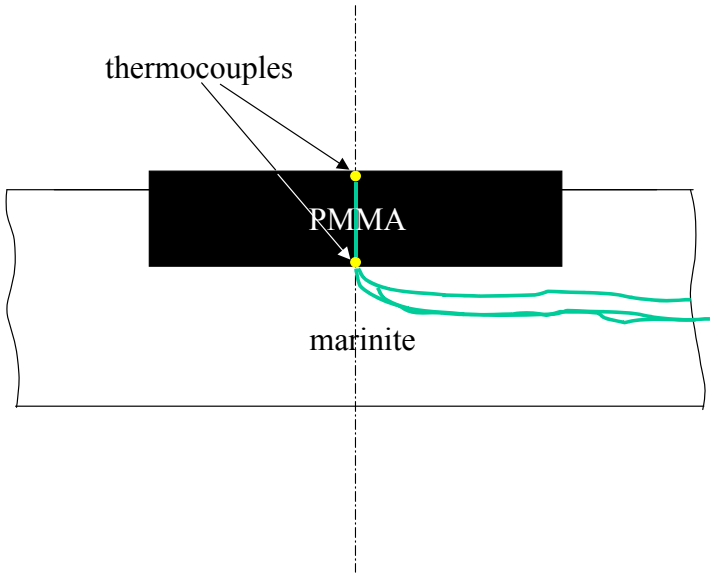

Figure 6 thermocouple placement in the test specimen PMMA

Looking at Figure 1 it can be seen, that the thermocouple wiring might disturb the weight measurements. Therefore, some of the pyrolysis tests were conducted without the thermocouples to obtain exact weight measurements. Correlating the observed pyrolysis to the temperature at the surface of the sample material leads to the pyrolysis temperature T_p.

An important value to know for the later analysis, is the incident heat flux $\dot{q}_i''$ present at the surface of the sample material. Therefore, specific precautions were made, to correctly measure the impinging incident heat flux $\dot{q}_i''$ on the surface of the sample. As it is shown in Figure 7 a heat flux meter is placed, before the actual test, underneath the cone heater, exactly at the same place were the test specimen is placed. The exact placement is achieved by using the earlier mentioned laser light sheet, which touches the sample specimen and the heat flux meter exactly in the center of both, which is also the center axis of the cone heater as depicted in Figure 3 and Figure 7. According to the desired heat flux, the voltage input to the cone heater is adjusted.

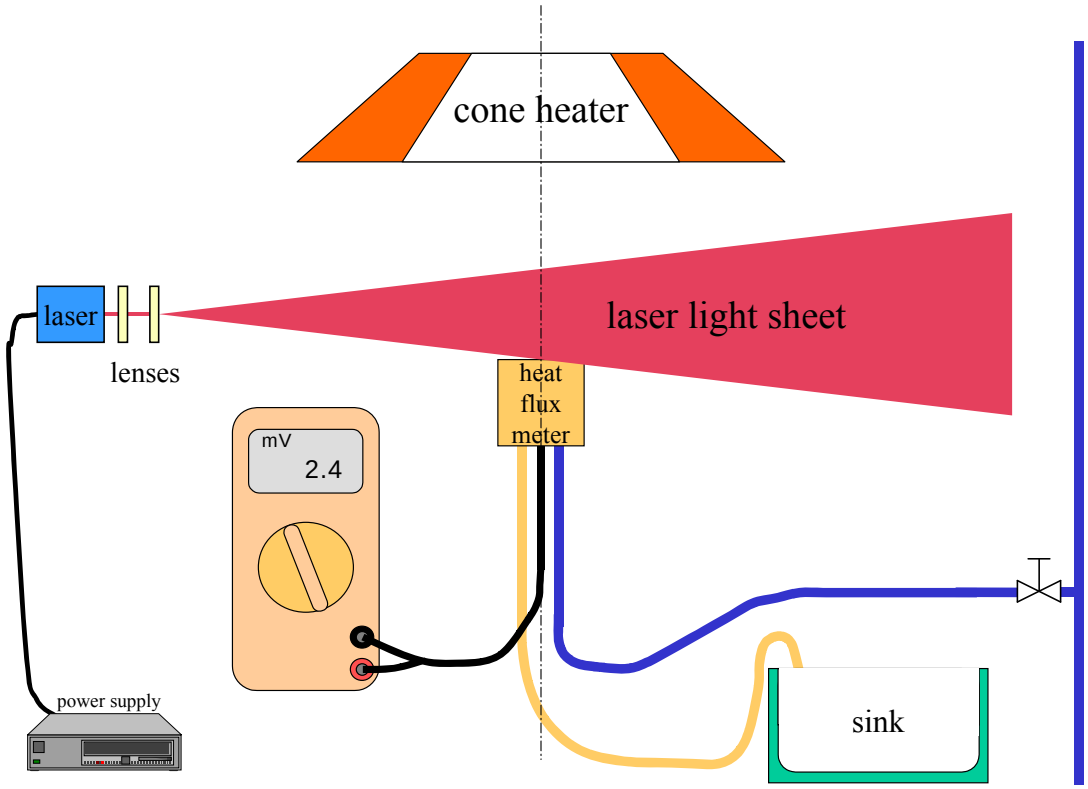

Figure 7 incident heat flux $\dot{q}_i''$ determination for the experimental apparatus measurements with touching thermocouples

The typical results for one incident heat flux $\dot{q}_i''$ from this apparatus are the

- Time dependant front (TC 1) and back (TC 2) surface temperature of the test specimen Figure 8,
- Time dependant weight Figure 9 and
- Time to pyrolysis Figure 8 and Figure 9.

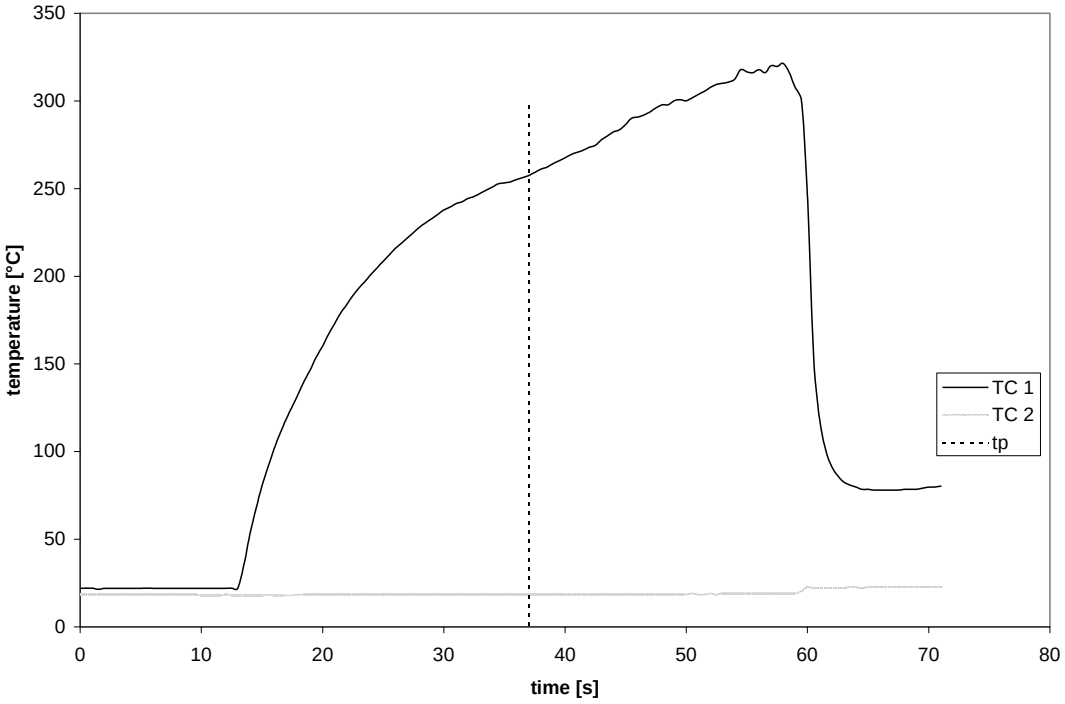

Figure 8 typical temperature versus time plot for an incident heat flux $\dot{q}_i''$ of 46.98 kW/m^2

Looking at Figure 8, which is a typical temperature versus time plot, several things can be observed. First, the thermocouple in the back does not recognizably change over the whole time period, which shows that heat losses through the back of the

sample can be reasonably neglected. Second, the slope decreases as the temperature approaches the onset of pyrolysis (t_p) but never flattens showing that the external heat flux provided might be in excess of that necessary for pyrolysis. A different reason for the unexpected result is that at this point the thermocouples start a process of detachment from the surface. The thermocouple mounted in the surface of the sample material (PMMA) separates from the surface, therefore does not read the surface temperature any more. The temperature readings would resemble an energy mixture coming from the gases over the surface and the radiant energy, which starts to directly impinge on it and [JeNC-79, WaWa-95, GlSS-56, DanG-68, BolW-48]. This might explain the acquired readings, which caused an increase in the temperature the further the degradation process continued. Improved measurements can be obtained with an infrared camera as described in Section 2.2.

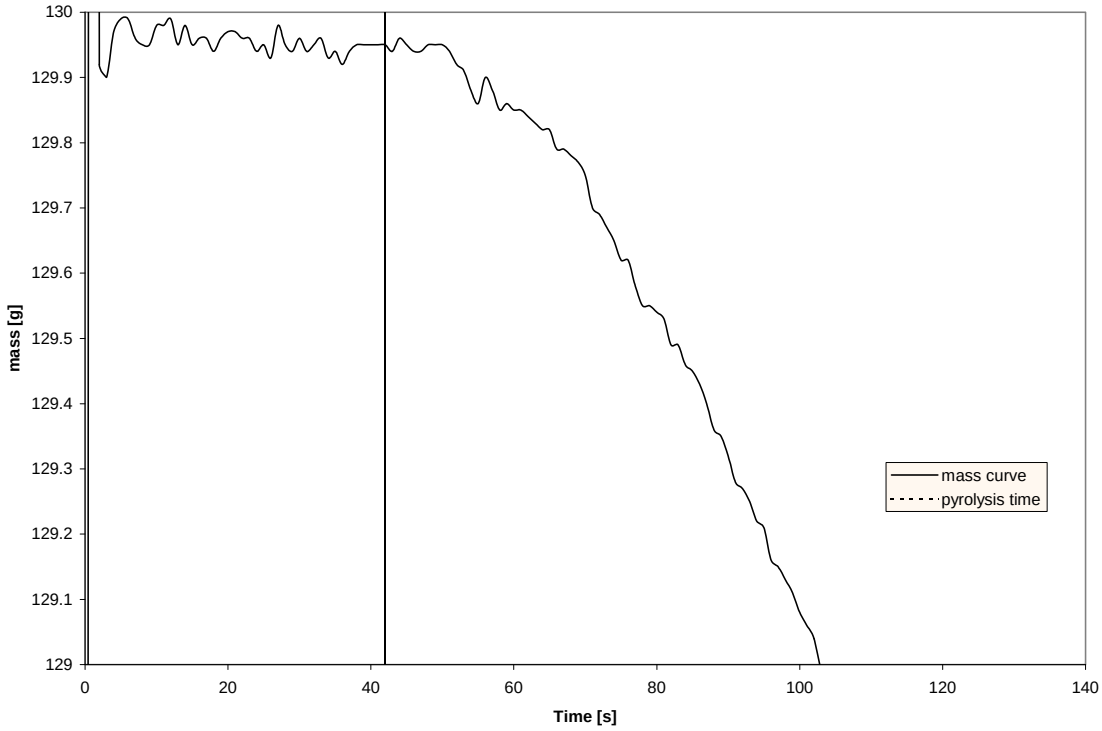

Figure 9 mass versus time plot for an incident heat flux $\dot{q}_i^{"}$ of 35.64 kW/m^2

As mentioned before, mass loss was also recorded and an example of the time evolution of the sample mass is presented in Figure 9. The mass loss evolution presented in Figure 9 was obtained in the absence of a surface thermocouple.

An initial peak is observed in the first few seconds and corresponds to the period where the sample is placed under the cone heater. This period is characterized by a large peak in the mass readings followed by oscillations that, never the less, show that in the phase up to pyrolysis almost no mass loss occurs. A real change in mass starts to occur a certain period of time after the initiation of pyrolysis and converges to a linear dependency with time which indicates a constant mass loss (constant slope). The

fluctuations around a decaying straight line are probably due to the bursting of bubbles, which cause recoil onto the scale and dynamic oscillations.

Correlation between the different events, temperature, flow visualization and mass loss will allow a more consistent definition of the onset of pyrolysis.

2.2. Temperature Measurements with an Infra Red Camera

The use of a non-intrusive measurement technique, infra-red thermography, was attempted, not only to avoid the problems expressed in the previous section, but also as further validation of the definition of the event that marks the onset of pyrolysis. The main element of the experimental setup is an infrared camera, which has the capability to record incoming radiation in the infrared band, into a pixel image with 256 gray levels. A preliminary validation of this technique will be presented in this section. A single temperature evolution will be used to explain the methodology used, a number of experiments were conducted to give statistical value to the correction presented here. Further validation for the materials that will be used during flight experiments is necessary but goes beyond the scope of this study, and will be a subject of future work.

The experimental apparatus had to be changed to conduct experiments in a way that the infrared camera will not be exposed to the direct heat from the cone heater. As can be observed from Figure 10 the cone heater and sample were rotated by a 90° angle. The range of the scale required a lightweight structure therefore the sample was embedded in fiberfrax (a lightweight) insulating material. The fiberfrax with the test

specimen was held in place by an aluminum frame, with a stand that serves to support the sample on the scale (Figure 10). To place the stand at the right distance from the cone heater a measuring element was used and is also shown in Figure 10.

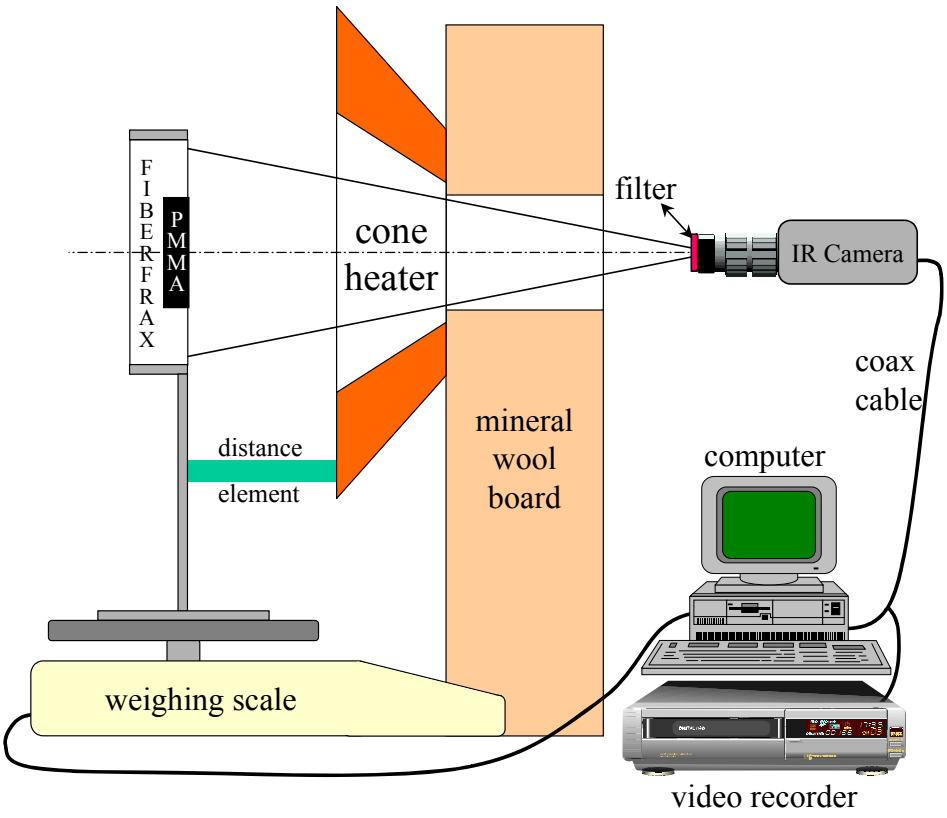

Figure 10 measurements with a non touching temperature measurement method

The infrared camera used was a model "13463" from Inframetrics. The camera was custom-built for NASA and, therefore, is not part of the Inframetrics normal product line. Because of this no written manual could be obtained so the description of the camera will be based on comparable products, and thus, is not necessarily exact. The general technical information which is available, is that the camera works roughly in a

wavelength range between 1.5 and 5.5 μm , needs a 27 Volt DC power supply, cooling system consists of stirling cooler, has a digital image output and a serial port to control the unit. Included in the infrared camera is a filter wheel system, which was designed and build by NASA, to replaced the original filter system from Inframetrics. This filter wheel system consists of an array of six filter holder that can be rotated at different velocities, so that the digital image output provides, every $1/6^{th}$ of the frequency, a different image originating from one of the six filters.

The camera was placed perpendicular to the surface of the sample, looking through the center whole of the cone (Figure 10). The back of the cone proved to be a significant problem since the metal shield covering the heating element attained very high temperatures. An insulating material (mineral wool board (thermofiber LLC)) from thermafiber) had to be placed between the infrared camera and the cone. This insulation eliminated all radiation coming from the cone and also worked as a reflection shield. The data from the infrared camera was sent for processing to a computer and a video recorder. The computer consists of a Pentium-133 computer equipped with 64MB RAM and the EPIX imaging board PIXCI which grabs and process a large amount of graphical information produced by the recording infrared camera.

The PIXCI imaging board is designed to take advantage of the power of the host computer. Applications that were once restricted by a limited memory or processing power can now be easily accomplished with the PIXCI board and a compatible PCI

computer [EPIX-96]. The specifications of this card are listed in the following table (Table 1):

video input	Color or monochrome video:	S-Video, NTSC, PAL, RS-170, CCR
	Resolution-pixel:	754x480: S-Video, NTSC, RS-170 922x580: S-Video, PAL, CCIR
	Resolution-depth:	8bit: RS-170, CCIR YUV [4:2:2]: NTSC, PAL YCrCb: S-Video
	Capture/display rate	30 ftp: S-Video, NTSC, RS-170 25 ftp: S-Video, PAL, CCIR
Bus requirements	32 bit, 33 MHz PCI slot	
	0.55 Amps @ +5Volts	
	4.913 inches by 3.350 inches (short slot)	
Transfer rates	requires a burst mode PCI motherboard for full resolution image capture to motherboard DRAM.	
Display-DOS	via standard VGA:	limited to 4 bit (16 gray levels), non real-time display
	via Super VGA:	8 bit, 256 gray level display
Display-windows	display resolution as per installed VGA device driver	
	a DCI compatible S/VGA adapter is required for real-time display.	
Connections	4 Pin DIN Receptacle:	S-Video Input

	BNC Jack:	Composite Video Input
	DB15 Receptacle:	TTL I/O Triggers

Table 1 PIXCI card specifications [EPIX-96]

The other component of the computer is the Matrox Millennium graphic card, which displays the received information onto the computer screen. No further information about this graphic card and other computer components (such as Monitor) are given, because those are not necessarily required for the infrared thermography.

Due to the huge variety of different radiant sources in the surrounding environment such as the air or other surfaces filters had to be used. Filters will serve to narrow down the infrared bandwidth to a smaller band close to a specific wavelength of interest. The above mentioned infrared camera had six different filters available. Those infrared camera filters characteristics are depicted in Table 2. This table mainly characterizes the band in which radiation transmission is close to unity. In the species column a typical species which radiates in that bandwidth is listed.

Filter				
Number	Center bandwidth (CW) [μm]	Half bandwidth (HW) [μm]	Species	Transmission %
1	2.790	0.230	CO_2	5
2	2.790	0.222	CO_2	1
3	3.399	0.304	MMA	25
4	1.872	0.104	H_2O	25
5	4.277	0.053	CO_2	16
6	4.808	0.116	CO	100

Table 2 infrared camera filters characteristics

The temperature distribution on the surface of the sample can be obtained by using a filter. The filter will allow only a specific wavelength to be transmitted through (e.g. a CO_2 filter). If the material has a high emissivity around this wavelength and the surrounding environment has low emission and absorption the measurement error is minimized. The emissivity of the material, in that specific band, is necessary for further analysis. With the filter in front of the infrared camera, which can only transmit a certain portion of the incoming rays, the recording chip receives enough radiation to record it. With this intensity information, which is expressed digitally in 256 gray levels, and a calibration table, which was acquired form a black body radiator, the gray level of each pixel can be directly related to the surface temperature. The black body calibration curves for the six different filters are presented in Figure 11.

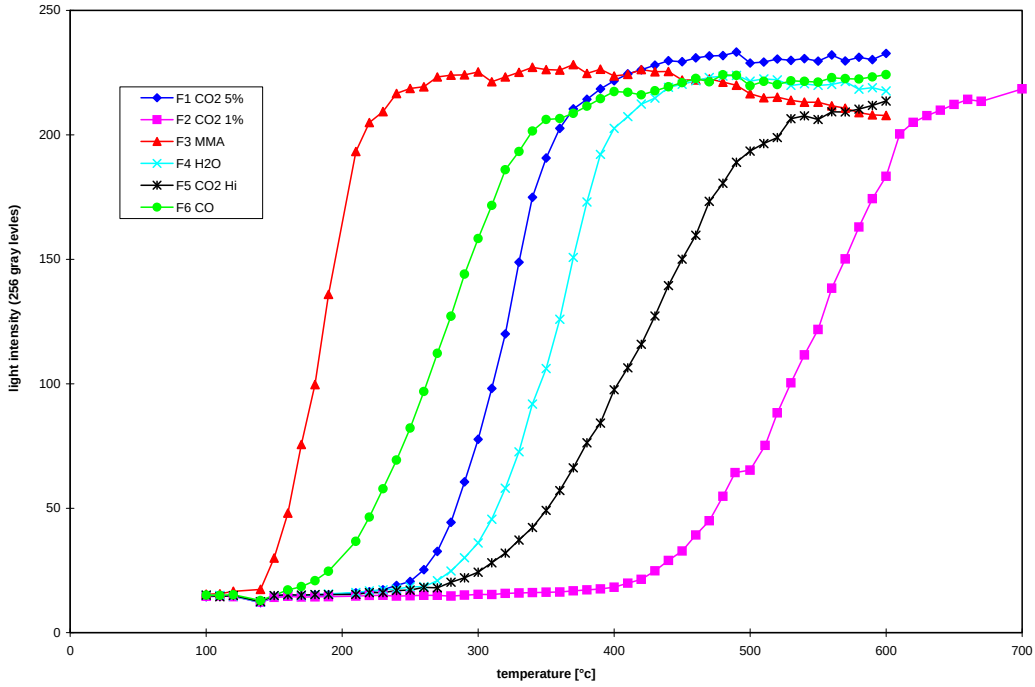

Figure 11 intensity versus temperature calibration for a black body

The specific MMA filter was chosen to also determine the onset of pyrolysis or the pyrolysis time, t_p. The decomposition of PMMA, leads to the production of MMA at approximately 265°C, at this point the emissivity of the surface in the bandwidth corresponding to MMA will increase approaching unity. Figure 11 shows that, for a black body, at this temperature the camera will saturate, therefore the onset of pyrolysis will be characterized by a sudden transition to a saturation level.

Simultaneous determination of the pyrolysis time, t_p, and temperature evolution over time is only possible by rotating the filters, the rate at which those filters can be rotated will determine the accuracy of the measurement.

The incident heat flux, $\dot{q}_i''$, was, again, calibrated with a heat flux meter, which was placed on the center axis of the cone heater. The correct distance between the heater and sample was achieved by the usage of the distance element, as mentioned above in this section (Figure 12).

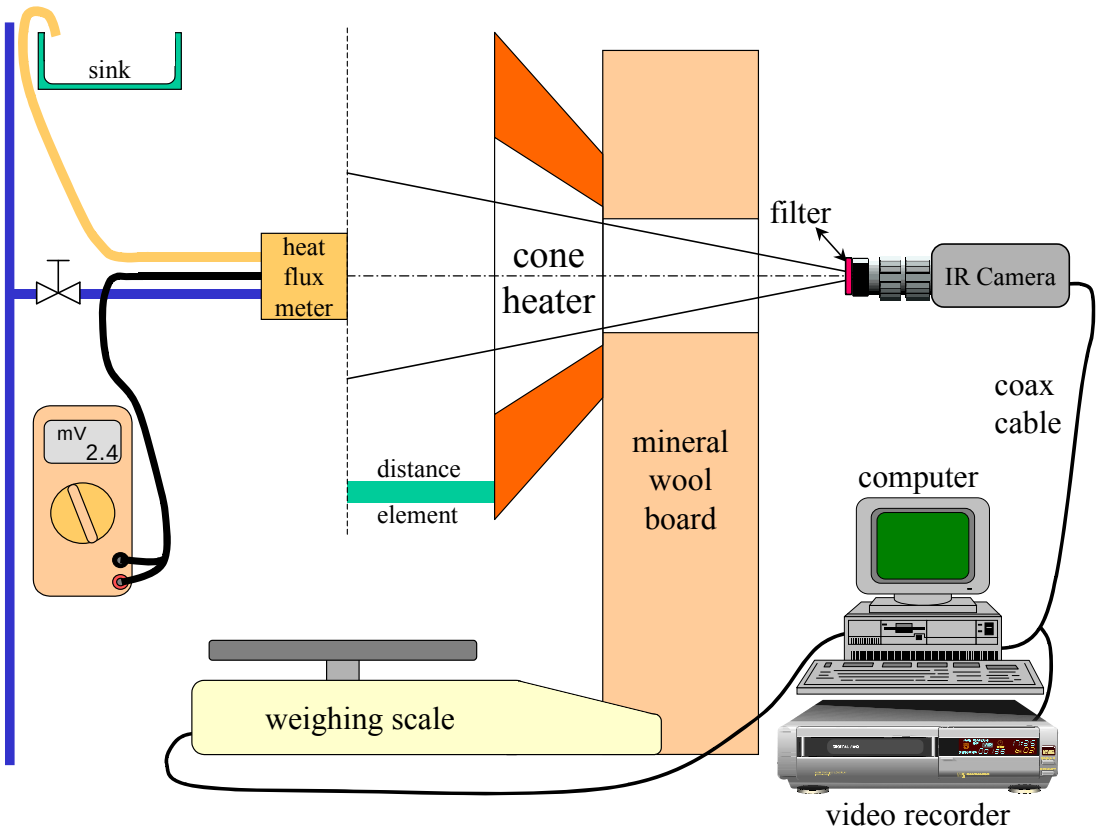

Figure 12 incident heat flux $\dot{q}_i''$ determination for the experimental apparatus measurements with a non touching temperature measurement method

The typical results for one incident heat flux $\dot{q}_i''$ from this apparatus are the

- Time surface intensity evolution of the test specimen Figure 13,

- Time surface temperature evolution of the test specimen Figure 15,
- Temperature distribution over the sample Figure 16,
- Time dependant weight Figure 17 and
- Time to pyrolysis Figure 13, Figure 15 and Figure 17.

Figure 13 displays a typical recorded intensity versus time plot for an incident heat flux $\dot{q}_i''$ of 49.68 kW/m^2 obtained by using filter number 6 acquired at a frequency of 1/3 of a second.

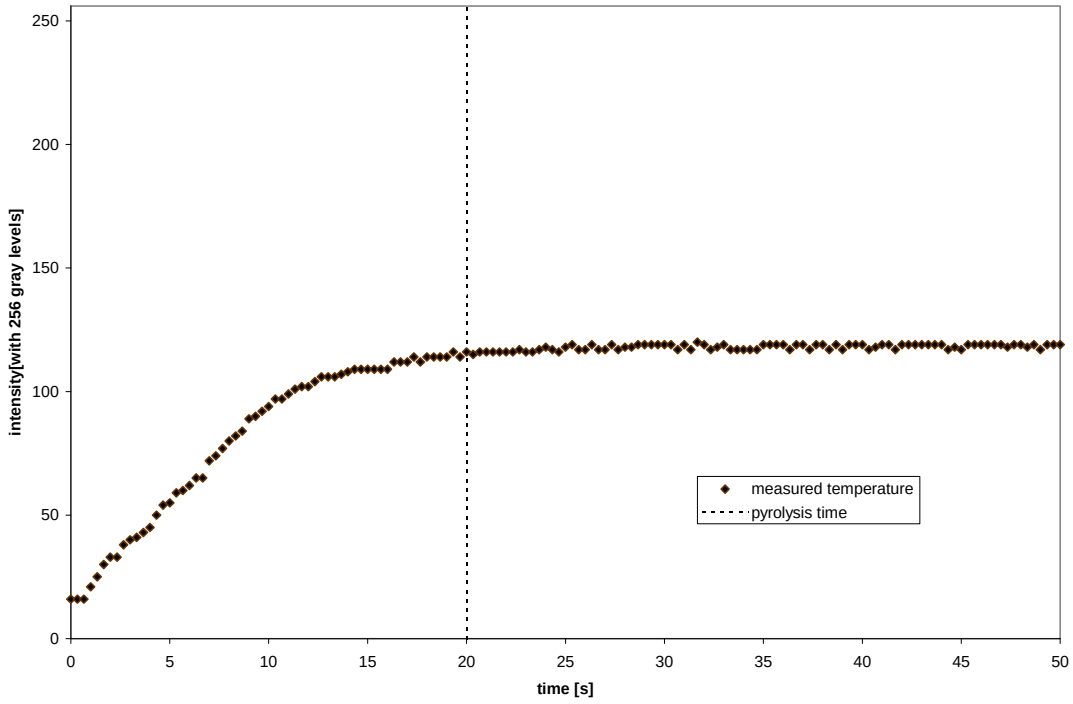

Figure 13 typical IR intensity versus time plot for an incident heat flux $\dot{q}_i''$ of 49.68 kW/m^2

Figure 13 shows a typical evolution of the intensity at the center point of the sample. When having a close look at the first second (the first 3 points) it seems as if there is no variation of the recorded intensity even though the sample is exposed to a very high heat flux. The data presented in Figure 13 was obtained with filter No. 6 which has a minimum temperature threshold of ~150°C below which no changes in the flux reaching the camera detector can be discerned (an approximate intensity of 14.28) and an erroneous constant intensity is recorded. This region represents no interest for the present study therefore, no attention will be given to correct these low temperature measurements. As the temperature increases the behavior of the intensity recordings is according to the expected evolution of the surface temperature. The rest of the curve will be discussed later when intensity data is converted to temperature data.

For the transformation from intensities to temperatures a polynomial-fit obtained from the NASA calibration data is used. The information presented in this section only corresponds to values for filter No. 6 since it is the one that covers best the temperature range of interest. The polynomial-fit is given by Equation (1).

$$T = 3.501103 \cdot 10^{-7} \cdot I^4 - 1.128546 \cdot 10^{-4} \cdot I^3 + 7.187482 \cdot 10^{-3} \cdot I^2 + 0.9211355 \cdot I + 229.3304 \quad (1)$$

Figure 14 presents a lookup plot for Equation (1), where I is the intensity given in a 0-256 range of gray levels and T is the temperature in °C. A fourth order polynomial was chosen because it best followed the evolution of the black body

calibration data. A graphic representation of Equation (1) is presented in Figure 15. Note that the axis are inverted from the way the data is presented in Figure 11, this was done just for practical convenience. The polynomial-fit follows well the data points only in the range between the intensity of 18.97 and 228, which corresponds to a temperature range between 240°C and 430°C. Knowing that PMMA pyrolysis occurs at about 265°C the range corresponding to filter 6 is appropriate when focussing on the onset of pyrolysis. A broader range would obviously be useful but, Filter No. 6 has to be changed and only the MMA filter provided covers a lower range.

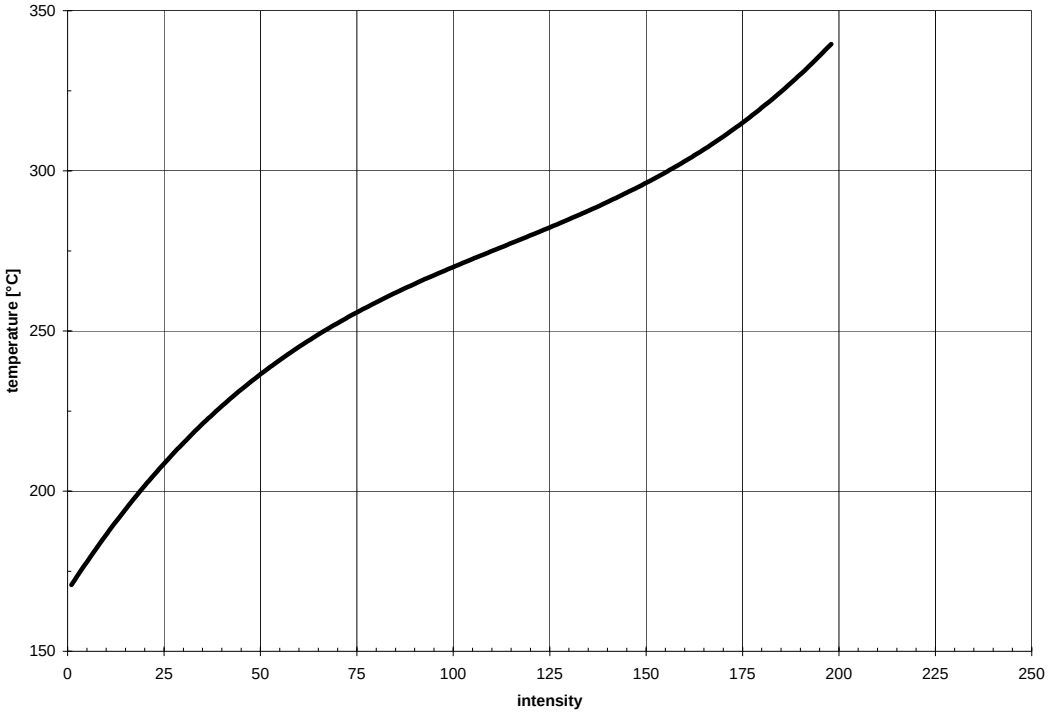

Figure 14 lookup plot

Converting the intensities of Figure 13 with the help of Equation (1) into temperatures, one obtains Figure 15.

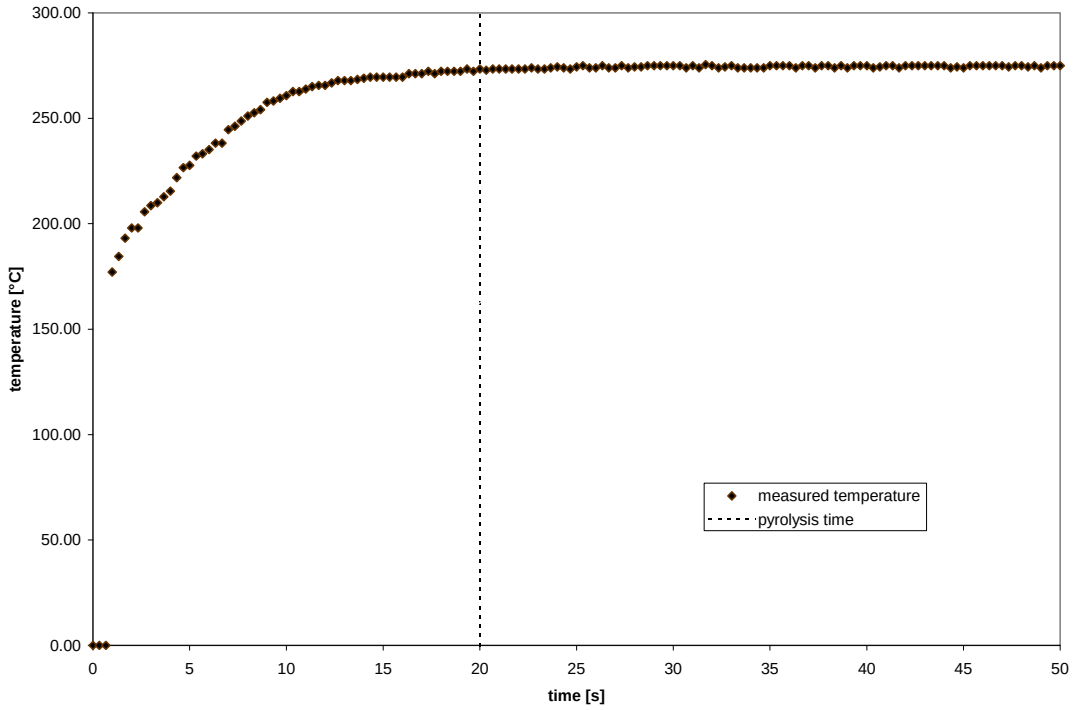

Figure 15 typical IR temperature versus time plot for an incident heat flux $\dot{q}_i''$ of 49.68 kW/m^2

Figure 15 describes a typical temperature versus time plot, on which several things can be seen. The temperature curve resembles the behavior of the sample surface temperature. When the graph approaches the pyrolysis time t_p, the temperature curve, which resembles the temperature of the sample surface, flattens out and stays constant after attaining the pyrolysis temperature. This phenomenon is described in the theory chapter. Approaching the pyrolysis time t_p, more and more of the impinging energy is used to pyrolyze the fuel instead of further heating the sample surface. After having attained the pyrolysis (pyrolysis time t_p and pyrolysis temperature T_p) the impinging energy is no longer used, to further heat up the sample surface, but to conduct pyrolysis

(solid to gas phase transition), which causes the leveling of and therefore the surface remains at the pyrolysis temperature T_p.

A temperature distribution of a PMMA sample exposed by an incident radiant heat flux is depicted in Figure 16.

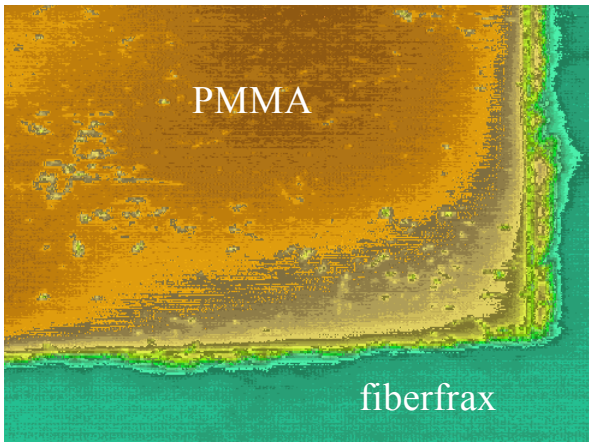

Figure 16 temperature distribution over the sample

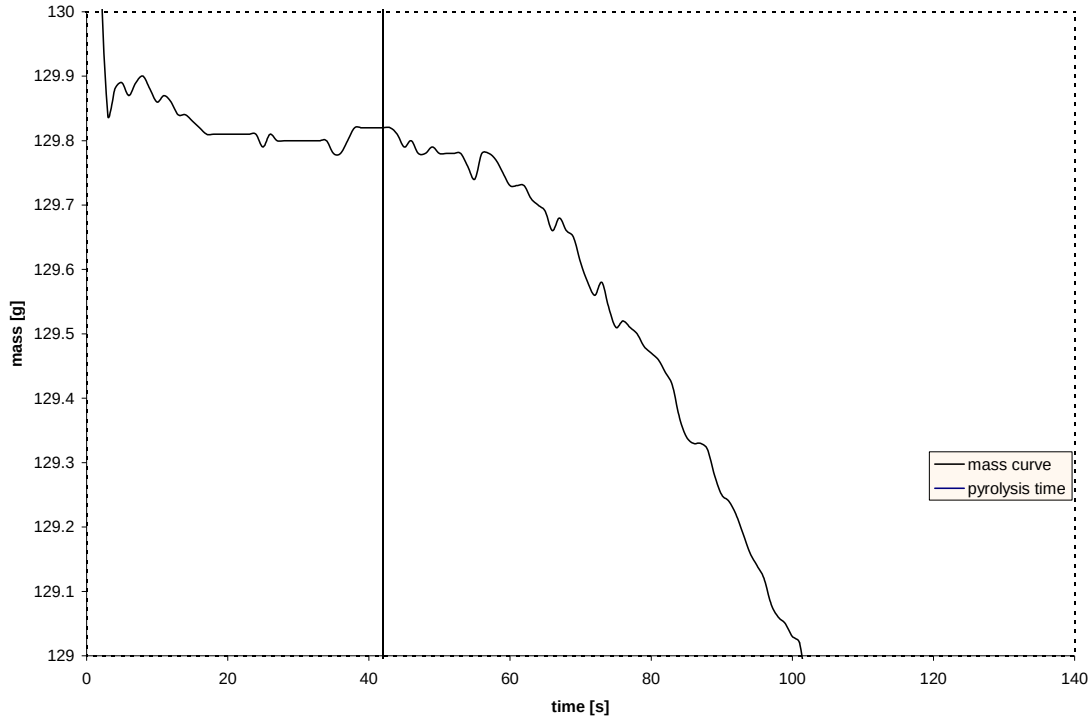

Figure 17 IR mass versus time plot for an incident heat flux $\dot{q}_i^{"}$ of 35.64 kW/m^2

The above depicted mass versus time plot graph shows, as one would expect an equivalent result compared the "Thermocouple Measurements" because nothing has really changed in the test setup, only that the sample is placed now vertically instead of horizontally, therefore the short discussion of Section 2.1 is also valid fort this graph.

2.3. Correction Methodology

As mentioned earlier, a single temperature distribution will be used to illustrate the methodology, but validation included 9 tests conducted all at an incident heat flux $\dot{q}_i^{"}$ of 30.78 kW/m^2. Test 1 trough 4 were conducted only using the infrared camera, while in test 5 trough 9 with the infrared camera and a thermocouple placed just

underneath the surface of the test specimen, as depicted in and Figure 5. The typical temperature evolutions are presented in Figure 18.

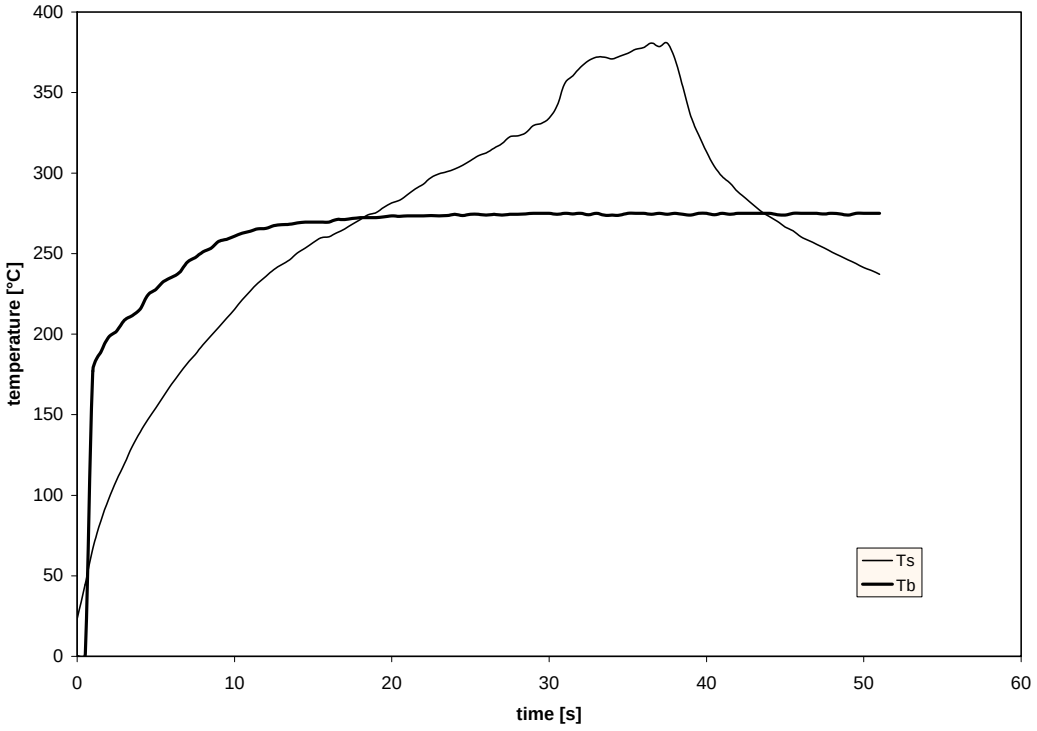

Figure 18 IR, TC temperature comparison

As can be seen from the above figure, significant discrepancies can be observed between the two temperature histories. Thermocouples can be considered to provide an adequate temperature distribution away from pyrolysis, but as the fuel degrades the thermocouple separates from the surface and the temperature measurements differ from the real surface temperature. The IR-camera does not have this problem but the temperatures obtained from the calibration, and presented in Figure 18 correspond to energy reaching the camera sensor and converted as if it was a black body. In reality the

material is not a black body, therefore its emissivity needs to be considered, and the total heat flux reaching the camera sensor includes also the incoming energy from the heater and reflected at the surface. Therefore the reflectivity of the material also needs to be considered. The percentage of the energy transmitted through the filter is accounted for through the black body calibration, therefore is not considered in this analysis.

The energy coming from the surface (s) towards the infrared camera (IR) can be expressed by the following equation:

$$\dot{q}''_{IR} = F_{s-IR}(\varepsilon\sigma T_s^4 + r\dot{q}''_i) \tag{2}$$

where, $\dot{q}''_{IR}$ is the energy seen by the sensor, F_{s-IR} the view factor between the surface and the sensor (a constant), σ the Stefan-Boltzman constant, ε the emissivity and r the reflectivity. In a narrow bandwidth and for the small temperature range of interest, the emissivity and reflectivity have a small variation. Since the dependency on this parameters is to the power 0.25, small variations will have little effect on the results, therefore, both values will be considered constant. This assumption will lead to errors that will need to be evaluated in the future.

The camera will translate, by means of the calibration, this energy into a black body temperature T_b providing the evolution presented in Figure 18. The relationship that describes this translation is presented in Equation (3)

$$\sigma T_b^4 = \dot{q}''_{IR} = F_{s-IR}(\varepsilon\sigma T_s^4 + r\dot{q}''_i) \tag{3}$$

with all temperatures in Kelvin. Rearranging Equation (3), the following expression is obtained:

$$\left(\frac{T_b}{T_s}\right)^4 = C_1 + \frac{C_2\dot{q}''_i}{T_s^4} \tag{4}$$

Where $C_1 = F_{s-IR}\varepsilon$ and $C_2 = \frac{r\,F_{s-ir}}{\sigma}$ are the unknown constants, the object of the calibration. Once the constants are obtained by comparing thermocouple and IR-camera temperature measurements, the surface temperature, as obtained from the IR-camera (T_{s-IR}) is given by:

$$T_{s-ir} = \left(\frac{T_b^4 - C_2\dot{q}''_i}{C_1}\right)^{0.25} \tag{5}$$

As the surface temperature increases, the contribution of the surface reflection becomes negligible ($\frac{C_2\dot{q}''_i}{T_s^4} \to 0$) and Equation (4) can be approximated by:

$$\left(\frac{T_b}{T_s}\right)^4 \approx C_1 \tag{6}$$

T_b is obtained from the IR-camera calibration and T_s from the thermocouple measurements and an asymptotic value for C_1 can be extracted by plotting the ratio. It needs to be noted that the surface temperature, as obtained from the thermocouple, is limited by pyrolysis, since the accuracy of this measurement decreases as it approaches decomposition. This is the most significant source of error, since the asymptotic value might not be reached in this range of temperatures. Experiments at low heat exposures should provide the more accurate results. Here a case with a large heat flux, $\dot{q}_i^{''}$ = 30.78 kW/m^2, to show that even at large heat fluxes an asymptotic value seems to be reached.

Figure 19 shows a typical evolution of the $\left(\frac{T_b}{T_s}\right)^4$ ratio as a function of time, as can be seen from the figure the ratio leads to an asymptotic value, that for this case is approximately 0.8. It can also be noted that the separation of the thermocouple from the surface is clearly shown by discontinuities in the ratio followed by a reverse trend (thermocouple measuring a higher temperature than the surface temperature). This discontinuity and trend change is common and serves as to provide a limit of validity for Equation (6). The dotted line represents a curve fit to the data that provides the asymptotic value shown by the arrow.

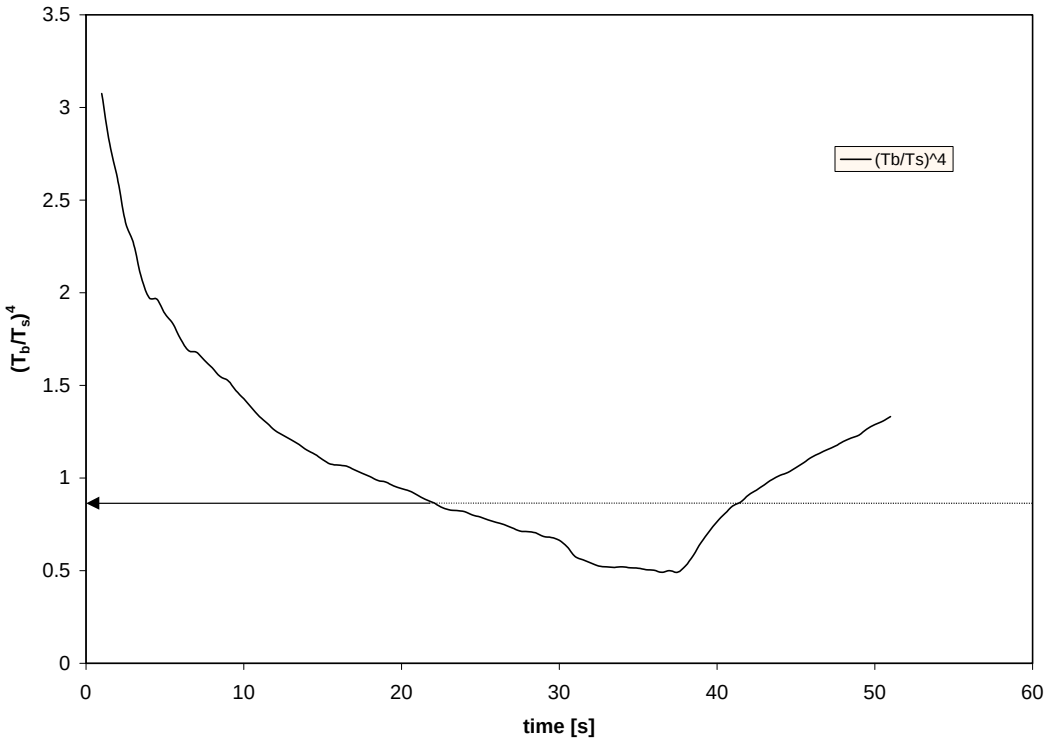

Figure 19 $(T_b/T_s)4$ versus time

Once the value of C_1 has been estimated, Equation (4) can be used to solve for C_2. Equation (7) shows this relationship:

$$C_2 = \left(\frac{T_b^4 - C_1 T_s^4}{\dot{q}_i''} \right) \tag{7}$$

Again, the thermocouple measurements and the black body temperature, as obtained from the camera, can be used to evaluate C_2. Best accuracy can be obtained at low temperatures within the limits of the calibration. As the temperature approaches the lower limit of the calibration, the accuracy of T_b decreases, similarly with T_s as the

surface temperature approaches pyrolysis. A typical plot of C_2 is presented in Figure 20.

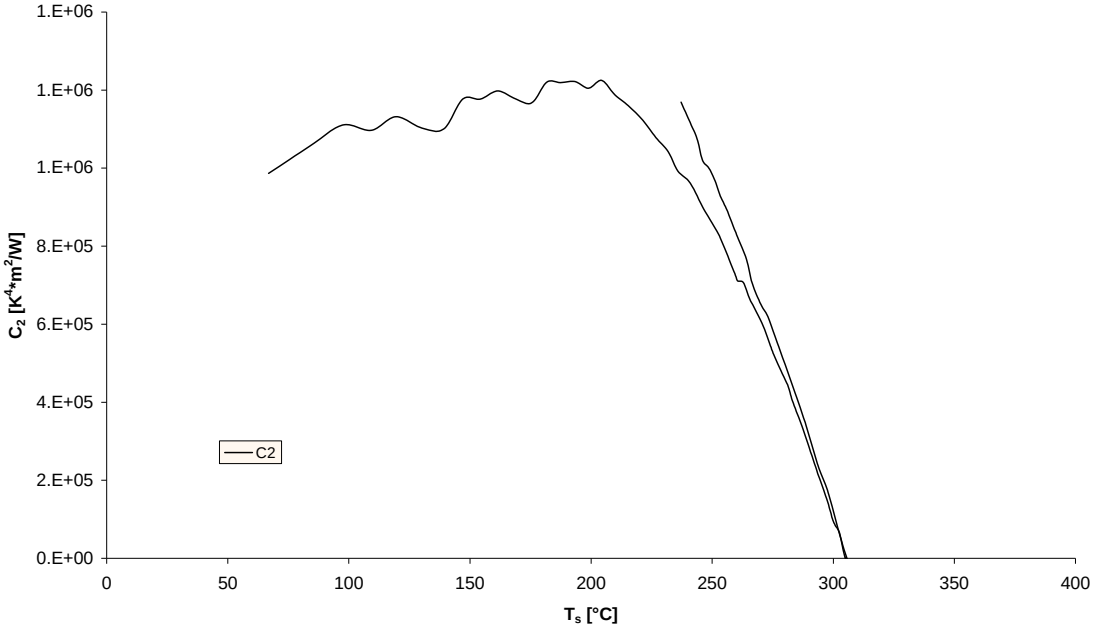

Figure 20 C_2 versus T_s

This time the plot is presented as a function of the temperatures as measured by the thermocouple (T_s), to better depict the range of validity. An average value of $11 \cdot 10^6 \left[\frac{K^4 m^2}{W} \right]$ was chosen for C_2, and represents the average in the range of 60-200^{o}C. As can be seen from in Figure 20, beyond 200 there is a sudden trend change and the reverse curve shows the cooling down of the of the thermocouple after the first 40 seconds (Figure 18).

Finally, the C_1 and C_2 are substituted in Equation (4) and the corrected infrared temperature measurement can be obtained. Figure 21 shows the corrected values as a function of time presented together with the thermocouple measurements. As can be seen, the correction fits very well the low temperature data and significant discrepancies only appear as the surface approaches pyrolysis, at this point the IR-temperature should provide a more adequate determination of the surface temperature.

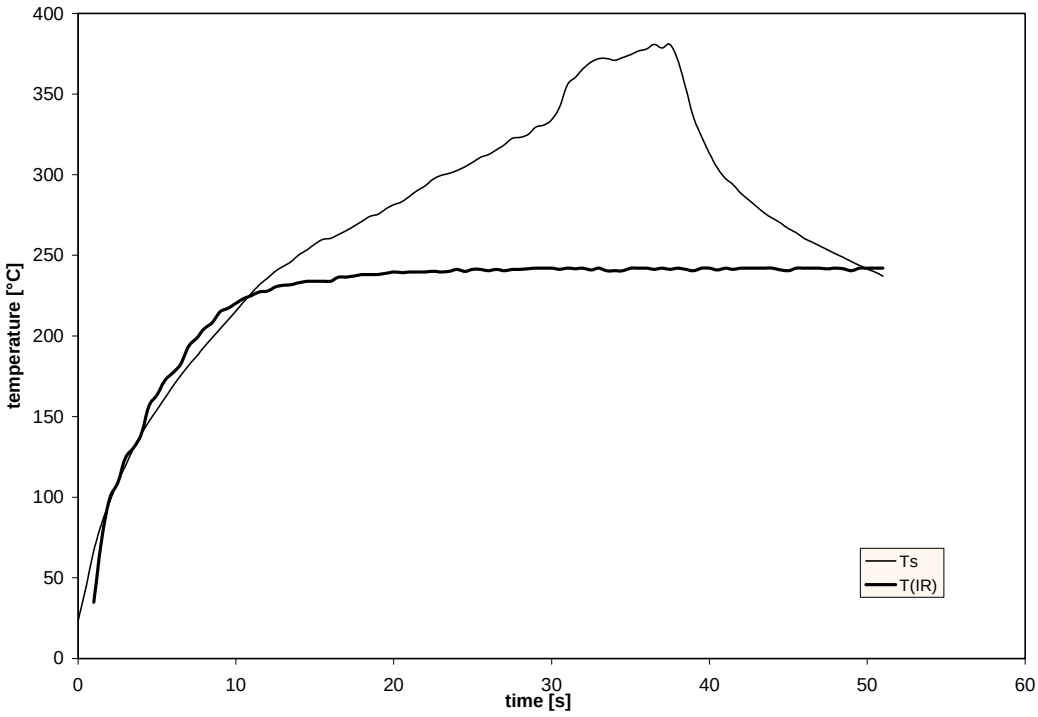

Figure 21 corrected IR, TC temperature comparison

The pyrolysis temperature predicted by the IR camera seems approximately 100°C lower than temperatures estimated previously for this same material. As mentioned before this temperature histories are only presented to illustrate the

methodology, therefore, the quantitative values here should not be taken as absolute values. Further validation of the constants C_1 and C_2 for different heat fluxes and multiple tests will provide a better quantitative indication of the surface temperatures.

3. Theoretical Background

3.1. Ignition Theory

In the following section the theoretical background that describes the mechanisms that lead to gas phase ignition from a solid fuel sample, are going to be described to create the basis on which this work was conducted.

The solid fuel sample is considered initially to be at ambient temperature T_∞. When the sample is suddenly exposed to an incident heat flux $\dot{q}_i''$, which is constant during the testing time, the temperature of the solid fuel sample rises and it passes different transition stages. For the polymer PMMA the first transition stage when heated up from ambient temperature T_∞ is the glass transition, which occurs at the glass transition temperature T_g (for more detail see Section 4.4). The second transition stage, is the transition between the soft stage to the gas phase stage, where a transformation of PMMA (Poly(methyl Methacrylate)) into MMA (Methyl Methacrylate) takes place, this occurs when the surface temperature of the sample reaches the pyrolysis temperature T_p. The time required for the fuel surface to attain T_p, starting when the incident heat flux $\dot{q}_i''$ was imposed on the sample surface, will be referred to as the pyrolysis time t_p. When having attained T_p, the vapor (pyrolysate or MMA) leaves the surface and diffuses and convects outwards mixing with the ambient oxidizer and creating a flammable mixture near the solid surface. This time period, from the point of pyrolysis

until the presence of a flammable mixture, is referred to as the mixing time t_m. The ruling parameters for that mixing time t_m are the flow and geometrical characteristics. For the specific case of the LIFT apparatus, used by [LonR-98], the flow was natural convection and the geometry was fixed, therefore the mixing time t_m is expected to be only a function of the external heat flux. When the temperature of the mixture is increased gas phase oxidation of the fuel vapor may become so strong, that the created heat overcomes the heat lost to the solid and the ambient. At this point, the combustion reaction becomes self-sustained. That also means, flaming ignition would occur. The time period, from when a flammable mixture is present in the gas phase up to flaming ignition, corresponds to the induction time t_i, which is derived from a complex combination of fuel properties and flow characteristics.

Using and extending the analysis proposed by Fernandez-Pello [FerA-95], the time period between the time when the incident heat flux $\dot{q}_i''$ was imposed on sample surface and the point of the flaming ignition can be named the ignition delay time t_{ig}. This time is as depicted in Equation (8) the sum of the pyrolysis time t_p, the mixing time t_m and the induction time t_i.

$$t_{ig} = t_p + t_m + t_i \tag{8}$$

Under idealized conditions, such as in the LIFT, a pilot reduces the induction time t_i to a minimum, making it negligible when compared to t_p [QuiJ-81]. The

mixing process has been commonly considered to be a fast process compared to the heating of the solid fuel sample. Therefore, the fuel and oxidizer mixture becomes flammable almost immediately after the pyrolysis transition starts. Due to the two above described facts, the pyrolysis temperature and times (T_p and t_p) are commonly referred to such as in [QuiJ-81] as the ignition temperature and ignition delay time (T_{ig} and t_{ig}) as presented in equation (9) and (10).

$$t_{ig} = t_p \tag{9}$$

$$T_{ig} = T_p \tag{10}$$

Exactly these assumption are the topic of this work and will be discussed later, with the presentation of conducted pyrolysis tests with the test conducted by Long [LonR-98]. As it was just inferred such a definition is not physically correct [AlMa-71], but can be very useful in some practical applications since it provides a reference parameter that could serve to characterize ignition.

As presented above, the induction time t_i and the mixing time t_m have been considered negligible but, how good that describes the real world scenario is unknown. In his work, the piloted ignition ensured a minimal induction time t_i, which lead to Equation (11).

$$t_{ig} = t_p + t_m \tag{11}$$

That assumption can be assumed to be valid. Therefore, when knowing the pyrolysis time t_p as well as the ignition time t_{ig} for the here used material (PMMA), a statement can be made about the mixing time t_m.

The following sections present a more detailed view of the used theoretical models for the ignition process and are divided into the processes occurring before and after pyrolysis. Section 3.1.1 presents the main theory for the process up to pyrolysis and Section 3.1.2 presents a more detailed view of the theoretical model for the time after pyrolysis.

3.1.1. Pre Pyrolysis Process

This section is dedicated to the processes occurring before and at the pyrolysis of a solid fuel sample exposed to a constant incident heat flux $\dot{q}_i''$. To gain an in depth look at those processes an energy balance at the sample surface under radiative heating conditions is presented below.

The energy going to and coming from the sample surface (enclosed by the control volume) as shown in Figure 22, are the absorbed incident heat flux $a\dot{q}_i''$, the emitted energy $\varepsilon\sigma\left(T^4(0,t) - T_\infty^4\right)$, and the convective energy $h_c(T(0,t) - T_\infty)$. The sum of them resembles the net heat flux at the surface of the solid fuel sample $\dot{q}_s''(0,t)$.

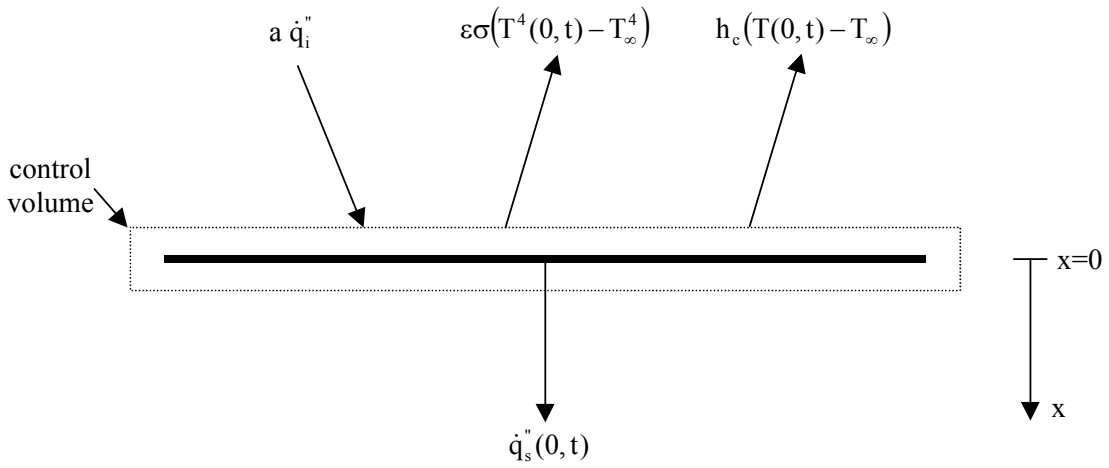

Figure 22 energy balance at the surface of the solid fuel sample

In equation (12) that energy balance is expressed as:

$$\dot{q}_s''(0,t \le t_p) = a\dot{q}_i'' - \varepsilon\sigma\left(T^4(0,t)-T_\infty^4\right) - h_c\left(T(0,t)-T_\infty\right) \tag{12}$$

Where $\dot{q}_s''$ is the net heat flux at the surface of the solid fuel sample, a is the absorptivity of the solid fuel sample, ε is the emissivity of the solid fuel sample, σ is the Stefan-Boltzmann constant, $T(0,t)$ is the surface temperature at time t, h_c is the convective heat transfer coefficient, and T_∞ is the ambient temperature.

To obtain an analytical solution, the classical analysis corresponding to the ignition process assuming a linear approximation for the surface re-radiation is used. Therefore, equation (12) can be rewritten with Equation (13) to Equation (14).

$$\varepsilon\sigma\left(T^4(0,t)-T_\infty^4\right)=h_r\left(T(0,t)-T_\infty\right) \tag{13}$$

$$\dot{q}_s''(0,t\le t_p)=a\dot{q}_i''-h_r\left(T(0,t)-T_\infty\right)-h_c\left(T(0,t)-T_\infty\right) \tag{14}$$

This simplification allows an analytical solution of the one dimensional heat conduction energy equation. Nevertheless, this assumption remains controversial especially in the range of the minimum heat flux necessary to attain the pyrolysis temperature.

When trying to simplify Equation (14), the total heat transfer coefficient h_t is equal to the sum of the convective heat transfer coefficient h_c and the radiative heat transfer coefficient h_r expressed mathematically by Equation (15).

$$h_t=h_c+h_r \quad \text{or} \quad h_t\left(T(0,t)-T_\infty\right)=h_c\left(T(0,t)-T_\infty\right)+h_r\left(T(0,t)-T_\infty\right) \tag{15}$$

Using Equation (15) leads to the simplified expression of the net heat flux $\dot{q}_s''$ at the surface of the solid fuel sample expressed in Equation (16) and depicted by Figure 23.

$$\dot{q}_s''(0,t\le t_p)=a\dot{q}_i''-h_t\left(T(0,t)-T_\infty\right) \tag{16}$$

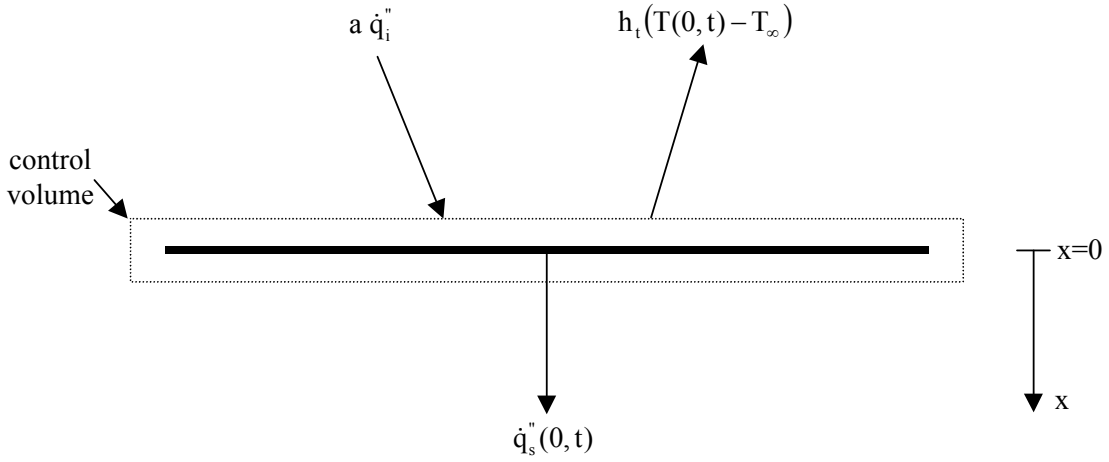

Figure 23 energy balance at the surface of the solid fuel sample simplified with total heat transfer coefficient h_t

Using the one dimensional heat diffusion equation

$$\frac{\partial}{\partial x}\left(\lambda\frac{\partial T}{\partial x}\right)+\dot{q}=\rho c_p\frac{\partial T}{\partial t} \tag{17}$$

and assuming that there is no internal heat generation and the thermal conductivity is independent of the location the following governing energy equation can be used (Equation (18)).

$$\frac{\partial^2 T}{\partial x^2}=\frac{\rho c_p}{\lambda}\frac{\partial T}{\partial t} \tag{18}$$

The first boundary conditions for the case described in Figure 23 at the surface ($x = 0$) can be expressed with

$$-\lambda \left.\frac{\partial T}{\partial x}\right|_{x=0} = \dot{q}_s''(0, t \le t_p) = a\dot{q}_i'' - h_t\left(T(0,t) - T_\infty\right). \tag{19}$$

While the second boundary condition for equation (18) for the temperature of the semi-infinite slab at $x = \infty$ is

$$T(\infty, t) = T_\infty . \tag{20}$$

Changing variables to:

$$\theta(x, t \le t_p) = \left(T(x,t) - T_\infty\right) \tag{21}$$

the governing energy equation (Equation (18)) can be rewritten to

$$\frac{\partial^2 \theta}{\partial x^2} = \frac{\rho c_p}{\lambda}\frac{\partial \theta}{\partial t} . \tag{22}$$

And the boundary conditions are transformed to

$$-\lambda \left.\frac{\partial \theta}{\partial x}\right|_{x=0} = \dot{q}_s''(0, t \le t_p) = a\dot{q}_i'' - h_t\theta(0,t) \tag{23}$$

and

$$\theta(\infty, t) = 0 . \tag{24}$$

Conducting a Laplace transformation ($L[\theta(t)] = \bar{\theta}(s)$)) and replacing $\frac{\rho c_p}{\lambda} s$ with k^2 Equation (22) can be rewritten to

$$\frac{\partial^2 \bar{\theta}}{\partial x^2} - \frac{\rho c_p}{\lambda} s\bar{\theta} = \frac{\partial^2 \bar{\theta}}{\partial x^2} - k^2 \bar{\theta} = 0 . \tag{25}$$

With boundary conditions:

$$-\lambda \left. \frac{\partial \bar{\theta}}{\partial x} \right|_{x=0} = \dot{q}_s''(0,s) = a\dot{q}_i'' - h_t \bar{\theta}(0,s) \tag{26}$$

$$\bar{\theta}(\infty, s) = 0 \tag{27}$$

Solving this ordinary homogeneous differential equation with constant properties leads to Equation (28).

$$\bar{\theta}(x,s) = \frac{a\dot{q}_i''}{s\left(h_t + \lambda\sqrt{\frac{\rho c_p}{\lambda} s} \right)} e^{-\sqrt{\frac{\rho c_p}{\lambda} s} \cdot x} = \frac{a\dot{q}_i''}{s\left(h_t + \sqrt{\lambda \rho c_p}\sqrt{s} \right)} e^{-\sqrt{\frac{\rho c_p}{\lambda}}\sqrt{s} \cdot x} \tag{28}$$

Inverting this Laplace solution, one gets with the table on page 262 in [ÖziM-80] the following general solution.

$$T - T_\infty = \frac{a\dot{q}_i''}{(h_T)}\left[\operatorname{erfc}\left(\frac{x}{\sqrt{4\frac{\lambda}{\rho c_p}t}}\right) - e^{\frac{h_T}{\sqrt{\frac{\lambda}{\rho c_p}}\sqrt{\lambda\rho c_p}}x+\frac{(h_T)^2}{\lambda\rho c_p}t}\operatorname{erfc}\left(\frac{h_T}{\sqrt{\lambda\rho c_p}}t^{\frac{1}{2}} + \frac{x}{\sqrt{4\frac{\lambda}{\rho c_p}t}}\right)\right] \tag{29}$$

To obtain the surface temperature T_s, x is set to 0, $T(0, t \le t_p) = T_s(t)$ and with the fact, that $\operatorname{erfc}(0) = 1$ and $\operatorname{erfc}(\infty) = 0$ Equation (29) can be simplified to

$$T_s(t \le t_p) = T_\infty + \frac{a\dot{q}_i''}{h_T}\left[1 - e^{\frac{(h_t)^2}{\lambda\rho c_p}t} \cdot \operatorname{erfc}\left(\frac{h_T}{\sqrt{\lambda\rho c_p}}t^{\frac{1}{2}}\right)\right] \tag{30}$$

Looking at equation (30) $\frac{a\dot{q}_i''}{h_T}$ can be defined as a characteristic temperature $\overline{T}$

$$\overline{T} = \frac{a\dot{q}_i''}{h_T} \tag{31}$$

and $\frac{\lambda\rho c_p}{(h_T)^2}$ is defined as a characteristic time t_c

$$t_c = \frac{\lambda\rho c_p}{(h_T)^2} \tag{32}$$

so that Equation (30) can be rewritten to

$$T_s(t \le t_p) = T_\infty + \overline{T}\left[1 - e^{\frac{t}{t_c}} \operatorname{erfc}\left(\left(\frac{t}{t_c}\right)^{\frac{1}{2}}\right)\right]. \tag{33}$$

This is the general solution for the surface temperature at all levels of incident heat fluxes and times after exposure. At the onset of pyrolysis the time t becomes the pyrolysis time t_p the surface temperature $T_s(t)$ is substituted by pyrolysis temperature $T_p = T_s(t_p)$ and equation (33) becomes

$$T_p = T_s(t_p) = T_\infty + \overline{T}\left[1 - e^{\frac{t_p}{t_c}} \operatorname{erfc}\left(\left(\frac{t_p}{t_c}\right)^{\frac{1}{2}}\right)\right]. \tag{34}$$

The pyrolysis temperature T_p for PMMA is approximately 265°C.

3.1.1.1. Pyrolysis Time (t_p)

To determine which parameters influence the pyrolysis time t_p the above conducted analysis has to be extended by solving Equation (34) for the parameter pyrolysis time t_p. This causes some problems due to the presence of the complement of the error function (erfc) which can be expressed in an infinite power series by

$$\operatorname{erfc}(x) = 1 - \operatorname{erf}(x) = \frac{2}{\sqrt{\pi}} \int_x^\infty e^{-u^2} du = 1 - \frac{2}{\sqrt{\pi}}\left(x - \frac{x}{3 \cdot 1!} + \frac{x^5}{5 \cdot 2!} - \frac{x^7}{7 \cdot 3!} + \dots\right) \tag{35}$$

Nevertheless, a pyrolysis time solution for Equation (34) can be found by focusing on two regions. The first region would be where $t_p << t_c$ and the second region would be where $t_p >> t_c$.

The **first region**, where $t_p << t_c$ means, that the time it takes the surface of the fuel sample to attains pyrolysis temperature T_p is very fast an therefore a lot smaller than the characteristic time t_c this occurs for high incident heat fluxes $\dot{q}_i''$. The above described fact also mean, that the time fraction $\frac{t_p}{t_c}$ approaches zero as described in Equation (36).

$$\frac{t_p}{t_c} \to 0 \tag{36}$$

Knowing that and the fact, that the error function

$$\operatorname{erfc}(0) = 1 \tag{37}$$

it is reasonable to use the first order approximation of Equation (35) as presented in Equation (38).

$$\operatorname{erfc}(x) \approx 1 - \frac{2}{\sqrt{\pi}} x \tag{38}$$

For the same reason (Equation (36)) and a first order approximation of the exponential term of Equation (34) ($e^{\frac{t_p}{t_c}}$) can be approximated to be equal to 1 as presented in Equation (39).

$$e^0 \approx 1 \tag{39}$$

Which transforms Equation (34) into Equation (40).

$$T_p = T_\infty + \overline{\overline{T}} \frac{2}{\sqrt{\pi}} \left(\frac{t_p}{t_c} \right)^{\frac{1}{2}} \tag{40}$$

Solving that equation for $\frac{1}{\sqrt{t_p}}$ and using $\frac{a\dot{q}_i''}{h_T}$ for the characteristic temperature $\overline{\overline{T}}$ and $\frac{\lambda \rho c_p}{(h_T)^2}$ for the characteristic time t_c so that the following formulation for the pyrolysis time t_p can be obtained.

$$\frac{1}{\sqrt{t_p}} = \frac{2}{\sqrt{\pi}} \frac{a}{\sqrt{\lambda \rho c_p}} \frac{\dot{q}_i''}{(T_p - T_\infty)} \tag{41}$$

As one can see from Equation (41), the first region (short ignition times) solution for the pyrolysis time t_p is independent of the total heat transfer coefficient h_t. Thus the pyrolysis time t_p is a function of the energy absorbed $a\dot{q}_i''$ due to radiation

from the radiant panel and the material properties λ, ρ, and c_p of the solid fuel sample.

The **second region** where $t_p >> t_c$ describes the fact, that the time it takes the surface of the fuel sample attains pyrolysis temperature T_p is very long if not infinitely long and therefore a lot bigger than the characteristic time t_c. That corresponds to a low incident heat fluxes $\dot{q}_i''$. That fact means, that the time fraction $\frac{t_p}{t_c}$ approaches infinity for very long pyrolysis times t_p, which is expressed in Equation (42).

$$\frac{t_p}{t_c} \to \infty \tag{42}$$

Knowing, that the error function

$$\text{erfc}(\infty) = 0 \tag{43}$$

or that the exponential term of Equation (34) ($e^{\frac{t_p}{t_c}}$) is

$$e^{\infty} = \infty$$

does not contribute to a further analysis. Therefore, a slightly different expression for the error function of Equation (35) is used and is represented by the following equation.

$$\operatorname{erfc}(x) \approx \frac{e^{-x^2}}{\sqrt{\pi}\cdot x}\left(1-\frac{1}{2x^2}+\frac{1\cdot 3}{\left(2x^2\right)^2}-\frac{1\cdot 3\cdot 5}{\left(2x^2\right)^3}+\ldots\right) \tag{44}$$

Knowing that and the fact, that the time fraction $\frac{t_p}{t_c}$ approaches infinity it can be assumed, that the first order approximation of Equation (44) can be used in the further analysis as presented in Equation (45).

$$\operatorname{erfc}(x) \approx \frac{e^{-x^2}}{\sqrt{\pi}\cdot x} \tag{45}$$

Using Equation (45) in Equation (34) leads to Equation (46).

$$T_p = T_\infty + \overline{T}\left[1-e^{\frac{t_p}{t_c}}\frac{e^{-\frac{t_p}{t_c}}}{\sqrt{\pi}\cdot\left(\frac{t_p}{t_c}\right)^{\frac{1}{2}}}\right] \tag{46}$$

Solving that Equation (46) for $\frac{1}{\sqrt{t_p}}$ and using $\frac{a\dot{q}_i''}{h_t}$ for the characteristic temperature $\overline{T}$ and $\frac{\lambda\rho c_p}{(h_t)^2}$ for the characteristic time t_c so that the following formulation for the pyrolysis time t_p can be obtained.

$$\frac{1}{\sqrt{t_p}} = \frac{\sqrt{\pi}\sqrt{\lambda\rho c}}{h_t}\left[1 - \frac{h_t\left(T_p - T_\infty\right)}{a\dot{q}_i''}\right] \tag{47}$$

As one can see from Equation(47), the second region (long ignition times) solution for the pyrolysis time t_p is dependent of the total heat transfer coefficient h_t, which is different from the first region, which was independent. Thus the pyrolysis time t_p is not only a function of the energy absorbed $a\dot{q}_i''$ due to radiation from the radiant panel and the material properties λ, ρ, and c_p of the solid fuel sample but also dependant of the total heat transfer coefficient h_t.

The dependency of Equation (41) and the independence of Equation(47) on the total heat transfer coefficient h_t can also be explained logically. When the incident heat flux $\dot{q}_i''$ from external sources is big, the losses to the surrounding environment by radiation and convection are minor compared to the incident heat flux $\dot{q}_i''$. But when the incident heat flux $\dot{q}_i''$ from external sources is small, the losses to the surrounding environment play an important role. Long [LonR-98] has determined, that for the sample material PMMA the losses to the surrounding play a minor role till close to the critical heat flux as depicted in Figure 24. Long assumed, that the ignition delay time t_{ig} would be in the same range as the time to pyrolysis t_p. Therefore the ignition delay times $t^{-1/2}$ was plotted in Figure 24 versus the incident heat flux $\dot{q}_i''$. Figure 14 shows an excellent correlation between theory and the collected data even for heat fluxes close to the critical heat flux. Therefore Equation (41) is used for the later analysis.

Additional to data from Long [LonR-98] and Quintere [QuHa-84] Figure 24 presents the first and second region expressed by Equation (41) and Equation(47).

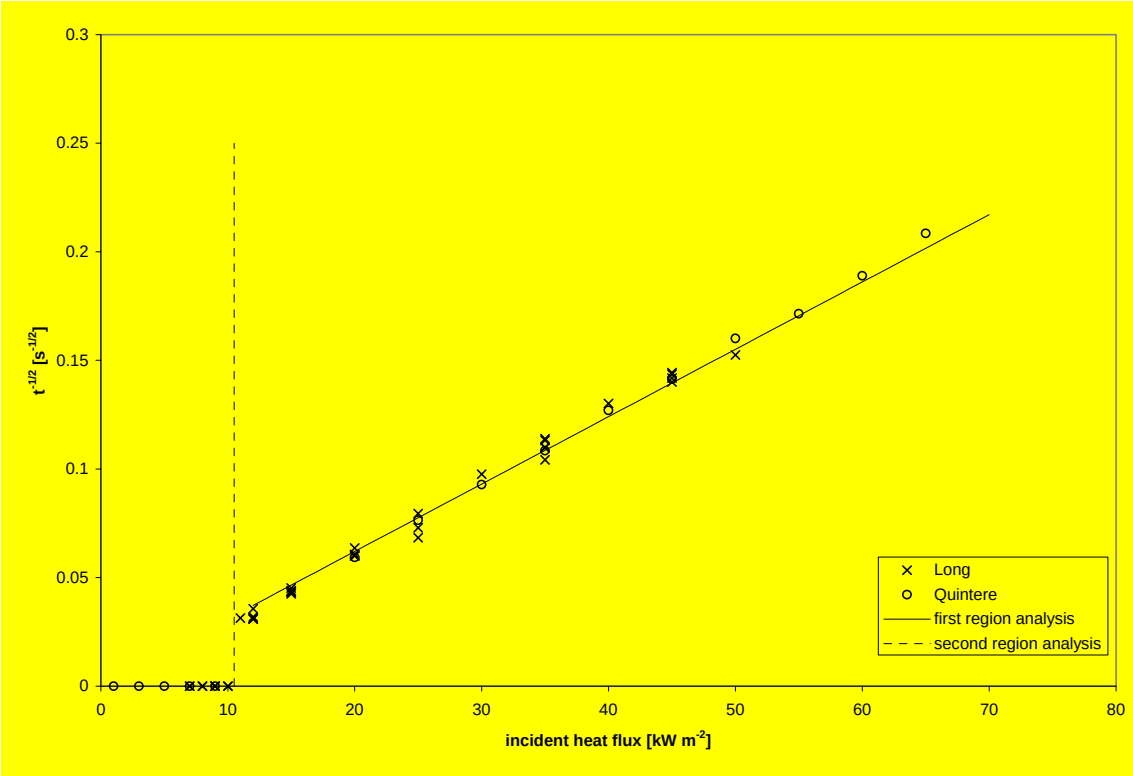

Figure 24 ignition delay times $t^{-1/2}$ versus incident heat flux $\dot{q}_i''$

3.1.1.2. Net Heat Flux Into the Sample ($\dot{q}_s''(0, t \le t_p)$)

For a later mass contemplation it is interesting to determine the time evolution, up to the pyrolysis, of the net heat flux into the sample $\dot{q}_s''(0, t \le t_p)$ at the surface of the solid fuel sample.

Inserting the general solution for the surface temperature at all levels of incident heat fluxes and times Equation (33) into the simplified expression of the net heat flux $\dot{q}_s^{"}$ at the surface of the solid fuel sample as expressed by Equation (16) one gets:

$$\dot{q}_s^{"}(0, t \le t_p) = a\dot{q}_i^{"} - h_t \overline{T}\left[1 - e^{\frac{t}{t_c}} \operatorname{erfc}\left(\left(\frac{t}{t_c}\right)^{\frac{1}{2}}\right)\right] \tag{48}$$

By using simple mathematical transformation rules and Equation (31) the following expression, for the net heat flux $\dot{q}_s^{"}$ at the surface of the solid fuel sample prior to the pyrolysis, is obtained.

$$\dot{q}_s^{"}(0, t \le t_p) = h_t \overline{T}\left[e^{\frac{t}{t_c}} \operatorname{erfc}\left(\left(\frac{t}{t_c}\right)^{\frac{1}{2}}\right)\right] \tag{49}$$

At the time of pyrolysis t becomes t_p and therefore Equation (49) leads to:

$$\dot{q}_s^{"}(0, t_p) = h_t \overline{T}\left[e^{\frac{t_p}{t_c}} \operatorname{erfc}\left(\left(\frac{t_p}{t_c}\right)^{\frac{1}{2}}\right)\right] \tag{50}$$

A solution for Equation (50) can be found by focusing again on the two regions presented on Section 3.1.1.1. The first region would be where $t_p << t_c$ and the second region would be where $t_p >> t_c$.

For the **first region**, where $t_p << t_c$ it is reasonable to use the first order approximation presented in Equation (38). Therefore for the net heat flux $\dot{q}_s^{"}$ at the surface of the solid fuel sample is expressed by:

$$\dot{q}_s^{"}(0,t_p) = h_t \overline{T}\left[1 - \frac{2}{\sqrt{\pi}}\left(\left(\frac{t_p}{t_c}\right)^{\frac{1}{2}}\right)\right] \tag{51}$$

For the **second region** where $t_p >> t_c$ Equation (50) can be rewritten as Equation (52) and represents the net heat flux $\dot{q}_s^{"}$ at the surface of the sample

$$\dot{q}_s^{"}(0,t_p) = \frac{h_t \overline{T}}{\sqrt{\pi}}\left(\frac{t_p}{t_c}\right)^{-\frac{1}{2}} \tag{52}$$

3.1.2. Post Pyrolysis Processes $t \geq t_p$

The process described in this section relates to the mixing and induction process. Once the pyrolysis temperature T_p has been attained, chemical degradation of the solid sample occurs and gases begin to enter the boundary layer formed close to the surface of the material. Therefore Equation (12) looses its validity. Up to this point, the fuel sample is considered inert, but in the presence of pyrolysis the energy balance at the surface from Equation (12) changes according to Figure 25 to Equation (54), where the energy term $L_v \dot{m}_f^{"}$ needs to be added. This term accounts for the energy consumed by

the chemical degradation process (pyrolyze). To avoid confusion, for this analysis the time $t \geq t_p$ will be referred as the time τ which starts at zero when the time $t = t_p$.

$$t \geq t_p \quad \Rightarrow \quad t = \tau \quad \text{starting at } \tau = 0 \text{ when } t = t_p \tag{53}$$

$$\dot{q}''_s(0,\tau) = a\dot{q}''_i - \varepsilon\sigma\left(T^4(0,\tau) - T_\infty^4\right) - h_c\left(T(0,\tau) - T_\infty\right) - L_v\dot{m}''_f(0,\tau) \tag{54}$$

The fuel mass flux $\dot{m}''_f(0,\tau)$, is an average mass flow rate that does not take into account the structure of the boundary layer, thus is independent of length scale. This approximation is justified by the opposing effects of convective heat transfer h_c and convective mass transfer coefficient h_m on t_m which was verified by Long [LonR-98]. For the present work the mass flow rate of fuel will be determined by the energy balance at the surface.

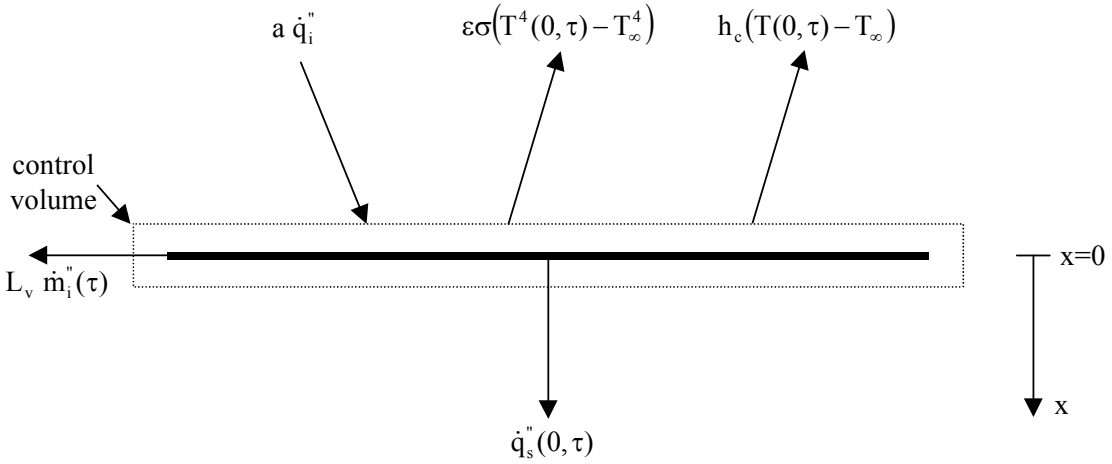

Figure 25 energy balance at the surface of the solid fuel sample after pyrolysis

As adressed in Section 3.1.1 and Equation (15), the linearized heat transfer coefficient h_t describes well the heating process, except for the reagion close to the critical heat flux for ignition. Thus Equation (54) can be written as follows and presented in Figure 26.

$$\dot{q}_s''(0,\tau) = a\dot{q}_i'' - h_t\left(T(0,\tau) - T_\infty\right) - L_v\dot{m}_f''(0,\tau) \tag{55}$$

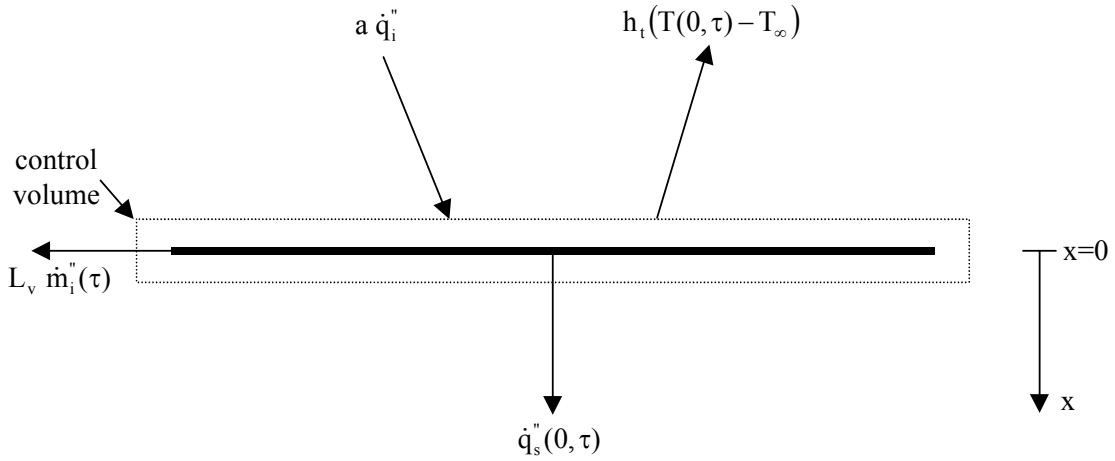

Figure 26 energy balance at the surface of the solid fuel sample after pyrolysis simplified with total heat transfer coefficient h_t

Where L_v is the heat of vaporization. After having attained the pyrolysis temperature T_p at the surface, it is assumed that the surface temperature T_s will remain at T_p because all the additional energy is used to sustain pyrolysis. The more energy is produced, the more material can be pyrolyzed.

Using the one dimensional heat diffusion equation, as stated in Equation (17), and assuming that there is no internal heat generation and the thermal conductivity is independent of the location the same governing energy equation (Equation (18)) can be used as presented in 3.1.1.

The initial condition at the surface is:

$$T(0,\tau) = T_p = T(0,t_p) \tag{56}$$

The surface condition at the pyrolysis time t_p is attained from the pre pyrolysis process expressed by the second boundary condition:

$$\dot{q}_s''(0,\tau=0) = -\lambda \left.\frac{\partial T}{\partial x}\right|_{x=0} = \dot{q}_s''(0,t_p) = \dot{q}_s''(0,t \le t_p) \tag{57}$$

While the third boundary condition for the temperature of the semi-infinite slab at $x = \infty$ is assumed to be

$$T(\infty,\tau) = T_\infty . \tag{58}$$

Conducting a change of variables with the following two expressions

$$\eta = x \cdot \sqrt{\frac{c_p \rho}{4\lambda\tau}} \tag{59}$$

$$\theta = \frac{T - T_\infty}{T_p - T_\infty} \tag{60}$$

Equation (18) can be rewritten as

$$\frac{\partial^2 \theta}{\partial \eta^2} = -2\eta \frac{\partial \theta}{\partial \eta}. \tag{61}$$

While the second and third boundary conditions become:

$$T(0,\tau) = T_p = T(0,t_p) \quad \Rightarrow \quad \theta(0,\tau) = 1. \tag{62}$$

$$T(\infty,\tau) = T_\infty \quad \Rightarrow \quad \theta(\infty,\tau) = 0. \tag{63}$$

Solving the ordinary homogeneous differential equation (Equation (61)) leads to

$$\theta = \operatorname{erfc}(\eta) \tag{64}$$

Which can be transformed with Equations (59)and (60) into

$$T(x,\tau) - T_\infty = (T_p - T_\infty)\operatorname{erfc}\left(x \cdot \sqrt{\frac{c_p \rho}{\lambda 4\tau}} \right). \tag{65}$$

3.1.2.1. Net Heat Flux Into the Sample ($\dot{q}_s''(0, t \geq t_p) = \dot{q}_s''(0,\tau)$)

To evaluate the mixing time t_m and the mass flow of fuel into the boundary layer requires the determination of the time evolution of the heat conducted into the

sample $\dot{q}_s''(0,\tau)$ as described in Figure 25. The temperature gradient in the sample material is given by:

$$\dot{q}''(x,\tau) = -\lambda \left.\frac{\partial T}{\partial x}\right|_{x=0} \tag{66}$$

Inserting Equation (65) into Equation (66) and conducting a differentiation leads to the Equation (67).

$$\dot{q}''(x,\tau) = \sqrt{\frac{\lambda c_p \rho}{\pi \tau}} \cdot \left(T_p - T_\infty\right) \cdot e^{-\frac{x^2 c_p \rho}{4\lambda\tau}} \tag{67}$$

Looking only at the surface of the sample material where $x = 0$ Equation (67) can be simplified to Equation (68).

$$\dot{q}_s''(\tau) = \dot{q}''(0,\tau) = \sqrt{\frac{\lambda c_p \rho}{\pi \tau}} \cdot \left(T_p - T_\infty\right) \tag{68}$$

Having obtained the time evolution for the net heat flux $\dot{q}_s''(\tau)$ into the sample it is now necessary to mach the starting point of this equation (Equation (68)) with the ending condition for the net heat flux $\dot{q}_s''(t = t_p)$ to guarantee a continuous function. This requires the incorporation of an artificial time shift τ^* so that net heat flux $\dot{q}_s''(\tau)$ and $\dot{q}_s''(t)$ are equal at the pyrolysis time t_p as presented in Equation (69).

$$\dot{q}_s''(\tau^*) = \dot{q}_s''(t = t_p) \tag{69}$$

Inserting Equation (69) into Equation (68) and finally solving the equation for the time τ leads to the following expression for the time shift.

$$\tau^* = \frac{c_p \rho \lambda}{\pi} \left(\frac{\left(T_p - T_\infty\right)}{\dot{q}_s''(t = t_p)} \right)^2 \tag{70}$$

The net heat flux $\dot{q}_s''(\tau)$ into the material therefore be expressed with Equation (71).

$$\dot{q}_s''(\tau) = \sqrt{\frac{\lambda c_p \rho}{\pi\left(\tau + \tau^*\right)}} \cdot \left(T_p - T_\infty\right) \tag{71}$$

3.1.2.2. Mixing Time (t_m)

Once the pyrolysis temperature T_p is attained, the fuel (vapors coming from the solid sample induced by the pyrolyze process) start flowing into the oxidizer boundary layer. Even though the mass flow rate of fuel increases with time from the beginning, reaches, after a while a constant level, and finally, when the fuel is us used up, decreases. The boundary layer can be considered steady state. The mixing time t_m, is the point in time from the onset of pyrolysis, when a flammable mixture is present, or, in other words, the concentration of fuel evolved from the surface of the sample has just reached a value equal to the concentration necessary to attain the lean (lower)

flammability limit (LFL). This can be obtained by using a pilot and measuring the ignition delay time [LonR-98].

The flammability limits, both upper and lower, are the values of the fuel and oxidizer mixture that will allow flame propagation. In the case of the lower flammability limit this is the point where a minimum amount of fuel has mixed with the oxidizer entrained in the boundary layer that creates a "flammable" mixture that will propagate flaming.

It is important to note that the characteristic time required for the fuel to migrate from the sample surface to the pilot location is neglected. Therefore the lean flammability limit corresponds to the time at which the necessary mass of fuel to create a flammable mixture is evolved from the surface of the sample. Characteristic values for the velocity in the natural convection boundary layer are approximately 0.5 m/s thus justifies this assumption. Nevertheless, very high heat fluxes might lead to errors, since the characteristic times for mixing and pyrolysis are very small.

The lean (lower) flammability limit can be expressed by the mass fraction of fuel in the boundary layer at the location of the pilot. Where the mass fraction of fuel in the boundary layer is expressed as the ratio of the mass of fuel to the mass of the mixture, fuel and oxidizer. Therefore the mass fraction of fuel Y_f is given by the following equation:

$$Y_f = \frac{\dot{m}_f'}{\dot{m}_f' + \dot{m}_o'} \tag{72}$$

The determination of the mass flow rate of fuel $\dot{m}_f'$ and mass flow rate of oxidizer $\dot{m}_o'$ entrained can be used to calculate the mass fraction of fuel Y_f. When having attained the mass fraction of fuel Y_f in can be compared to the stoichiometric fuel mass fraction $Y_{f,stoic}$ for the particular tested.

The **stoichiometric fuel mass fraction** $Y_{f,stoic}$ can be determined by writing a equilibrium equation. The following equation (Equation (73)), is a general expression which can be used for a variety of different materials reacting in air.

$$C_a H_b O_d + x\left(O_2 + \frac{x_{N_2}}{x_{O_2}} N_2\right) \rightarrow a\ CO_2 + \left(\frac{1}{2} b\right) H_2O + \frac{x_{N_2}}{x_{O_2}} x\ N_2 \tag{73}$$

Where the concentration of oxygen and nitrogen in air is:

$$x_{O_2} = 0.21 \tag{74}$$

$$x_{N_2} = 0.79 \tag{75}$$

Using equation

$$x = a + \frac{1}{4} b - \frac{1}{2} d \tag{76}$$

leads to the following general stoichiometric fuel mass fraction $Y_{f,stoic}$

$$Y_{f,stoic} = \left[\frac{m_f}{m_f + m_{air}}\right]_{stoic} = \frac{a(M_C) + b(M_H) + d(M_O)}{a(M_C) + b(M_H) + d(M_O) + x\left(M_{O_2} + \frac{x_{N_2}}{x_{O_2}} M_{N_2}\right)}. \quad (77)$$

For Methymethacrylate (MMA), the pyrolysis product of Poly(methyl Methacrylate) (PMMA), Equations (77) is:

$$Y_{C_5H_8O_2,stoic} = \frac{5(M_C) + 8(M_H) + 2(M_O)}{5(M_C) + 8(M_H) + 2(M_O) + 6\left(M_{O_2} + \frac{0.79}{0.21} M_{N_2}\right)} = 0.1083 \quad (78)$$

To calculate the **mass fraction of fuel** Y_f the fuel mass flow rate $\dot{m}_f^{'}(t)$ and the mass flow rate of the oxidizer $\dot{m}_o^{'}(t)$ need to be determined.

The **fuel mass flow rate** $\dot{m}_f^{'}(t)$ can be obtained by rearranging Equation (55) and solving for the mass fuel flow rate $\dot{m}_f^{''}(0, t \geq t_p) = \dot{m}_f^{''}(0, \tau)$ evolving from the sample surface after the pyrolysis time t_p, leading to

$$\dot{m}_f^{''}(0,\tau) = \frac{a\dot{q}_i^{''} - h_t\left(T_p - T_\infty\right) - \dot{q}_s^{''}(0,\tau)}{L_v}. \quad (79)$$

If the length of the sample is L and the total mass flow per unit length if $\dot{m}_f^{'}(\tau)$

$$\dot{m}_f'(\tau) = \dot{m}_f''(\tau) \cdot L \tag{80}$$

Typical curves of the fuel mass flow rate $\dot{m}_f''(0,t)$ for varying levels of incident heat flux are shown in (Figure 27). No fuel evolves ($\dot{m}_f''(0, t < t_p) = 0$) before the pyrolysis time t_p and then, at the pyrolysis time t_p, the mass of fuel evolved increases ($\dot{m}_f''(0, t \geq t_p) = \dot{m}_f''(0,\tau)$) leading to an eventual plateau, as can be illustrated from Figure 27, where there the pyrolysis time was determined using Equation (41).

As one can observe from Figure 27 the reduction of the incident heat flux $\dot{q}_i''$ leads to a lower mass flow rate $\dot{m}_f''(0,\tau)$ and to a slower rate of increase of $\dot{m}_f''(0,\tau)$. The values of $\dot{m}_f''(0,\tau)$ obtained by means of Equation (79) match well values previously reported by other authors for PMMA such as [QuIq-94] and [StKB-3].

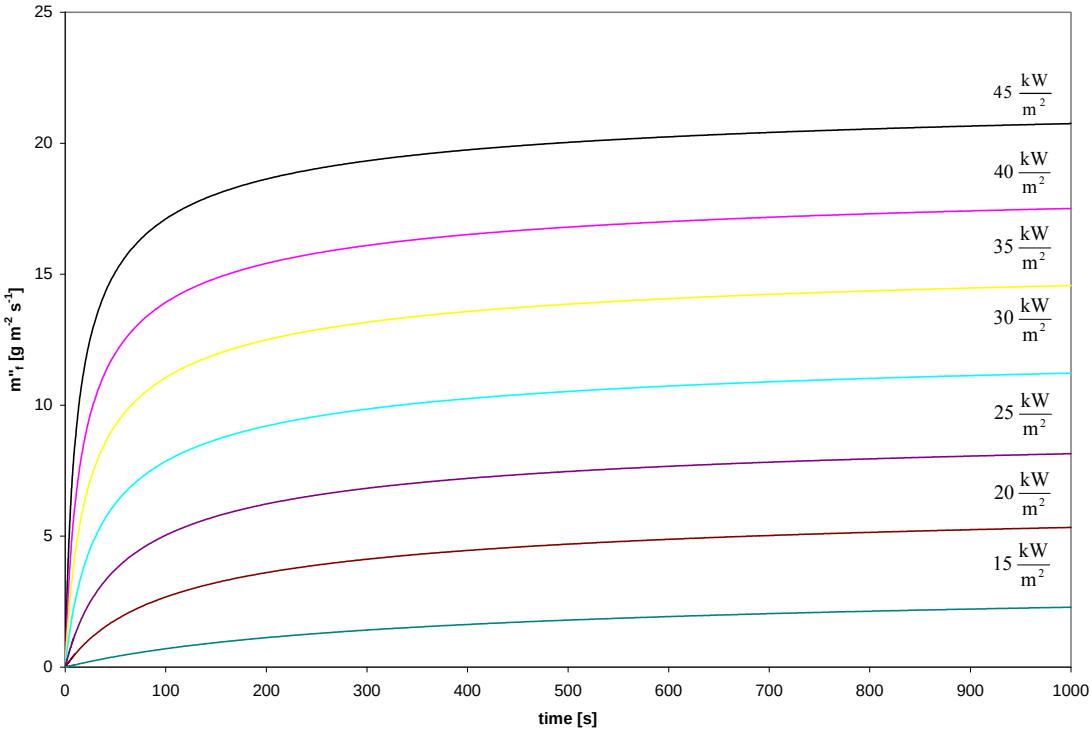

Figure 27 mass flow rate of fuel as a function of incident heat flux

In order to evaluate the **oxidizer mass flow rate** $\dot{m}_o'$, the mass of oxidizer entrained in the boundary layer at the location of the pilot can be solved with a classical integral approach that solves the energy and momentum equations simultaneously [BejA-84].

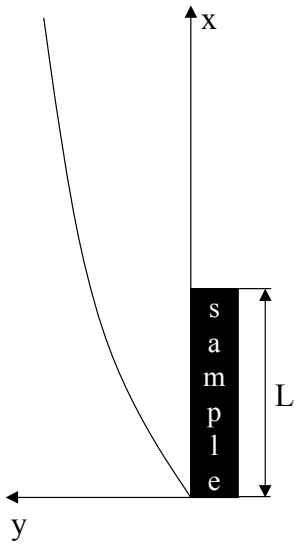

Figure 28 natural convection problem

Conducting an integral analysis over the boundary layer thickness by using the Integral form of the energy and momentum equations one obtains the following expressions, where Equation (81) is the conservation of energy and Equation (82) the conservation momentum.

$$\frac{\partial}{\partial x}\int_{o}^{\delta} u\left(T_{\infty}-T\right)dy=\frac{\lambda}{c_{p}\rho}\frac{\partial T}{\partial y}\bigg|_{y=0} \tag{81}$$

$$\frac{\partial}{\partial x}\int_{0}^{\delta} u^{2}dy=-\nu\frac{\partial u}{\partial y}\bigg|_{y=0}+g\beta\int_{0}^{\delta}\left(T-T_{\infty}\right)dy \tag{82}$$

Assuming that the Prandtl Number $Pr \approx 1$ thus the momentum boundary layer thickness δ equals approximately the thermal boundary layer thickness δ_t.

$$\mathrm{Pr} \approx 1 \quad \Rightarrow \quad \delta \approx \delta_t \tag{83}$$

The following two equations express the velocity $u(x,y)$ and temperature $T(x,y)$ condition in a Squire type profile [BejA-84], where u_c is defined as a characteristic velocity in the vertical direction.

$$T(x,y) - T_\infty = \left(T_p - T_\infty\right)\left(1 - \frac{y}{\delta}\right)^2 \tag{84}$$

$$u(x,y) = u_c\left(\frac{y}{\delta}\right)\left(1 - \frac{y}{\delta}\right)^2 \tag{85}$$

Inserting the two profiles into Equations (81) and (82), integrating over the boundary layer thickness and differentiating the right hand side results in the two following differential equations.

$$\frac{d}{dx}\left(\delta u_c\right) = 60\frac{\lambda}{\delta c_p \rho} \tag{86}$$

$$\frac{1}{105}\frac{d}{dx}\left(u_c^2\delta\right) = \frac{-\nu u_c}{\delta} + g\beta\frac{\left(T_p - T_\infty\right)}{3}\delta \tag{87}$$

To solve the two above described differential equations, the following expressions for characteristic velocity u_c Equation (88) and boundary layer thickness δ Equation (89) can be assumed [JalY-80 and SaGr-75].

$$u_c = U\, x^{\frac{1}{2}} \tag{88}$$

$$\delta = C\, x^{\frac{1}{4}} \tag{89}$$

With $\alpha = \dfrac{\lambda}{c_p}$ and $Pr = \dfrac{\upsilon}{\alpha}$ leading to the following expressions for U and C

$$U = \left[g\beta\left(T_p - T_\infty\right)\frac{\frac{80}{3}}{\frac{20}{21} + Pr} \right]^{\frac{1}{2}} \tag{90}$$

$$C = \left[\frac{240\left(\frac{20}{21} + Pr\right)}{\frac{g\beta c_p^2 \rho^2 \left(T_p - T_\infty\right)}{\lambda^2}} \right]^{\frac{1}{4}} = \left[\frac{240\left(\frac{20}{21} + \frac{\nu}{\lambda}\right)}{\frac{g\beta c_p^2 \rho^2 \left(T_p - T_\infty\right)}{\lambda^2}} \right]^{\frac{1}{4}} \tag{91}$$

Having found a solution for the velocity $u(x,y)$ the oxidizer mass flow $\dot{m}_o''(x)$ can be evaluated by integrating the mass of oxidizer across the boundary layer with the following equation:

$$\dot{m}_o'(x) = \int_0^\delta \rho u(x,y)\, dy \tag{92}$$

giving:

$$\dot{m}_o'(x) = \frac{\rho}{12}\left[g\beta\left(T_p - T_\infty\right)\frac{\frac{(80)^3}{3}\frac{\lambda^2}{c_p^2\rho^2}}{\frac{20}{21}+\mathrm{Pr}}\right]^{\frac{1}{4}} x^{\frac{3}{4}} \tag{93}$$

A typical evolution of $\dot{m}_o'(x)$ as a function of the distance from the leading edge x is presented in Figure 29.

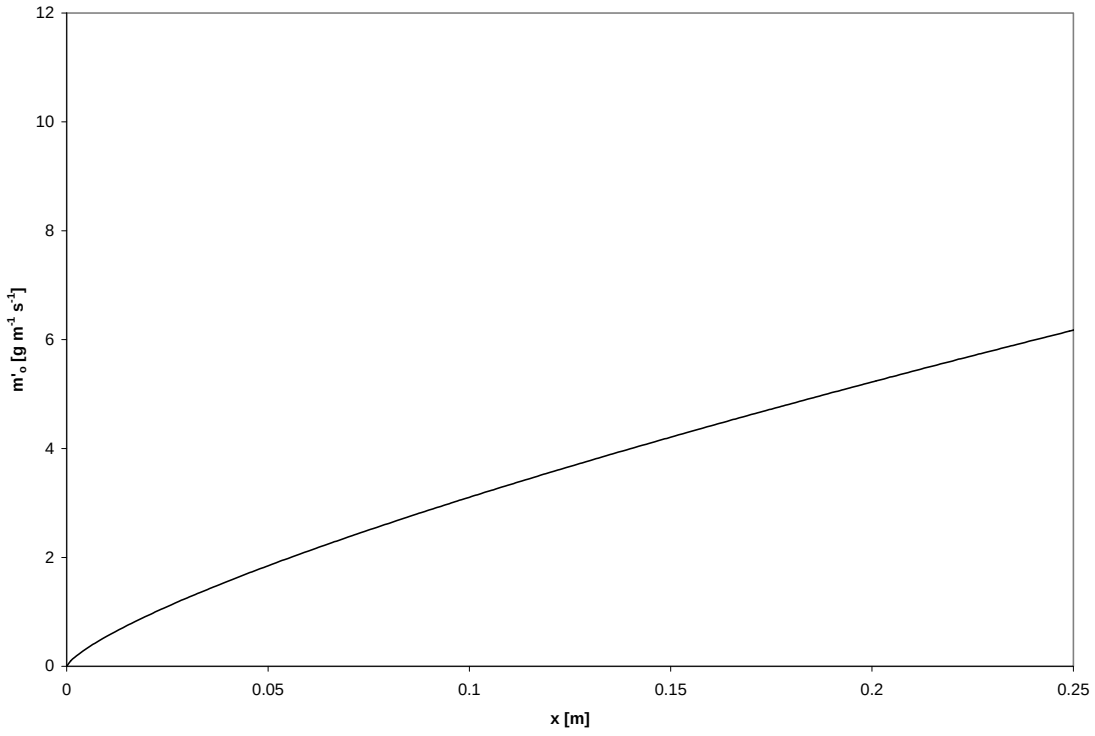

Figure 29 mass flow rate of oxidizer as a function of the characteristic length scale

After having determined the fuel mass flow rate $\dot{m}_f'(\tau)$ and the mass flow rate of the oxidizer $\dot{m}_o'(x)$ it is time to go back and calculate mass fraction of fuel Y_f. Inserting Equation (79) and Equation (93) into Equation (72) one obtains the time

dependent mass fraction of fuel $Y_f(\tau)$ at the pilot location. With this, an evaluation of the fuel concentration at the onset of ignition is plausible. When the time dependent mass fraction of fuel $Y_f(\tau)$ has reached the threshold fuel mass fraction at the pilot, it's strong flame heats up the fuel oxidizer mixture so fast that when the mixture has reached this concentration immediate ignition occurs.

3.1.2.3. Induction Time (t_i)

The induction time is the last of the three parameters influencing the ignition time t_{ig}. As defined earlier it is the time period, after having attained a flammable mixture, to heat up till it ignites. Unfortunately this process is a complex combination of fuel properties and flow characteristics therefore a theoretical contemplation is left aside. It is common knowledge, that when a very strong energy source is supplied an immediate ignition occurs. For the later analysis where a comparison with Long's data [LonR-98] is conducted, the induction time t_i will be neglected for the further analysis.

3.2. Thermography

The intention to use an infrared camera to measure the temperatures of objects, thermography, requires some theoretical background, which is being supplied below. The fact that all objects, at any temperature above absolute zero, vibrate and therefore emit electromagnetic waves depicts the basis on which thermography works.

The electromagnetic spectrum, as shown in Figure 30, is divided into a number of wavelength regions, the so called bands, distinguished by the methods utilized to produce and detect the radiation. The visible

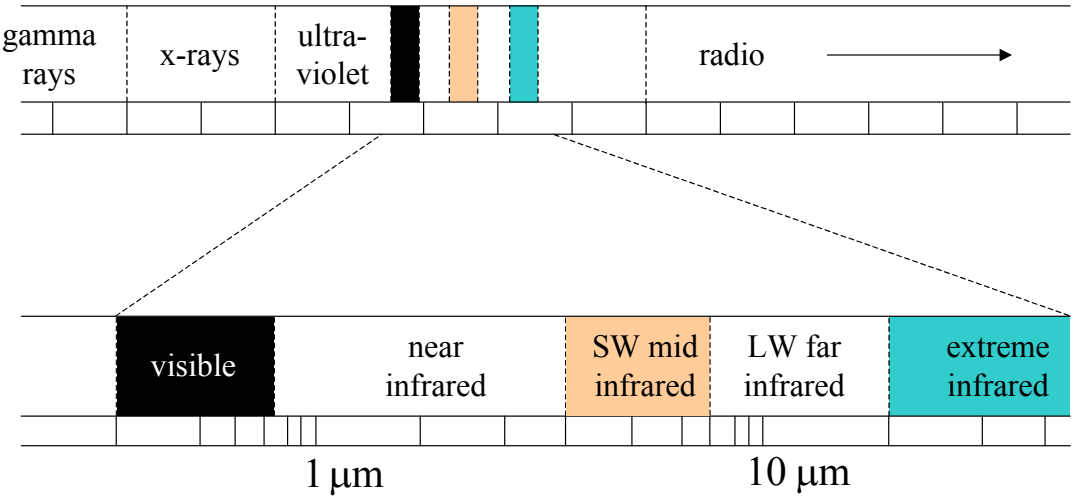

Figure 30 electromagnetic spectrum

No fundamental difference exists between the radiation in the different bands, meaning that the same laws govern them. The only differences are that they differ in wavelength. Commonly the infrared band itself is further subdivided into smaller bands, which are named the near infrared (0.75-3 μm), the middle infrared (3-6 μm), the far infrared (6-15 μm) and the extreme infrared (15-100 μm). Although the wavelengths are usually given in μm (micrometers), other units are often used such as microns (μ), manometers (nm) and Ångströms (Å). Their relationships is:

$$10{,}000\text{Å} = 1{,}000\ \text{nm} = 1\mu = 1\,\mu\text{m} \tag{94}$$

Sometimes the wavelength λ is also represented in a slightly different form, which is derived from the wavelength in micrometers [μm] and has the unit $\left[\frac{1}{\text{cm}}\right]$.

Generally, a part of the energy transported by radiation to the surface of an object, which impinges on the object's surface (Figure 31) will be reflected, absorbed or transmitted.

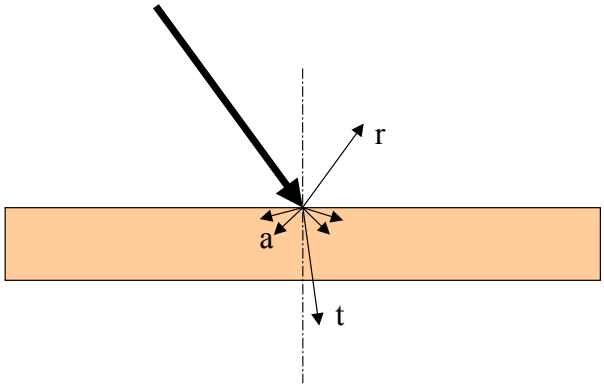

Figure 31 reflection, absorption, and transmission

This phenomenon can be expressed in the following equation:

$$r + a + t = 1 \tag{95}$$

or

$$r_\lambda + a_\lambda + t_\lambda = 1 \tag{96}$$

Where r is the reflectance a is the absorptance, t is the transmittance and the subscript λ infers that it is only valid for one wavelength. The sum of these three factors must always add up to the whole (impinging energy) at any wavelength or one particular wavelength depending on the used equation. E.g. an opaque materials where

$$t = 0$$

Equation (95) becomes:

$$r + a = 1$$

For a blackbody, that is defined as an object which absorbs all radiation that impinges on it at any wavelength, the reflectance and transmittancent (r and t) equal to zero ($r = 0$ and $t = 0$). Therefore Equation (95) can be rewritten to

$$a = 1 \tag{97}$$

According to Kirchhoff's Law (Equation (98) where ε is the spectral emissivity and a is the spectral absorptance) the black body is not only capable of absorbing all radiation that impinges on it at any wavelength, it is also equally capable in the emission of radiation.

$$\varepsilon = a \quad \text{or} \quad \varepsilon_\lambda = a_\lambda \tag{98}$$

Such a black body, which does not exist on earth, but can be idealized, is usually used to generate blackbody radiation to calibrate thermographic instruments. The construction of such a blackbody source is in principle very simple. A box (isotherm cavity) that is light tight except for a small opening on one sides can be used (Figure 32), where the inside of that isotherm cavity is made of an opaque absorbing material. Therefore any radiation, which enters the hole, is scattered and absorbed by repeated reflections so only an infinitesimal fraction can possibly escape (Figure 32). The obtained blackness is nearly equal to that of a blackbody and almost perfect for all wavelengths.

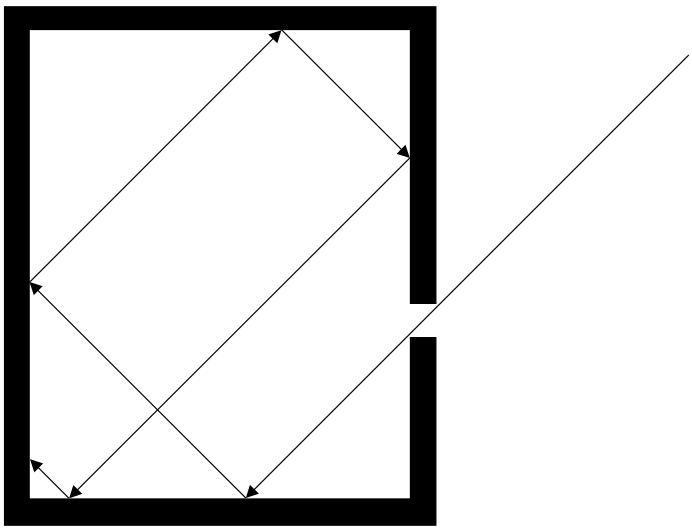

Figure 32 black body

When such a black body is heated to a uniform temperature it generates blackbody radiation coming out of the hole, which is typical for that specific temperature. The blackbody radiation obtained at a certain temperature serves as a reference radiation.

The radiation emitted from a black body can be described by means of Planck's law. Max Plank ascertains the radiation energy for the varying wavelengths due to the quantum theory. Where the natural (unpolarized) black body, radiates at wavelength λ perpendicular to the black wall of temperature T the black body b spectral radiant emittance $I_{b,\lambda,T}$ is

$$I_{b,\lambda,T}(\lambda, T) = \frac{h \cdot c^2}{\lambda^5} \frac{2}{e^{\frac{h \cdot c}{k \cdot \lambda \cdot T}} - 1}, \tag{99}$$

where

Symbol	Description	Value	Unit
c	Velocity of light	$2.9978 \cdot 10^8$	$\frac{m}{s}$
h	Planck's constant	$6.6252 \cdot 10^{-34}$	J s
k	Boltzmann's constant	$1{,}38034 \cdot 10^{-23}$	$\frac{J}{K}$
T	Absolute temperature of a black body		K
λ	Wavelength		m

Table 3 parameter in of Planck's law

When spectral radiant emittance $I_{b,\lambda,T}$, from the Planck's formula, is plotted graphically for various temperatures, against the wavelength λ, the result is a family of curves as presented in Figure 33. If one follows any Planck curve, the spectral emittance is zero at $\lambda = 0$, then increases rapidly to a maximum and after passing it approaches

zero again at very long wavelengths, the higher the temperature, the shorter the wavelength at which maximum emittance occurs.

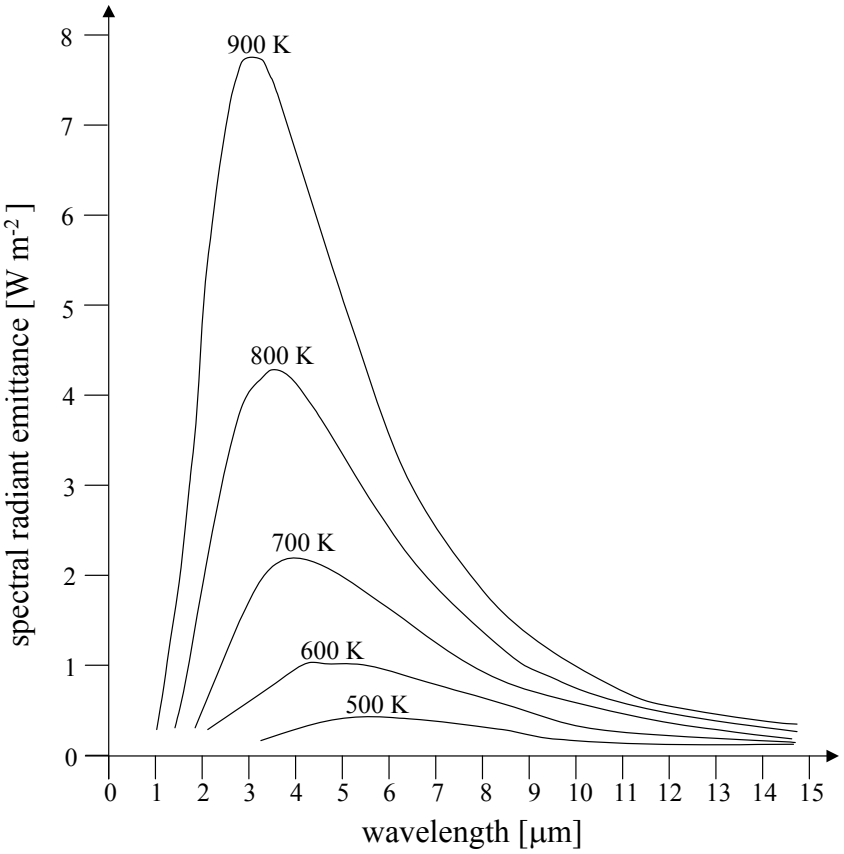

Figure 33 spectral radiant emittance of a black body

Up to this point, the discussion dealt mainly with blackbody radiators, which describe an ideal case for thermography. Unfortunately real objects behave differently and therefore a temperature analysis becomes more complicated.

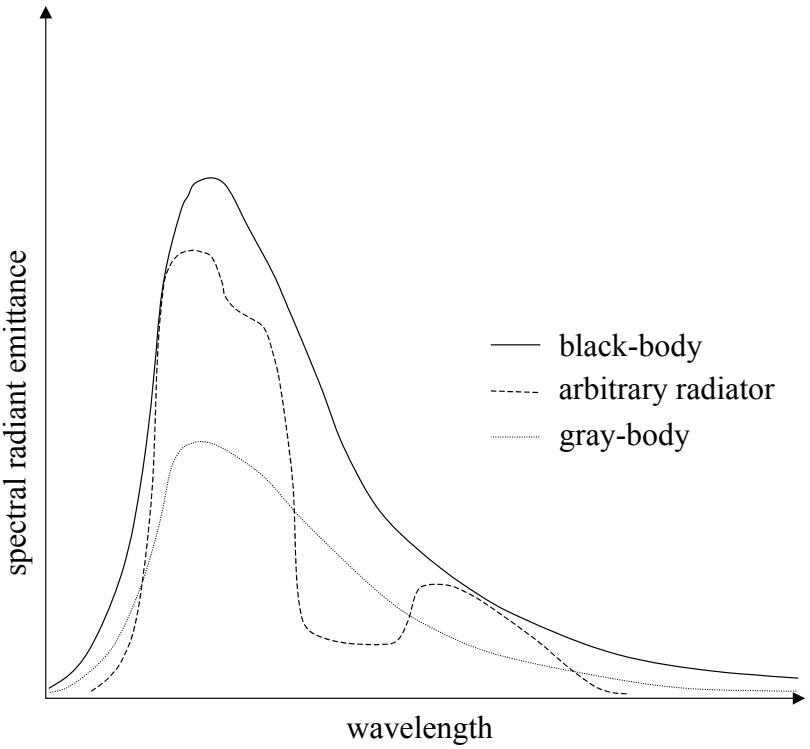

Figure 34 spectral radiant emittance

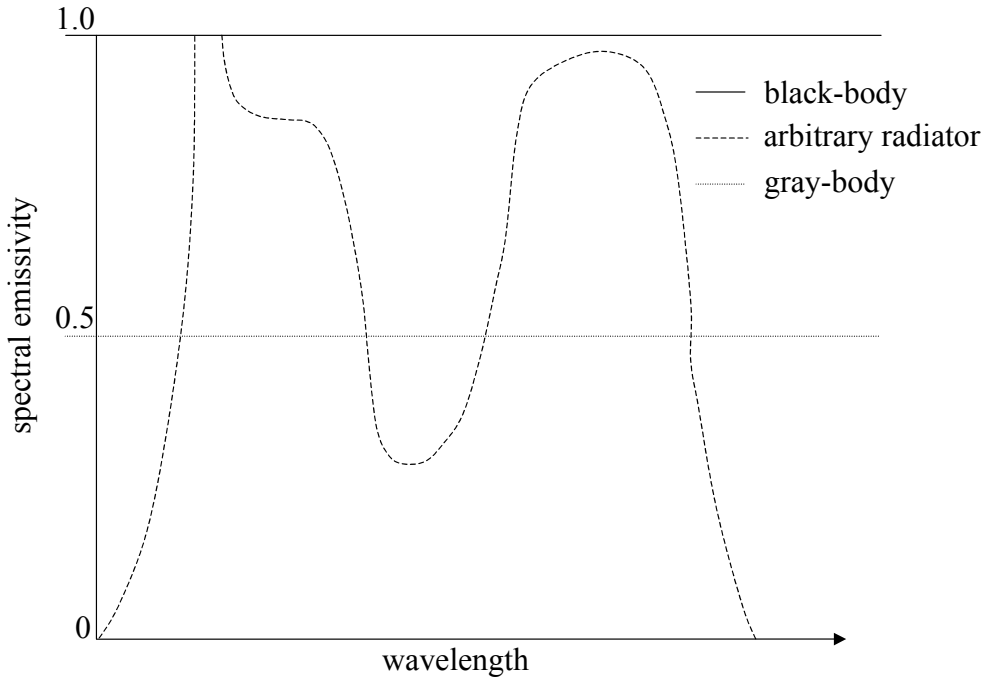

Figure 35 spectral emissivity

As can be seen from Figure 34 and Figure 35 real objects however, almost never comply with these laws over an extended wavelength region, but a blackbody behavior, in certain spectral intervals, can be observed, which makes it possible to treat the observed object in that specific wavelength range as a black body.

As mentioned above (Equation (95)), the two processes which prevent a real object from acting like a black body (Equation (97)) are the

- reflection, expressed by the reflectance coefficient r, and
- transmission, expressed by the transmittance coefficient t.

As inferred above and what can be seen from Figure 34 and Figure 35 all of the factors of Equation (95) are more-or-less wavelength dependent. Choosing a wavelength typical for specific material, where the transmittance is zero ($t_\lambda = 0$), and using a material, which is at the same wavelength not reflecting ($r_\lambda = 0$) Equation (96) can be rewritten to

$$a_\lambda = 1. \tag{100}$$

The determination where the transmittance is almost zero can be obtained, by a measurement technique called infrared spectroscopy (Section 4.7), however if the

transmittance has a significant value, the value for the transmittance coefficient for that wavelength t_λ has to be used in Equation (96).

The spectral radiant power emitted from real objects $\dot{E}\left[\frac{W}{m^2}\right]$ is always smaller than spectral radiant power emitted from a black body $\dot{E}_b\left[\frac{W}{m^2}\right]$ ($\dot{E} < \dot{E}_b$). This relationship is expressed by the following equation

$$\frac{\dot{E}}{\dot{E}_b} = \varepsilon \tag{101}$$

where ε is the spectral emissivity. Generally three types of radiation source, distinguished by the ways in which the spectral emittance of each varies with wavelength can be distinguished (Figure 35).

1. A blackbody, for which $\varepsilon = 1$
2. A graybody, for which ε is constant but $\varepsilon > 1$
3. A selective radiator, for which $\varepsilon > 1$ but varies with wavelength

According to Kirchhoff's Law (Equation (98)), for any material the spectral emissivity and spectral absorptance of a body are equal to any specified temperature and wavelength. Therefore, when choosing a wavelength typical for specific material where

the transmittance is zero ($t_\lambda = 0$) and using a material, which is at the same wavelength not reflecting ($r_\lambda = 0$) as presented in Equation (100) this equation becomes

$$a_\lambda = 1 = \varepsilon_\lambda . \tag{102}$$

For the above described case, or the general case from Equation (96) using the Kirchhoff's Law (Equation (98)) the following equation (Equation (103)) leads to a value for the emissivity coefficient ε.

$$r_\lambda + \varepsilon_\lambda + t_\lambda = 1 \tag{103}$$

Knowing the emissivity coefficient either all wavelengths ε or a single wavelength ε_λ finally leaves us with the ability to conduct thermography measurements with an infrared camera.

3.3. Least Square Best Fit Analysis

The lest square best fit analysis is a standard mathematical procedure to find the best fitting curve to a given set of points, as presented in Figure 36 and Figure 37.

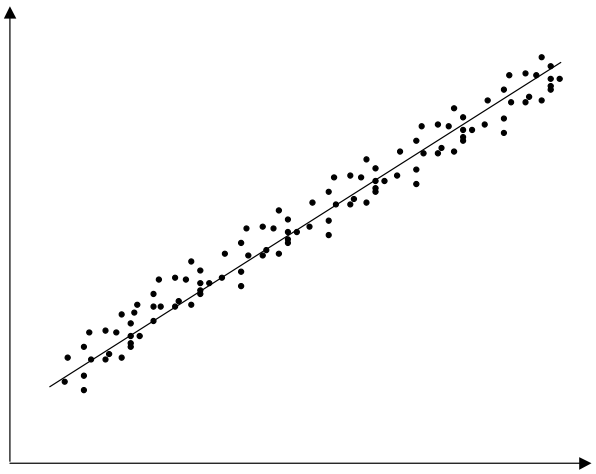

Figure 36 linear least square fit

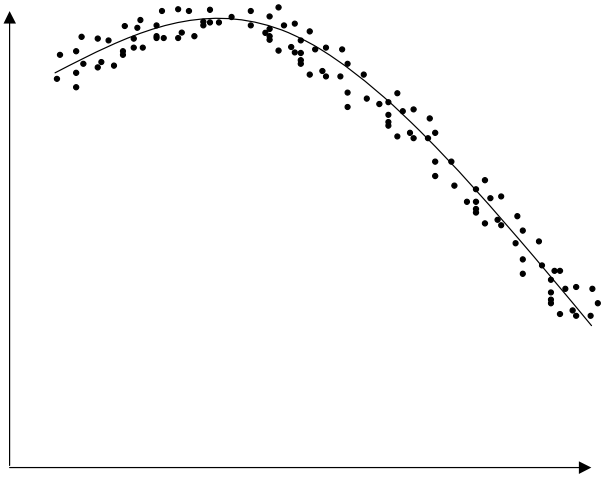

Figure 37 nonlinear least square fit

Finding the best fitting curve to a given set of points is obtained by the minimization of the sum of the squares of the offsets of the points from the curve. Taking the sum of the squares of the offsets was chosen instead of the offset absolute values, due to the fact, that this allows the residuals to be treated as a continuous differentiable quantity. This way of obtaining a best fitting curve is for most cases reasonable however, the usage of squares of the offsets, can have a disproportionate

effect on the curve fit, which may or may not be desirable. Looking at the offsets the question might arise, which kind of offset is generally used, the vertical (Figure 38), horizontal (Figure 39) or perpendicular offset (Figure 40).

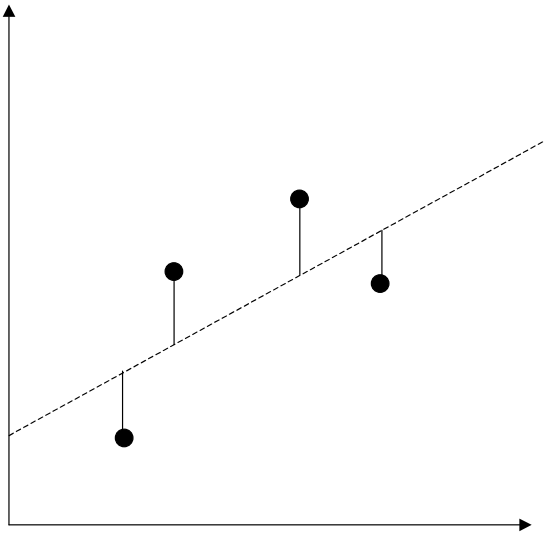

Figure 38 vertical offset

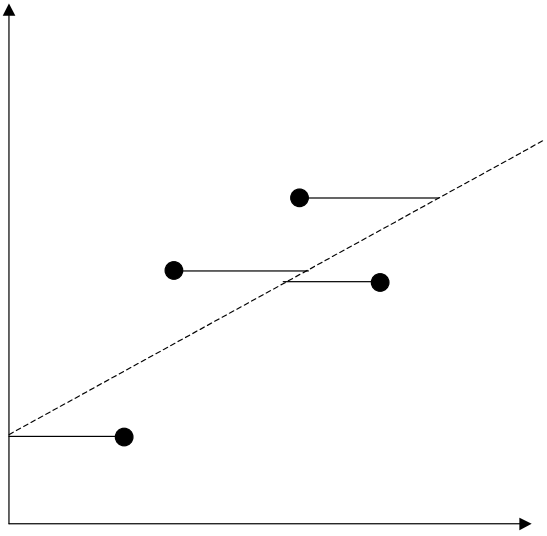

Figure 39 horizontal offset

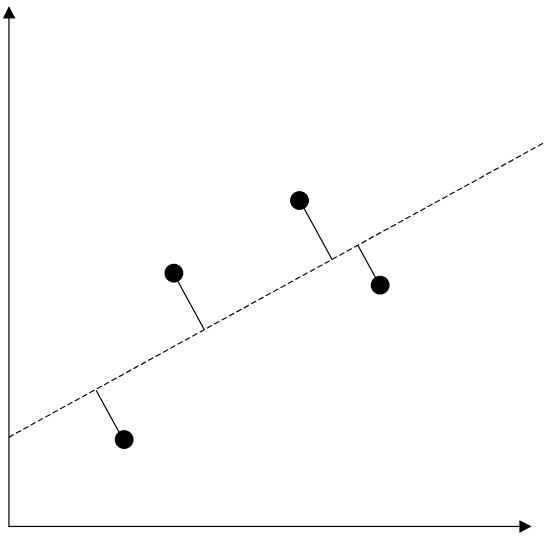

Figure 40 perpendicular offset

Generally the vertical offsets are used, which allows a much simpler analysis for the fitting parameters and allows uncertainties of the data points along the x- and y-axes to be simply incorporated.

The least square best fit analysis can be divided into two main groups, the

- linear least squares fitting technique and
- nonlinear least squares fitting.

Where the linear least squares fitting technique is the simplest and most commonly used technique, which provides a solution of the best fitting straight line through a set of points. This is also the technique, used in this work. As has been shown, it common practice even when the relationship between two quantities do not show a linear behavior, a transformation (exponential, logarithmic, power

transformations) of the data is conducted in such a way, that one ends up with linear relation to use the linear least squares fitting technique.

4. Material Properties

4.1. Objectives

The FIST Project (**F**orced flow **I**gnition and flame **S**pread **T**est) relies on a theoretical foundation that assumes a global set of material thermal properties to solve a heat transfer equation with appropriate boundary conditions that will lead to a surface temperature at ignition T_{ig}. As previously mentioned in the theory section, this work concentrates on two aspects of the piloted ignition problem, the validity of the $T_{ig} \approx T_P$ (T_p is the pyrolysis temperature) and thus, $t_{ig} \approx t_P$, assumptions and the global thermal property hypothesis as an adequate representation of the heating process. This section will address the material thermal properties. The material of choice for this work is Poly(methyl methacrylate) commonly referred as PMMA. The reason for this choice is the presumed adequate characterisation of this material thermal properties.

The general energy equation for the transient heating of a semi-infinite one-dimensional solid with variable thermal properties is given by

$$\frac{\partial}{\partial x}\left(\lambda(T)\frac{\partial T}{\partial x}\right) = \frac{\partial\left(\rho(T)c_p(T)T\right)}{\partial t} \tag{104}$$

with the initial condition of the form

$$T(t=0) = T_\infty \tag{105}$$

and the boundary conditions at $t > 0$ as well as $x = 0$ of the form

$$-\lambda(T)\frac{\partial T}{\partial x} = \dot{q}''_{net} = a(T)\dot{q}''_i - h_c(T)(T - T_\infty) - \varepsilon(T)\sigma(T^4 - T_\infty^4) \tag{106}$$

the above system of equations has no analytical solution therefore, by assuming global thermal properties the problem can be simplified to:

$$\bar{\lambda}\frac{\partial^2 T}{\partial x^2} = \bar{\rho}\bar{c}_p\frac{\partial T}{\partial t} \tag{107}$$

with the same initial condition as described in Equation (105) and boundary conditions of the form

$$-\bar{\lambda}\frac{\partial T}{\partial x} = \dot{q}''_{net} = \bar{a}\dot{q}''_i - \bar{h}_c(T - T_\infty) - \bar{\varepsilon}\sigma(T^4 - T_\infty^4) = \bar{a}\dot{q}''_i - \bar{h}_t(T - T_\infty) \tag{108}$$

where $\bar{\lambda}$, $\bar{\rho}$, $\bar{c}_p$, $\bar{a}$, $\bar{\varepsilon}$, $\bar{h}_C$, and $\bar{h}_t$ are the global thermal properties which include the additional assumption of a global linearized heat transfer coefficient $\bar{h}_T$. This

approach leads to the following solution for the time necessary to attain the pyrolysis temperature T_p at the surface,

$$\frac{1}{\sqrt{t_P}} = \frac{2}{\sqrt{\pi}} \frac{\bar{a}}{\sqrt{\bar{\lambda}\bar{\rho}\bar{c}_p}} \frac{\dot{q}_i''}{(T_P - T_\infty)} \tag{109}$$

which under the further assumption of the absorptivity close to unity, $\bar{a} \approx 1$, leaves the global property, $\overline{\lambda\rho C}$, as the single parameter determining the time for attainment of pyrolysis. Details of these formulations, the development and their limitations are described in the theory section.

Experimental determination of the pyrolysis temperature and time allows a single value for the thermal inertia $\overline{\lambda\rho C}$ to be extracted. The ultimate use of the information provided in this section will be the numerical modelling of Equation (104) with temperature dependent properties and by curve-fitting Equation (106) to the data and the numerical solution fully validate this approach.

Poly(methyl methacrylate) **(PMMA)**, better known under the trade mark name Plexiglas, was chosen as a sample material due to its wide uses in fire tests and therefore it's well-known fire related and non fire related properties. The following sections will provide information on poly(methyl methacrylate) which will serve to better understand the behaviour of PMMA in the heating process.

4.2. Introduction to Polymers

4.2.1. General Notions

Polymers, to which material group poly(methyl methacrylate) belongs, are often used as a synonym for "plastic". The word polymer, which includes already a short description in itself, is Greek and is a combination of the word "poly" which means many, and "meros" which means parts. If those two words are used together, one can say, that a polymer consists of a group of many single meros (monomers) or, in english, parts. Therefore, a polymer is a large molecule built by the repetition of small, simple chemical units (e.g. single atoms or molecules) as shown in Figure 41.

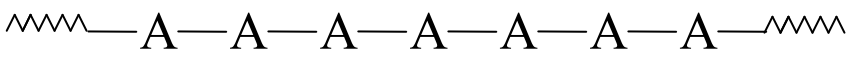

Figure 41 line polymer made out of "A" atoms

In most cases the repetition is linear, in other cases the chains are branched or interconnected to form three-dimensional networks. The repeat structure of the polymer is usually equivalent or nearly equivalent to the monomer, or starting material from which the polymer is formed (Figure 44). The number of repeated structures in the chain specifies the length of the polymer chain, which is called the degree of polymerization. This fact leads to a more difficult determination of the material properties such as the molecular weight, because they depend on the polymer chain. The

molecular weight of the polymer e.g. is the product of the molecular weight of the repeat structure and the degree of polymerization.

4.2.2. Polymerization

The formation of larger molecules from smaller ones is known as the polymerization process. The polymerization process produces in some type of plastics a cross-linking between long chain molecules. This has a significant effect on the characteristics of the plastic. Therefore the polymerization process can be divided into two groups, the cross-linked and not cross-linked polymerization.

Cross-linkage produces **thermosetting** plastics with the characteristic, that they are hardened permanently by heat.

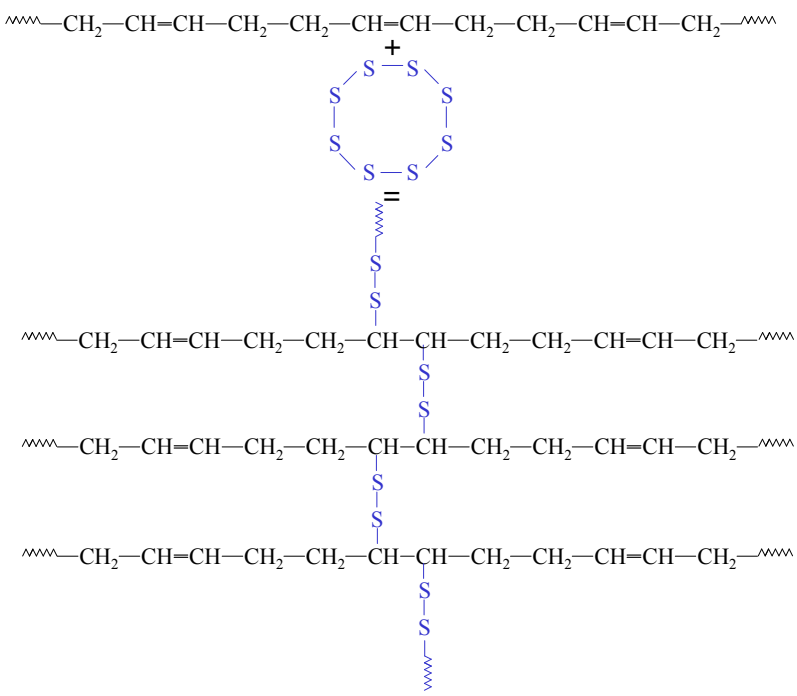

Figure 42 cross-linkage of sulfur atoms with polyisoprene to create a supermolecule

That means, that these plastics will remain permanently hard and will not soften upon subsequent heating. Typical thermosetting plastics are polyesters, amines, and urethanes. Another group of cross-linked plastics are the **elastomers**, such as rubber, they can be stretched to many times their initial length and still spring back to their original length when released.

Plastics which are not cross-linked are known as **thermoplastics**. Their major advantage is that they can be softened upon heating and hardened upon cooling. This cycle can be repeated indefinitely. Examples of thermoplastics are polyamides, polyethylenes, polystyrenes and poly(methyl methacrylate).

Many polymers, including most fibers, are partially crystalline but never fully crystalline.

4.2.3. The Entanglement of Polymer Chains

As mentioned earlier, most polymers are linear polymers. Generally, this chain is not stiff and straight, but is flexible. It twists and bends around to form a tangled mesh and the different structures tend to twist and wrap around each other, so the polymer molecules collectively will form one large tangled mesh.

Removing an individual strand is possible when the polymer is molten, but when polymers are cold, and in the solid state, it is very difficult to remove any particular strand. It is more likely, that one would end up having a coil in hand instead of one strand. The chains of solid polymers are all tangled up in each other and it is difficult to untangle them, this is what provides the strength of the polymer. Intermolecular forces affect polymers in the same way as small molecules, but are greatly compounded in polymers. That means, that the bigger the molecule is, the more mass there is to exert an intermolecular force. Even weak Van der Waals forces can be very strong in binding different polymer chains together.

4.3. Poly(methyl methacrylate) PMMA

4.3.1. Generalities

Poly(methyl methacrylate) (Figure 43), which is commonly referred to as PMMA is commonly called by it's trade mark name PLEXIGLAS™. In the chemical literature, it could also be listed as "2-propenoic acid, 2-methyl-, esters, methylester, homopolymer" or under the Chemical Abstract Number CAS [9011-14-7].

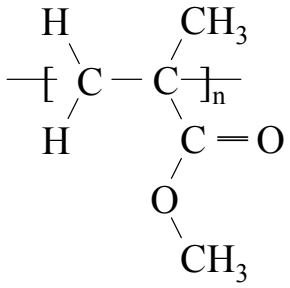

Figure 43 PMMA

As mentioned above, PMMA is a polymer and therefore has undergone a polymerization process. In this particular case no cross-linking exists between long chain molecules therefore can be considered a thermoplastic. PMMA is a vinyl polymer therefore it is composed of vinyl monomers; that is, molecules containing carbon-carbon double bonds. PMMA is thus the product of the polymerization of free vinyl radicals called methyl methacrylate (Figure 44).

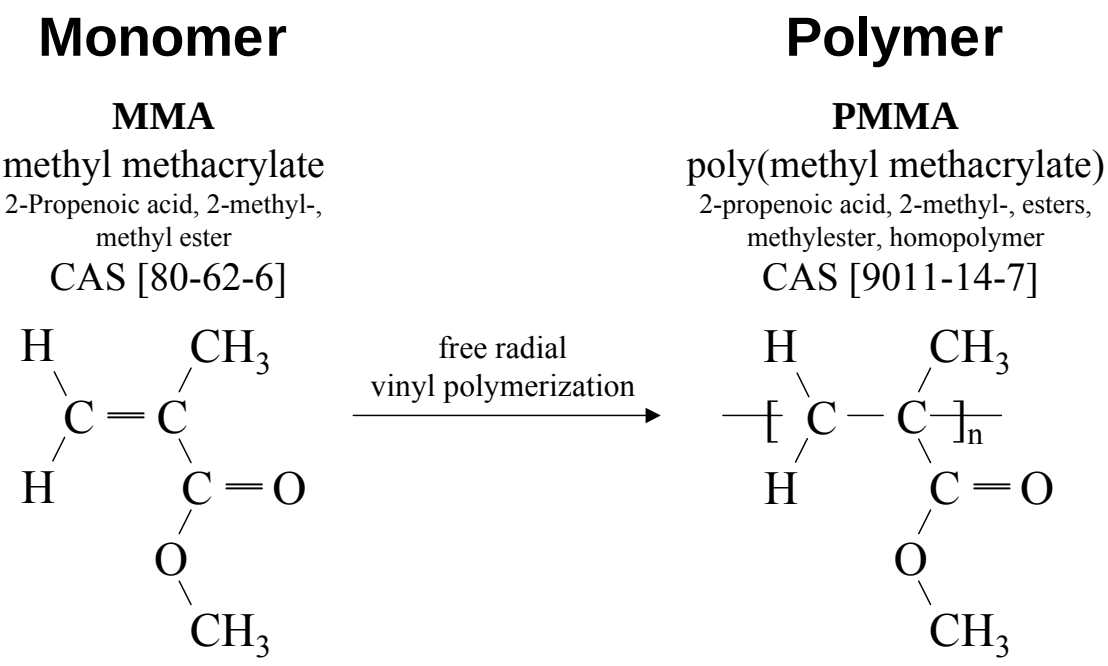

Figure 44 PMMA polymerization

PMMA is a member of a family of polymers which chemists call acrylates, or better known under the name acrylics. The general properties of PMMA are provided in Table 1.

Poly(methyl methacrylate)	
Type	Thermoplastics
Monomer:	Methyl methacrylate
Polymerization:	Free radical vinyl polymerization
Morphology:	Amorphous
Glass transition temperature:	105 °C

Table 4 poly(methyl methacrylate) at a glance

In general PMMA is a clear plastic, but is also available in an opaque form. When it is used as a clear plastic, it often replaces glass due to its shatterproof characteristics. When it comes to make windows, PMMA has even a further advantages

over glass, PMMA is more transparent than glass. When glass is made too thick, it becomes difficult to see through, but when PMMA is used even at a thickness of as much as 330 mm it is still perfectly transparent. Other areas of application of PMMA are paint e.g. acrylic "latex" paint, as an additive to lubricating oils and hydraulic fluids (increases their viscosity at low temperatures).

4.3.2. Properties of the PMMA Used in the Present Work (Acrylite FF from CYRO Industries)

The general properties of the material used for this study were provided by the manufacturer, PMMA (AcryliteFF) by CYRO Industries, and are displayed in Table 5 trough Table 9. As can be noted, from the tables below; only the density can be obtained as a function of temperature by means of the coefficient of linear thermal expansion. Further information especially temperature dependencies are generally not readily available from the producer.

Mechanical			
Property	ASTM Method	Value	Unit
Specific gravity	D 792	1.19	
Tensile Strength Elongation, Rupture Modulus of Elasticity	D 638	69 4.5 2800	M Pa % M Pa
Flexural Strength Modulus of Elasticity	D 790	117 3300	M Pa M PA
Impact Strenght Izod Milled Notch	D 256	21.6	J/m of notch
Rockwell Hardness	D 785	M-93	
Barcol Hardness	D 2583	48	

Table 5 mechanical properties for AcryliteFF from CYRO Industries

Optical			
Property	ASTM Method	Value	Unit
Refraction Index	D 542	1.49	
Light Transmission, Total	D 1003	0	%

Table 6 optical properties for AcryliteFF from CYRO Industries

Thermal			
Property	ASTM Method	Value	Unit
Forming Temperature		approx. 149	°C
Deflection Temperature Under load, 264 psi	D 648	91	°C
Vicat Softening Point	D 1525	105	°C
Maximum Recommended Continous Service Temperature		71	°C
Coefficient of Linear Thermal Expansion	D 696	0.000068	m/m - °C
Coefficient of Thermal Conductivity	Cenco-Fitch	0.19	W/m*K
Flammability, burning Rate (0.125" thickness)	D 635	25	mm/min
Self Ignition Temperature	D 1929	443	°C
Specific Heat @ 77°F		1470	J/kg*K
Smoke Density Rating	D 2843	5-10	%

Table 7 thermal properties for AcryliteFF from CYRO Industries

Electrical			
Property	ASTM Method	Value	Unit
Dielectric Strength Short Time (0.125" thickness)	D 149	17	kV/mm
Dielectric Constant 60 Hertz 1000 Hertz 1000000 Hertz	D 150	 3.6 3.3 2.8	
Dissipations Factor 60 Hertz 1000 Hertz 1000000 Hertz	D 150	 0.06 0.04 0.02	
Volume Resistivety	D 257	10^{16}	ohm-cm
Surface Resistivety	D 257	10^{15}	Ohms

Table 8 electrical properties for AcryliteFF from CYRO Industries

Miscellaneous			
Property	ASTM Method	Value	Unit
Water Absorptoin 24hr @ 73°C	D 570	0.2	
Odor		None	
Taste		None	

Table 9 miscellaneous properties for AcryliteFF from CYRO Industries

4.3.3. Molecular Weight

The evaluation of the molecular weight for polymers differs form that for small molecules because a polymer where all the chains have the same molecular weight does not exist. Usually a bulk piece of a specific polymer has a molecular weight distribution. In this bulk piece, some of the polymer chains will be much larger than others and some will be much smaller. The largest number will usually be clustered around a central point, the highest point on the curve Figure 45. The value given to the molecular weight of the polymer will therefore be an average value. The average can be calculated in a number of different ways that will be detailed as follows.

- **The Number Molecular Weight Average,** M_n - The number average molecular weight is the summation of the weight of each of the polymer molecules in a sample, divided by the total number of polymer molecules in the sample (Figure 45).

$$M_n = \frac{\sum_i n_i M_i}{\sum_i n_i} = \frac{W}{N} \tag{110}$$

where "i" is the polymer chain type, "n" the number of chains present, "M" the molecular weight of each individual chain, "W" the total weight and "N" the total number of chains.

- **The Weighted Molecular Weight Average,** M_w - The weighted average is based on the principle that a bigger molecule contains more of the total mass than a smaller one. Each molecular weight is multiplied by the molecular weight of the specific chain and the summation is divided by the summation of the total masses of each specific chain type (Figure 45).

$$M_W = \frac{\sum_i n_i M_i^2}{\sum_i n_i M_i} = \frac{\sum_i w_i M_i}{\sum_i w_i} \tag{111}$$

where w_i is the total weight of an individual type of chain.

- **The Viscosity Molecular Weight Average,** M_v **–** The molecular weight can also be calculated from the viscosity of a polymer solution. The bigger polymers molecules make a solution more viscous than small ones do. This measurement method is the so-called dilute solution viscometry.

$$M_v = \left[\frac{\sum_i n_i M_i^{1+a}}{\sum_i n_i M_i} \right]^{1/a} \tag{112}$$

where "a" is called the exponent of Mark-Houwink and represents the relationship that relates intrinsic viscosity to molecular mass [KreD-90].

As one would expect, the molecular weight obtained by measuring the viscosity is different from either the number average or the weight average molecular weight. Figure 45 illustrates the differences between all three methods where M_v tends to have an intermediate value between M_n and M_w.

None of the single methods can provide a full description of the polymer, therefore if the molecular weight is an issue of critical importance usually it is most adequate to plot the molecular weight distribution (Figure 45). In that plot, the molecular weight is plotted on the x-axis, and the amount of polymer at a given molecular weight is plotted on the y-axis. Generally the average molecular weight, the weighted molecular weight average, and the viscosity molecular weight average show up on the plot as depicted in Figure 45.

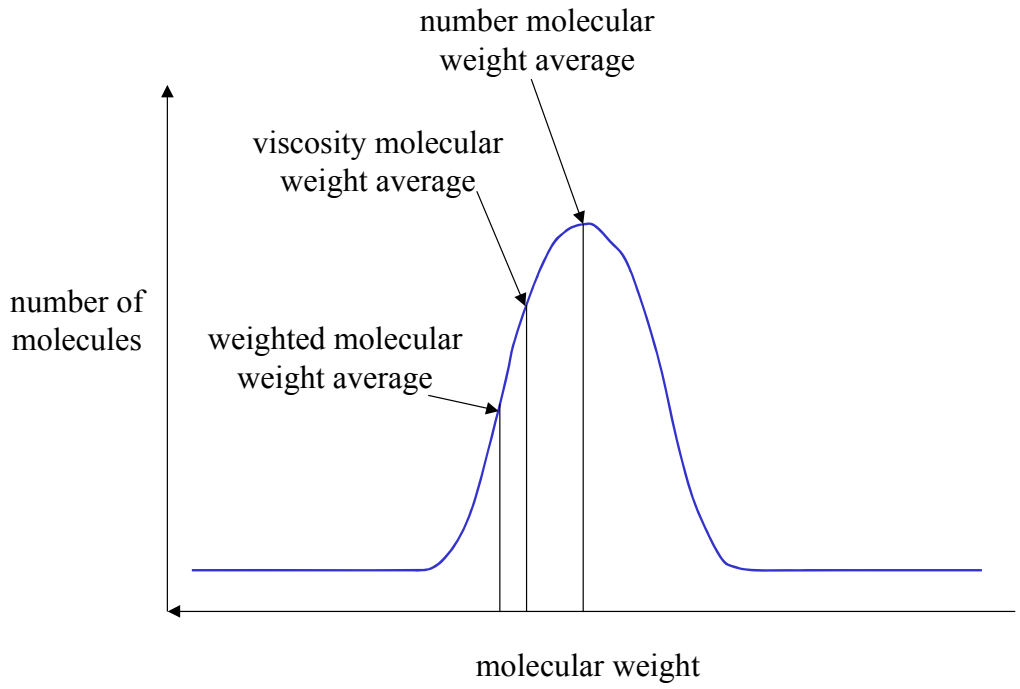

Figure 45 averaging the molecular weight

In an ideal scenario, the molecular weight will be evenly distributed as shown in Figure 45, but in most realistic polymers the distribution resembles more the curve presented in Figure 46. The uneven distribution of different size polymer chains makes, it often necessary to look in detail at the distribution when evaluating the effect of the molecular weight of the polymer on the different macroscopic mechanical and thermal properties of the material.

The unevenness in the molecular weight distribution can be a result of the so-called Tromsdorff effect, where the rate of polymerization steadily decreases as the viscosity of the gel increases, which can be found in free radical vinyl polymerization [BrIm-89].

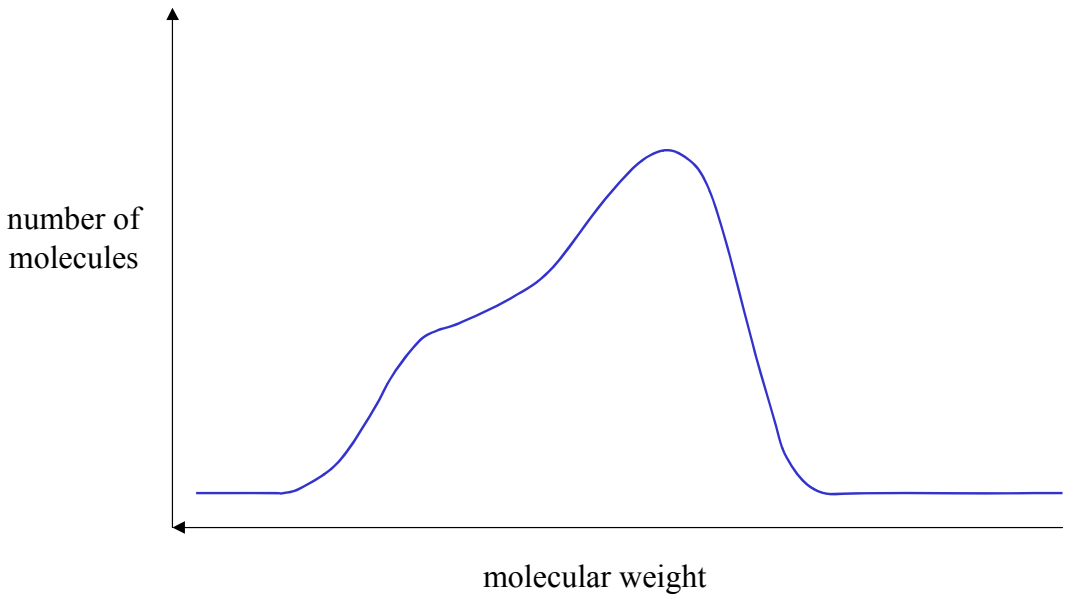

Figure 46 molecular weight distribution 1

Occasionally the distribution is even worse, like the one shown in Figure 47. As one can see in Figure 47 the number average molecular weight does not resemble the real situation because, there is not a single molecule of that weight in the whole sample.

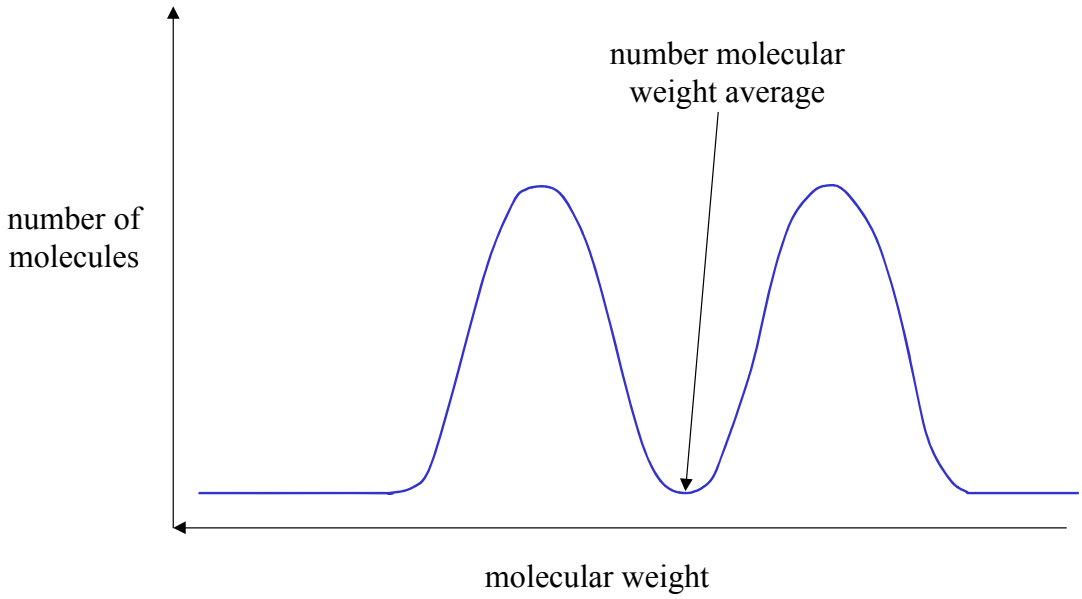

Figure 47 molecular weight distribution 2

The molecular weight distribution can be determined by of a size exclusion chromatography (SEC) or matrix-assisted laser desorption/ionization (MALDI) mass spectrometry. Details of how these techniques work go beyond the scope of this work but can be found in references [CreH-93].

Different properties have been found to depend more ore less significantly on the population of different chain sizes requiring for their determination accurate knowledge of the molecular mass distribution. Tensile and impact strength are governed by short molecules, viscosity and low shear melt flow by middle size molecules and melt elasticity by larger size chains. Thermodynamic properties are generally dependent only on the number average molecular mass and can be described by an equation of the type:

$$X = X_{\infty} - \frac{A}{M_n} \tag{113}$$

where X is the property considered, X_{∞} is the asymptotic value at very high molecular mass and A is a constant [KreD-90]. Therefore, for the purposes of this study the "Average Molecular Weight" will be considered sufficient for further calculations.

The average molecular weight provided by the manufacturer for AcryliteFF from CYRO is:

$$M_n = 93{,}200 \frac{g}{g\ mol}. \tag{114}$$

Typical values for the molecular weight for PMMA can be found in the literature, a few examples are shown in the table below:

Molecular weight (g/mol)	Reference
10,200	[KIBH-86]
17,400	[KIBH-86]
44,600	[KIBH-86]
176,000	[KIBH-86]
320,000	[KIBH-86]
54,800	[KIBH-86]
43,400	[KIBH-86]
12,900	[KIBH-86]
47,000	[KaOm-88]
200,000	[KaOm-88]
162,000	[RaLe-67] [LeRa-67] [LeRa-71]

Molecular weight (g/mol)	Reference
160,000	[BaWu-73]
60,600	[WuGa-81]

Table 10 molecular weight

The value of the molecular weight remains independent of temperature until the onset of decomposition (pyrolysis) therefore can be considered a constant throughout the preheating process.

4.4. Glass Transition

When a heated liquid polymer is cooled the free volume of the molecules decreases and the liquid contracts in an almost linear manner with temperature. The specific thermal expansivity for the liquid can thus be defined as:

$$\left(\frac{\partial V}{\partial T}\right)_p = e_1 \tag{115}$$

where V is the volume, T is the temperature, p is the pressure and e_1 specific thermal expansivity for the liquid.

When the liquid is cooled to a temperature below a potential crystalline melting temperature T_m, it can either crystallize or become an under-cooled liquid. If it crystallizes, further cooling will result in a constant temperature volume reduction (melt expansion ΔV_m) that if further cooled will lead to a volume reduction following an almost linear dependency with temperature.

$$\left(\frac{\partial V}{\partial T}\right)_p = e_g \tag{116}$$

If the liquid is under-cooled it will follow the relationship Equation (115) until a temperature is reached at which the free volume of the molecules becomes so small that molecular movements of the whole molecule or of large chain segments are no longer possible. This state is called the glassy state and the transition temperature, T_g, is the glass transition temperature [SiBo-62].

The glass transition is a phenomenon that only happens to those polymers, which are amorphous this is one of the things that makes them unique. At a certain temperature, which is different for each polymer, this transition will occur and major characteristic changes take place. When the polymer is cooled below this temperature, its characteristic changes from soft and flexible to hard and brittle, like glass. Polymers as we know them are used above and below their glass transition temperatures.

Plastics like polystyrene and poly(methyl methacrylate), which are used below their glass transition temperatures are hard ($T_g >> T_\infty$). The glass transition temperature for both these materials is around 100 °C. On the other hand elastomers like polyisoprene and polyisobutylene, are used above their glass transition temperatures, therefore they are soft and flexible.

Because the glass transition has a significant effect on the thermodynamical properties of polymers, it therefore will be addressed in more detail.

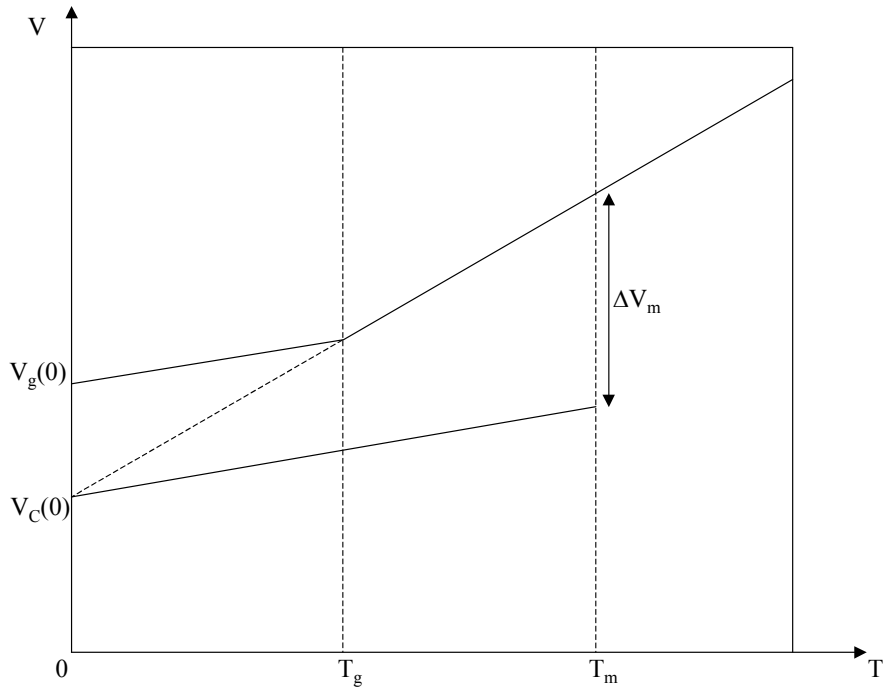

Figure 48 volume versus temperature

4.5. Heat Capacity and Latent Heat

When a crystalline polymer is heated at a constant rate, the temperature will increase at a constant rate. The same thing happens to the amorphous polymer. When the crystalline polymer has reached melting point, the temperature will hold steady for awhile, even though heat is further added to the polymer, until it is completely molten. At that point, the temperature of the polymer will begin to increase again, but at a slower rate, which means that the molten polymer has a higher heat capacity than the solid crystalline polymer, so it can absorb more heat with a smaller increase in

temperature. All this can be seen in Figure 49(a). If one summarizes the above given information, it can be said, that two things happen when a crystalline polymer melts:

1. It absorbs a certain amount of heat, the latent heat of melting and
2. it undergoes a change in it's heat capacity.

If we recall the heat capacity is the net amount of heat required to raise the temperature of one gram of material, in this case a polymer) one degree Celsius. Because the meting transition involves a change in heat capacity, and a latent heat, this transition is called first order transition.

When the amorphous polymer has reached the glass transition point, something different happens. The temperature does not stop rising, but the rising slope has changed as shown in Figure 49(b). The polymer undergoes an increase in its heat capacity when it undergoes the glass transition. Because the glass transition involves change in heat capacity, but it does not involve a latent heat, this transition is called second order transition.

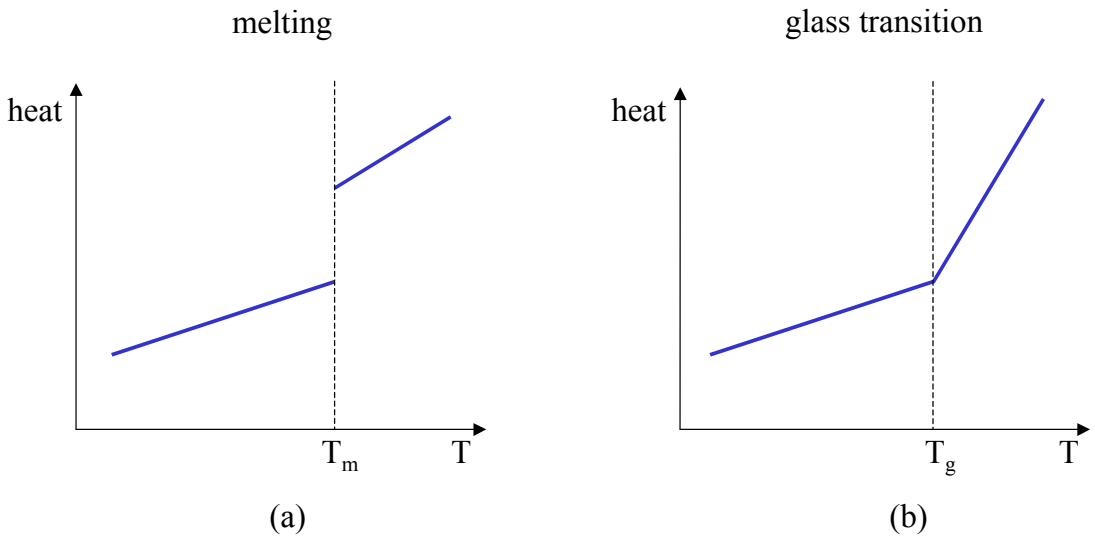

Figure 49 heat versus temperature for a (a) crystalline polymer (b) amorphous polymer

Measurements of the melting temperature, glass transition temperature, latent heats of melting and changes in heat capacity are generally obtained by differential scanning calorimetry, which will be described in Section 4.6.2.2.

In the present work, the only material that will be examined is poly(methyl methacrylate). As was mentioned at the beginning of this section the glass transition temperature of poly(methyl methacrylate) lies at around 100°C. In our case (for AcryliteFF from CYRO Industries), the glass transition lies, according to the manufacturer (see Table 7), at 105°C therefore determination of this value will not be part of this work.

4.6. Thermophysical properties of λ, ρ, c_p

As shown at the beginning of this chapter, the temperature evolution of the density ρ, the specific heat capacity c_p, and the thermal conductivity λ are necessary to determine the ignition delay time. These temperature evolutions are not provided by the manufacturer, therefore an exhaustive literature review will be used as a substitute to determine these properties. The following sections provide a summary of these data based on the principles explained above. The data collection in this chapter gathers, as far as possible, the information necessary, including which test method was used to obtain the data and a description of these test methods to assess their applicability to the present conditions.

4.6.1. Density ρ

The density ρ is one of those properties, which is going to be used in this work and need to be known in dependence of the temperature. In practice the determination of the temperature dependant density ρ is the easiest one, of the three temperature dependent properties, to get. One can just measure the weight and volume of a sample material, at different temperatures and will then obtain, a temperature dependent density $\rho(T)$. As mentioned before, it is known, that the density ρ decreases linearly with increasing temperature and that the slope is constant.

Agari [AUON-97] showed that even when blending PMMA with polycarbonate (PC) the slope of the temperature dependency of the density $\rho(T)$ does not change.

Therefore, the assumption was made that Agari's slope could be used for this work. Using that slope, and forcing it's value to be at room temperature (21°C) $1.19\left[\frac{g}{cm^3}\right]$, (which is the value provided by the manufacturer for AcryliteFF) the following expression is obtained for the temperature dependent density, where the temperature T has to be given in degree Celsius.

$$\rho = -7.316 \cdot 10^{-4} \cdot T + 1.4045 \left[\frac{g}{cm^3}\right] \tag{117}$$

The temperature dependant density, $\rho(T)$, for the PMMA used in this work over the temperature range 0 to about 280°C is presented in Figure 50.

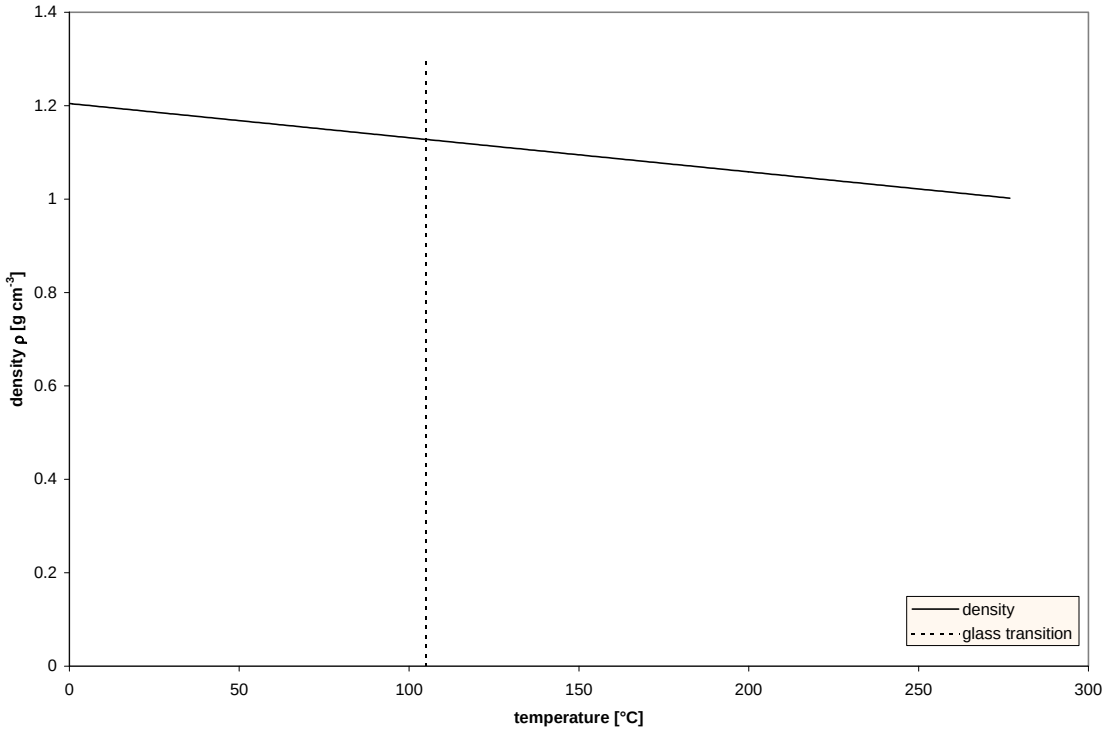

Figure 50 temperature dependant density (ρ) of the here used PMMA

4.6.2. Specific Heat Capacity, c_p

As it was mentioned earlier, some properties of the sample material, such as specific heat capacity c_p, need to be known as a function of the temperature. Therefore a literature research was conducted to obtain such data. A significant problem in the research was the determination of specific heat capacity c_p data in the required temperature range from 0 to about 275°C where pyrolysis of PMMA usually starts to occur.

One of the most interesting articles found in that research was the one from [GaWW-82] in which the heat capacity was reviewed for different polymers on the

basis of measurements on 35 different samples and an extensive literature survey. Some of the references cited in this work will be included here.

Table 11 provides a summary of the reviewed sample number, the characterization of the used PMMA, the investigator, the experimental technique, and the reference where to find that data in the literature.

Sample No.	Characterization	Investigator	Experimental technique	Reference
14g	Amorphous, solid	Sochava and Trapenzikova	Adiabatic (see Section 4.6.2.1)	[SoTr-58] [SocI-64] [SoTr-65]
16g	Amorphous, solid	O'Reilly and Karasz	Adiabatic (see Section 4.6.2.1)	[OJKB-64] [OJKF-66]
16m	Amorphous, molten	O'Reilly and Karasz	Adiabatic (see Section 4.6.2.1)	[OJKB-64] [OJKF-66]
18g	Amorphous, solid	Pavlinov et al.	Adiabatic (see Section 4.6.2.1)	[PROA-67]
18m	Amorphous, molten	Pavlinov et al.	Adiabatic (see Section 4.6.2.1)	[PROA-67]
20g	Amorphous, solid	Rabinovich and Lebedev	Adiabatic (see Section 4.6.2.1)	[RaLe-67] [LeRa-67] [LeRa-71]
22g	Amorphous, solid	Hoffmann and Knappe	Adiabatic (see Section 4.6.2.1)	[HoKn-71]
22m	Amorphous, molten	Hoffmann and Knappe	Adiabatic (see Section 4.6.2.1)	[HoKn-71]
25g	Amorphous, solid	Bares and Wunderlich	DSC (see Section 4.6.2.2)	[BaWu-73]
25m	Amorphous, molten	Bares and Wunderlich	DSC (see Section 4.6.2.2)	[BaWu-73]
26g	Amorphous, solid	Gaur and Wunderlich	DSC (see Section 4.6.2.2)	[WuGa-81]
26m	Amorphous, molten	Gaur and Wunderlich	DSC (see Section 4.6.2.2)	[WuGa-81]

Table 11 heat capacity of various solid and molten poly(methyl methacrylate)s

The evaluation, conducted by [GaWW-82], incorporated an assessment in terms of sample characterization, experimental technique used, error limits and accuracy, Table 11 only presents those measurement references, that fall in the 0 to 275°C (273.15 to 550K) temperature range.

Looking at that data, as presented in Figure 51 it is obvious, that even though a huge variety of different PMMA samples (different molecular weight, different color, etc.) were tested the band where they fall onto the heat capacity graph Figure 51 is relatively small. Easy to observe is the upward shift in the heat capacity at the glass transition temperature (105°C or 378.15K) as expected from the discussion in previous sections.

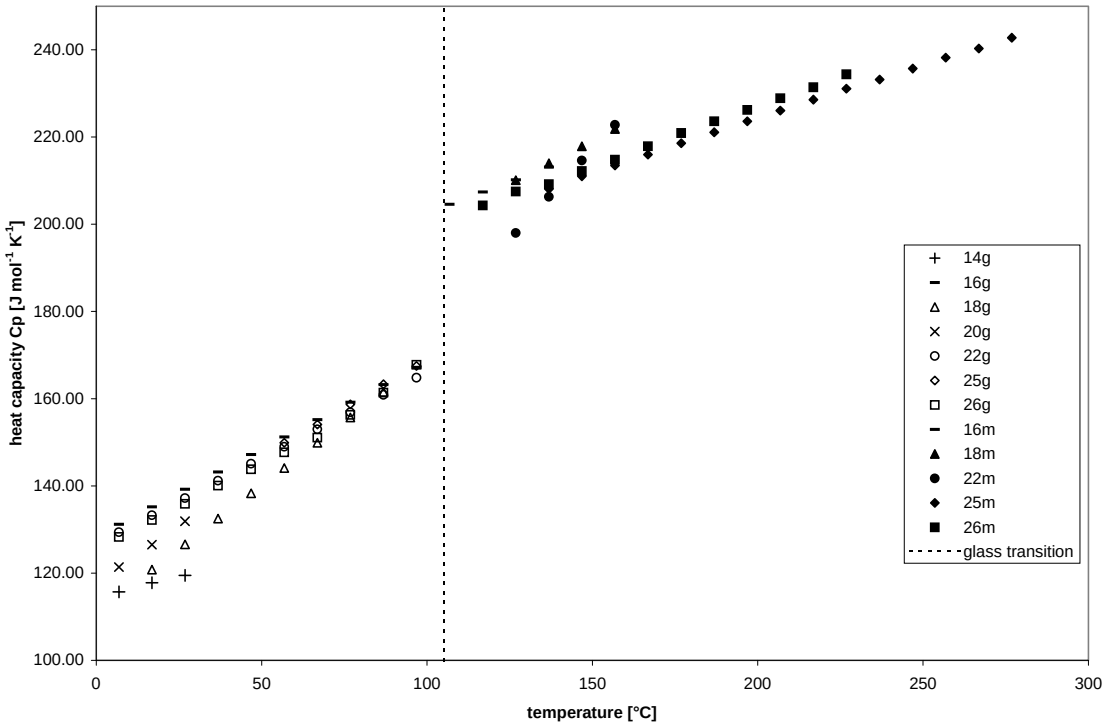

Figure 51 heat capacity of various solid and molten poly(methyl methacrylate)s

Due to the occurring small band, in which all the PMMA tests fall into, a function is created which will best fit the data in Figure 51. This fit was provided in the work of Gaur [GaWW-82]. The two curve fit functions, for the temperature range (273.15 to 550K) coming from that work are Equation (118) and (119). Where Equation (118) is valid in the temperature rage from 150 to 370K and Equation (119) is valid for the temperature range from 380K to 550K. The temperature in Equation (118) and (119) is given in Kelvin. As a reminder, the glass transition temperature for the here used PMMA is 105°C or 378K.

$$C_p = 1.902 \cdot 10^4 \cdot T^{-2} + 0.405 \cdot T + 16.118 \left[\frac{J}{mol\,K} \right] \tag{118}$$

$$C_p = 0.237 \cdot T + 112.95 \left[\frac{J}{mol\,K} \right] \tag{119}$$

Figure 52 shows the evolution of c_p as predicted by Equations (118) and (119). The plot also includes the experimental data of Figure 51. One can see, that those two function resemble the heat capacity c_p of a variety of different PMMA's.

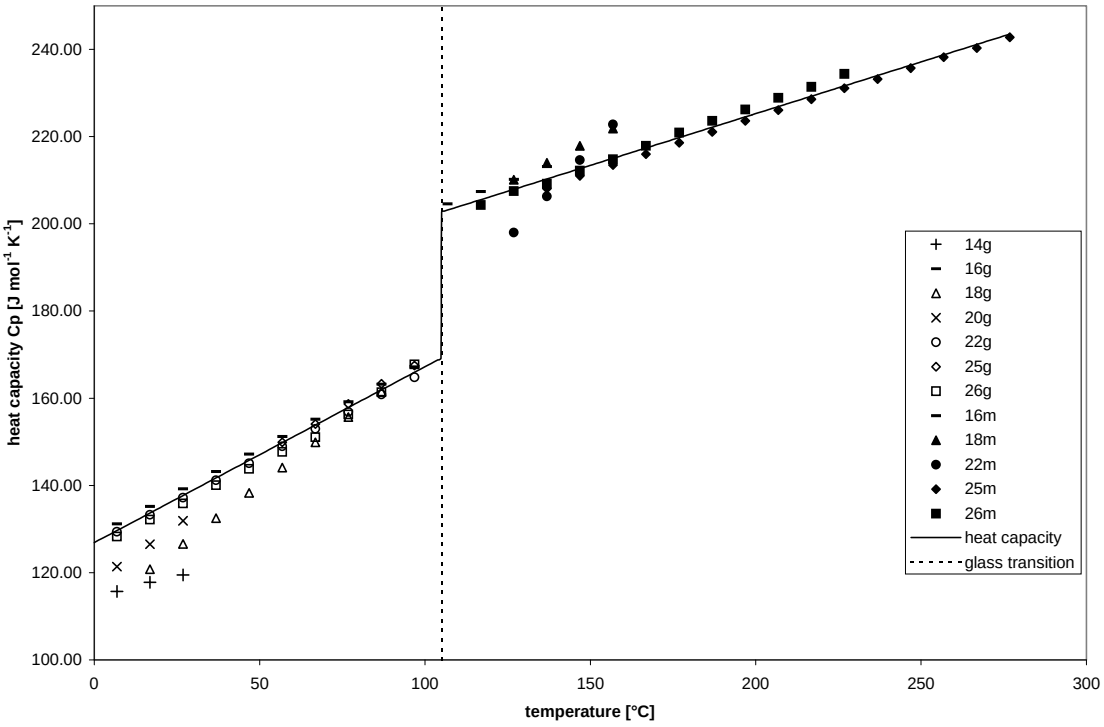

Figure 52 curve fit through the heat capacity of various solid and molten poly(methyl methacrylate)s

Looking at Figure 52, the chosen function for the case up to the glass transition point in the solid state does not appear to resemble the presented data very well. Some discrepancy of the data is observed in the lower temperature range so the line was chosen to fit the data that was most consistent with the information available at temperatures close to ambient and in the temperature range from 150K to 370K. Equations (118) and (119) will, thus, be used in the further analysis.

For later use, the specific heat capacity for PMMA per unit mol C_p as represented through the two Equations (118) and (119) and the graph in Figure 53 is going to be transformed by means of Equation (120) into the specific heat capacity c_p per unit mass.

$$c_p = \frac{C_p}{M_n} \tag{120}$$

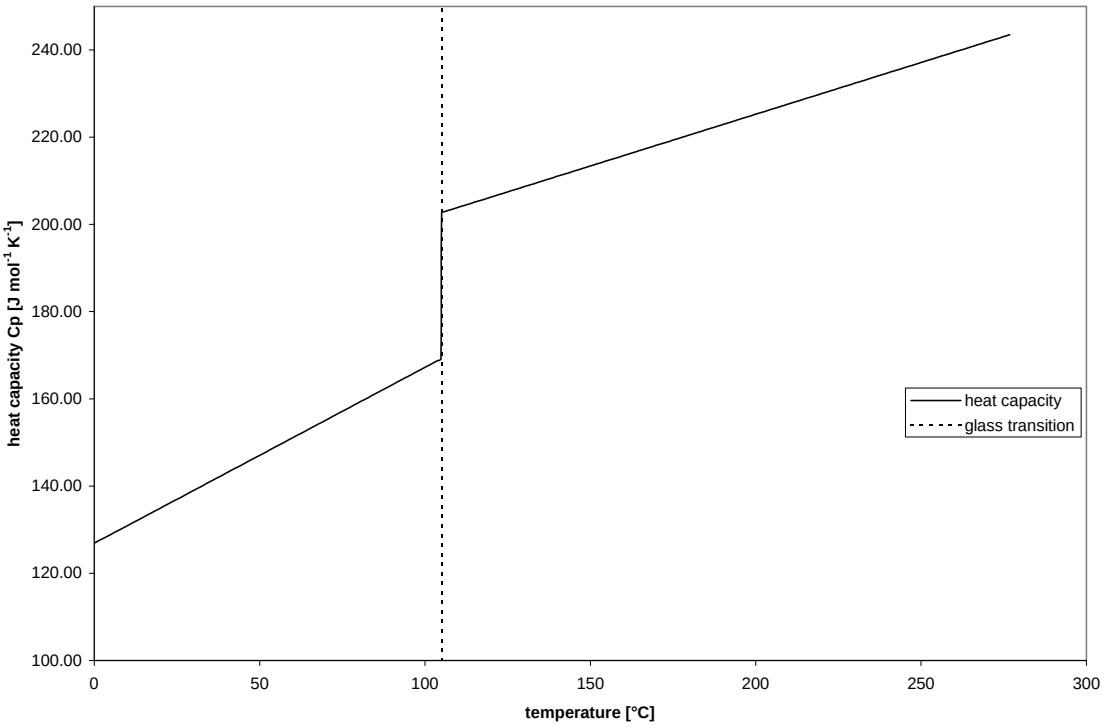

Figure 53 heat capacity graph of Equation (118) and (119)

The molecular weight used for that transformation is the number molecular weight, received from the manufacturer of the used PMMA (AcryliteFF from CYRO Industries), which one can get from Equation (114). This transformation has the effect that Equation (118) and (119) had to be rewritten and are presented by Equation (121) and (122).

$$c_p = 2.041 \cdot 10^2 \cdot T^{-2} + 4.341 \cdot 10^{-3} \cdot T + 0.173 \left[\frac{J}{g\,K} \right] \tag{121}$$

$$c_p = 2.547 \cdot 10^{-3} \cdot T + 1.212 \left[\frac{J}{g\,K} \right] \tag{122}$$

The result of that transformation is presented in Figure 52.

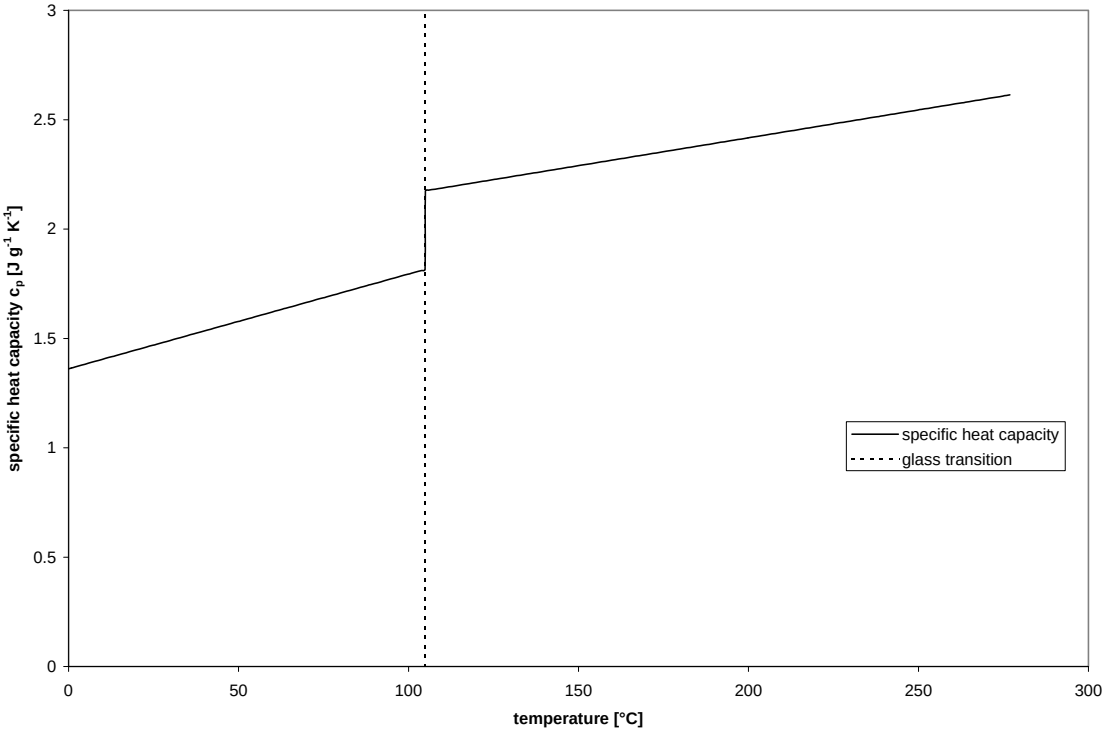

Figure 54 specific heat capacity graph of Equation (121) and (122)

The two test methods listed in Table 11 (adiabatic calorimetry and differential scanning method(DSC)) are also those, which are usually used for the determination of the heat capacity of polymers over a wide temperature range. For a better understanding those two test methods are described in Section 4.6.2.1 and 4.6.2.2.

4.6.2.1. Adiabatic Calorimetry

Precision measurements of the heat capacity over a large temperature range are usually done in adiabatic calorimeters. The adiabatic calorimetry is a technique, which

has lately become of rare use. Therefore only a few laboratories are equipped with such a testing device. A typical adiabatic colorimeter to measure the specific heat capacity c_p consists of an electrical heating source and a temperature measuring device. The first supplies an exact amount of heat, which goes into the sample; the later determines the change in temperature of the sample. The heat leakage is kept to a minimum, by carefully shielding the calorimeter from radiation losses. The remaining heat losses are going to be corrected so that it is possible to get the actual energy input to the sample.

With these information it is now possible to calculate an average heat capacity for the heating interval for the sample with Equation (123).

$$\bar{c}_p = \frac{\Delta Q}{m\,\Delta T}\left[\frac{J}{g\,K}\right] \tag{123}$$

In Equation (123) m is the mass, $\bar{c}_p$ the mean specific heat capacity for the given temperature rise ΔT, and ΔT the corrected energy input. The typical overall precessions, which one gets with such an apparatus is 0.1-0.5%. Even tough the adiabatic calorimetry is one of the most precise method for a direct measurement of the heat capacity it has some disadvantages. Those disadvantages are:

1. It is a time consuming test method
2. Each instrument is as a rule custom build, and therefore time and money consuming.

3. For polymers, due to their metastability and sensitivity to thermal pretreatment, it is not a preferable test method.

4.6.2.2. Differential Scanning Calorimetry (DSC)

The Differential Scanning Calorimetry (DSC) is probably the most widely used of all the thermal analysis techniques and is capable of measuring the heat flow as a function of time. The heat flow can than be used to determine the specific heats, glass transition temperatures, melting points, percent crystalinity, degree of cure, purity, effectiveness of plasticizers, thermal history and effects of additives and fillers.

The Differential Scanning Calorimetry (DSC) system consists of two pans. One pan contains the substance, which has to be measured, and the second pan is held empty as a reference. Currently two types of DSC's are commercially available:

1. The power compensated DSC and
2. the heat flux DSC, which is also known as Differential Thermal Analysis (DTA).

In the power compensated DSC case, the two pans are heated separately in such a way that they achieve the same temperature simultaneously. Each pan has its own furnace and fluctuations are compensated for in the individual pan. In the heat flux DSC, or DTA, the sample and reference are heated by the same furnace and the difference in temperature between the sample and reference is measured.

Commonly the power compensated DSC is used that is why this type is going to be described below in more detail. The temperature of the sample of the power compensated DSC is constantly rising, at a given rate. The result of that type of DSC is a plot where the difference in heat output, of the two heaters, is plotted against the temperature. Many of the important informational points, like the glass transition T_g, the melt point T_m, heats of crystallization H_c, melting H_f, and ultimate decomposition T_d, are already provided by a simple heating experiment, while additional information can be obtained from a controlled cooling and subsequent sample reheating process.

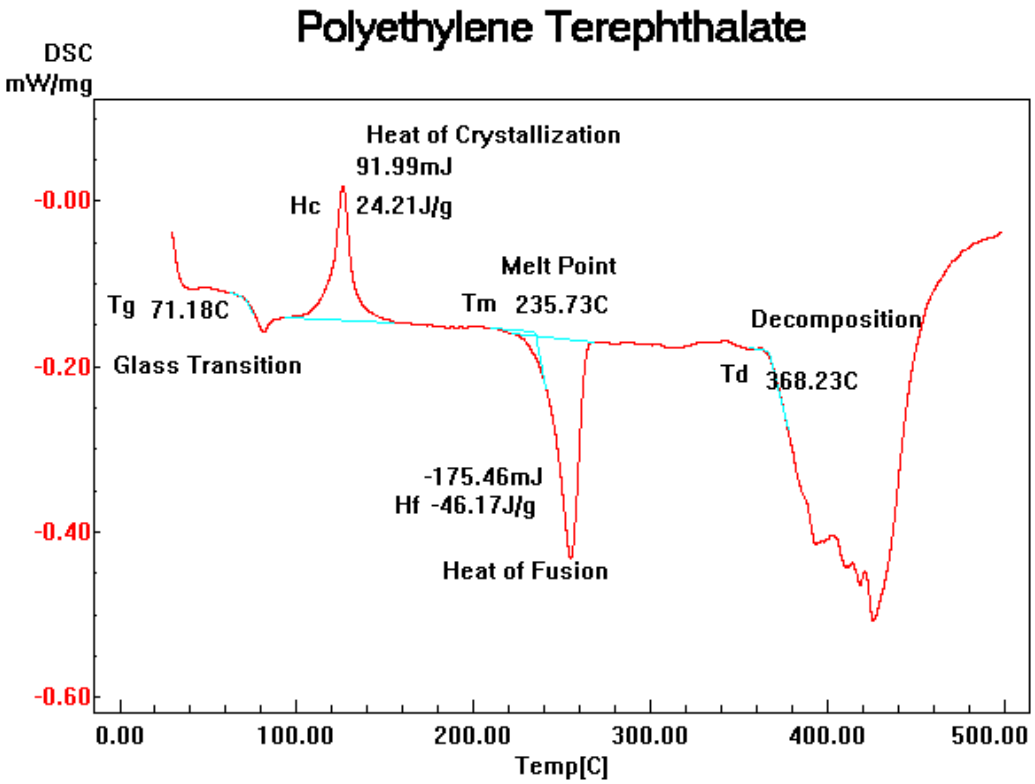

Figure 55 example DSC thermograph for Polyethylene Terephthalate (PET) from T_g Technologies, Inc

To calculate the **heat capacity** the heat absorbed by the polymer has to be plotted against the temperature. To see how such a plot will looks like at first one should look at Figure 56.

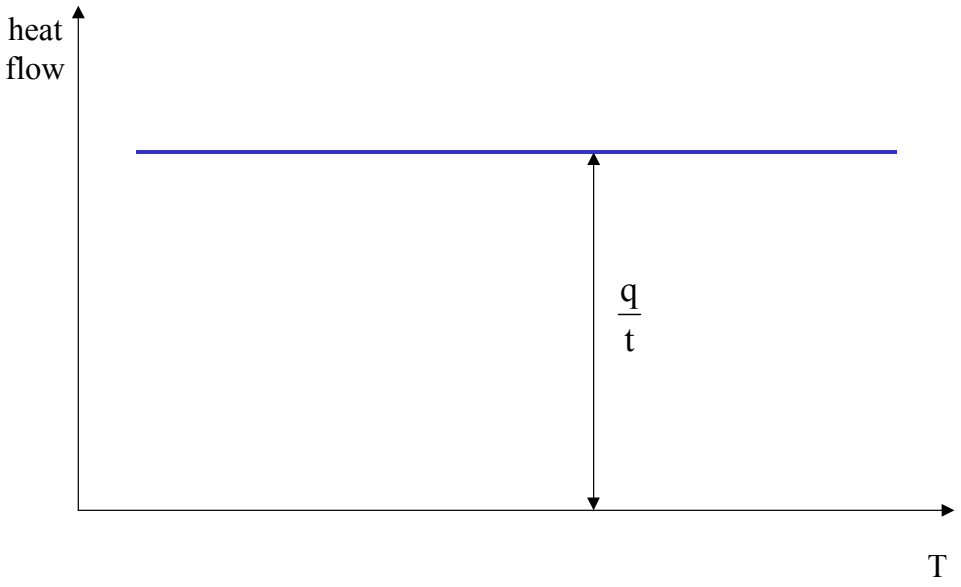

Figure 56 heat absorbed by the polymer plotted against the temperature

The heat flow at a given temperature is going to be shown in units of heat, q supplied per unit time, t

$$\frac{\text{heat}}{\text{time}} = \frac{\text{q}}{\text{t}} = \text{heat flow} \tag{124}$$

and the heating rate is temperature increase ΔT per unit time, t

$$\frac{\text{temperature increase}}{\text{time}} = \frac{\Delta\text{T}}{\text{t}} = \text{heating rate}. \tag{125}$$

The quotient of the heat flow $\frac{q}{t}$ divided by the heating rate $\frac{\Delta T}{t}$ is the heat capacity or when the starting equation is simplified the supplied heat divided by the temperature increase. The so received heat capacity has a typical precision of 1-3%.

$$\frac{\frac{q}{t}}{\frac{\Delta T}{t}} = \frac{q}{\Delta T} = \frac{\text{heat}}{\text{temperature increase}} = C_p = \text{heat capacity} \qquad (126)$$

Trying to determine the **Glass Transition Temperature** one has to look at the plot heat absorbed by the polymer versus temperature especially at the suddenly occurring upward shift, as shown in Figure 57, which occurs when the polymer is slightly beyond the glass transition temperature.

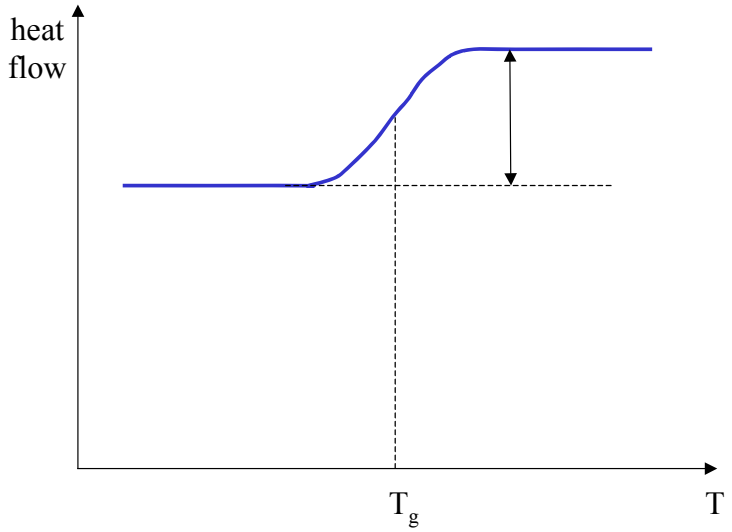

Figure 57 glass transition: heat absorbed by the polymer plotted against the temperature

Figure 57 clearly depicts that the pan with the polymer needs more heat (meaning, that a higher heat flow goes towards the sample polymer) to keep both pans at the same temperature. This fact also means that an increase of the polymers heat capacity occurred, because the polymer has just gone through the glass transition from

hard and brittle ton soft and flexible. Due to this change in heat capacity that occurs at the glass transition it is now possible to that the polymer's glass transition temperature is measured with the DCS.

Another phenomenon which can be detected with the DSC is the **Crystallization** of a polymer. It can be said, that polymers have a lot of mobility above the glass transition point. When reaching the right temperature, they will have gained enough energy to move into very ordered arrangements, which we call crystals. When this happens and polymers fall into these crystalline arrangements, they give off heat. This phenomenon can be seen in Figure 58 as big dip in the plot of heat flow versus temperature.

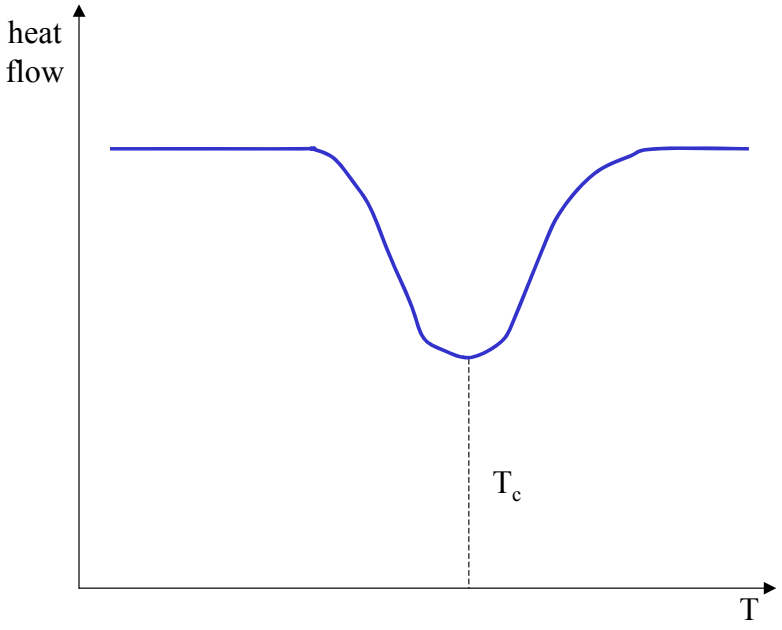

Figure 58 crystallization: heat absorbed by the polymer plotted against the temperature

The observed dip occurs due to a small amount of heat which is needed from the outside to keep the temperature of the sample rising. From a plot such as shown in Figure 58, the crystallization temperature T_c, the latent energy of crystallization for the polymer (by measuring the area of the dip), and that the polymer can in fact crystallizes can be determined. It is obvious such a dip would not occur if the tested polymer is 100% amorphous. Because the polymer gives off heat when it crystallizes, the crystallization process is an exothermic transition.

For those polymers, where **melting** occurs the DSC can be used to determine melting temperature T_m. When the heating process is still running, after the polymer past its crystallization temperature T_c another thermal transition, which is called melting, takes place. We the crystalline polymer's melting temperature T_m is reached, the crystalline polymer crystals begin to fall apart, which is called melting. When the polymer crystals melt, they must absorb heat. This means that when the melting temperature is reached, the polymer's temperature will not rise until all the crystals have melted. For the DSC that means, that the heater under the sample to output a lot of heat in order to melt the crystals and keep the temperature rising at the same rate as that of the reference pan. The extra heat flow during melting is then distinctly seen as a big peak the DSC plot as shown in Figure 59.

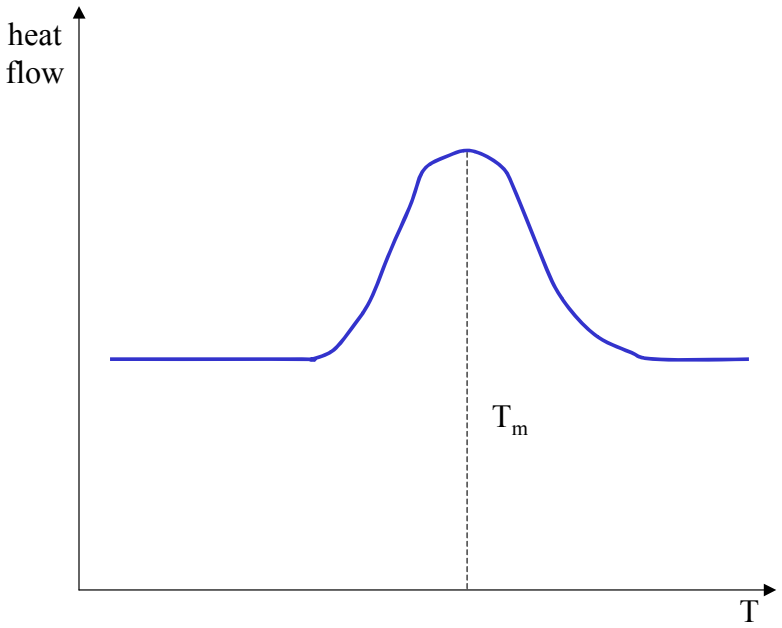

Figure 59 melting: heat absorbed by the polymer plotted against the temperature

An additional piece of information can be received from the above shown plot and its peak. The latent heat of melting can be found my measuring the area of this peak. Because the energy has to be added to the polymer to make it melt, this transition is an endothermic one.

When the glass transition is included together with the crystallization, and the melting in one single plot, the result is similar to the plot presented in Figure 60.

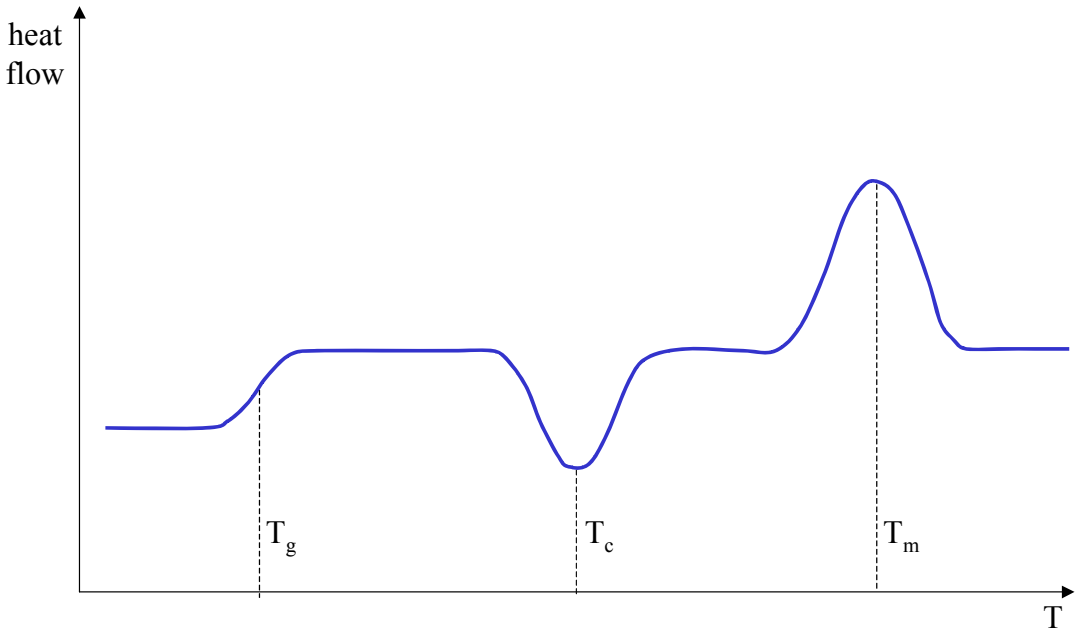

Figure 60 glass transition, crystallization and melting combined: heat absorbed by the polymer plotted against the temperature

Looking at Figure 60 it has to be clear, that not every transition will be on every DSC plot. The crystallization dip and the melting peak will only show up for polymers that can form crystals. Completely amorphous polymers will not show any crystallization, or any melting. But polymers with both crystalline and amorphous domains, will show all the features presented above.

4.6.3. Thermal Conductivity λ

The temperature dependency of the thermal conductivity λ is the last of the three properties, which is necessary, for this work. The thermal conductivity of amorphous thermoplastics was studied to quite an extent from low temperatures up to the glass transition point. The significant problem when determining this property beyond the glass transition point and up to 275°C because, almost no data exists of values for the

thermal conductivity of neither molten polymers nor PMMA. The probable reason for that is that most tests were conducted with a two-plate-apparatus which will be described later (Figure 65) and was designed for solid objects. Therefore the thermal conductivity of a probe can only be measured up to the temperature, where the probe is going to start to flow under its own mass. The temperature where that is going to happen for PMMA is the glass transition temperature of 105°C. Another experimental problem is, that at higher temperatures, due to a break down process, gasses are released which cause the PMMA to form gas bubbles.

Due to the above described reasons, most of the thermal conductivity data, for different kinds of PMMA, could be found for a temperature range below 105°C, while the literature search for the data above 105°C was not too successful. Never the less, some data was found, which covers the temperature range between 0°C and 250°C (which is the field of interest). The collected data for the thermal conductivity from different authors, measurement techniques, and PMMA's is presented in Figure 61. Table 12 serves for the same figure (Figure 61) as an information board which lists the sample number, the characterization of the used PMMA, the investigator, the experimental technique, and the reference where to find that data in the literature.

Sample No.	Characterization	Investigator	Experimental technique	Reference
1	Solid	Eiermann	N/A (probably two-plate apparatus)	[EieK-61]
2	Amorphous solid & molten	Eiermann	Cylindrical apparatus	[EieK-65]
3	Amorphous, solid	Eiermann	N/A (probably two-	[EieK-64a]

Sample No.	Characterization	Investigator	Experimental technique	Reference
			plate apparatus)	
4	Amorphous, solid	Eiermann	N/A (probably two-plate apparatus)	[EieK-64b]
5	Amorphous, solid	Hellwege Hennig Knappe	N/A (probably two-plate apparatus)	[HeHK-63]
6	Amorphous, solid	Knappe	Two-plate apparatus without a hot guard	[KnaW-60]
7	Amorphous molten	Lohe	Cylindrical apparatus	[LohP-65]
8	Amorphous solid & molten	Shoulberg Shetter	guarded hot-plate	[ShSh-62]

Table 12 thermal conductivity of various solid and molten poly(methyl methacrylate)s

In addition to the collected data the glass transition temperature of the PMMA used for this work is also depicted in Figure 61. Naturally this transition temperature does not always match the glass transition temperature of all the depicted PMMA's. But due to the small difference it is still presented and becomes later important, when attempting to establish an equation for $\lambda(T)$ valid for the region above and below the glass transition. Figure 62 is a simple close up of Figure 61 to allow better observation of the different data found in the literature.

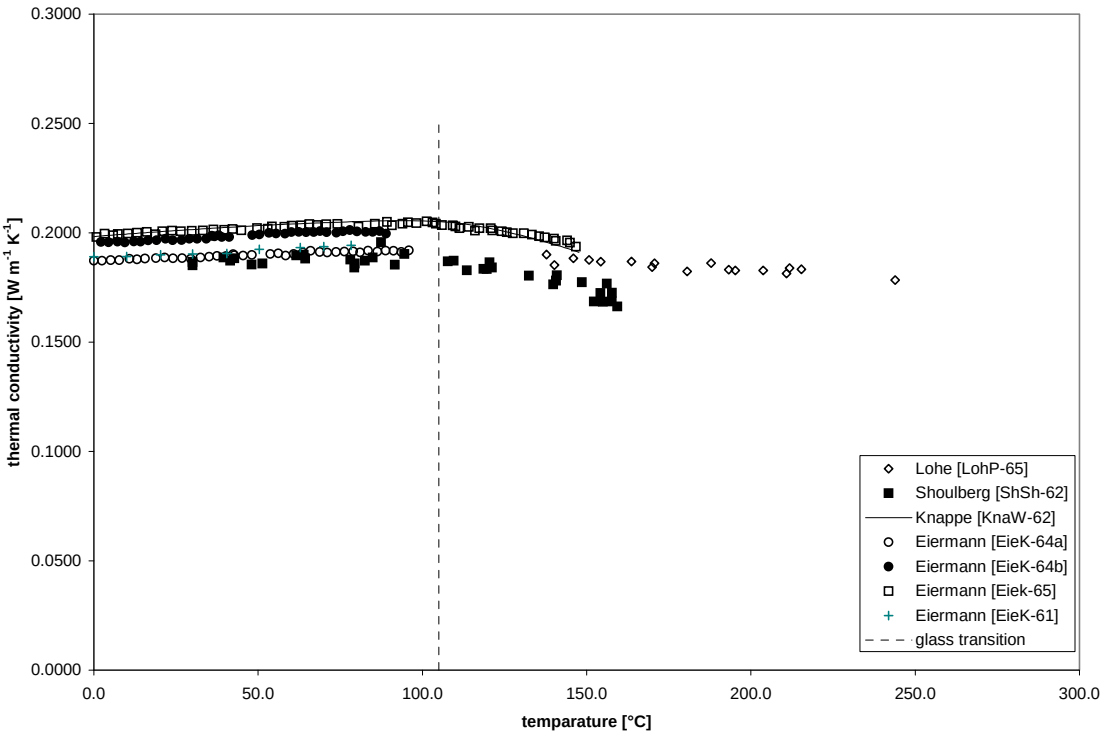

Figure 61 thermal conductivity of various solid and molten poly(methyl methacrylate)s

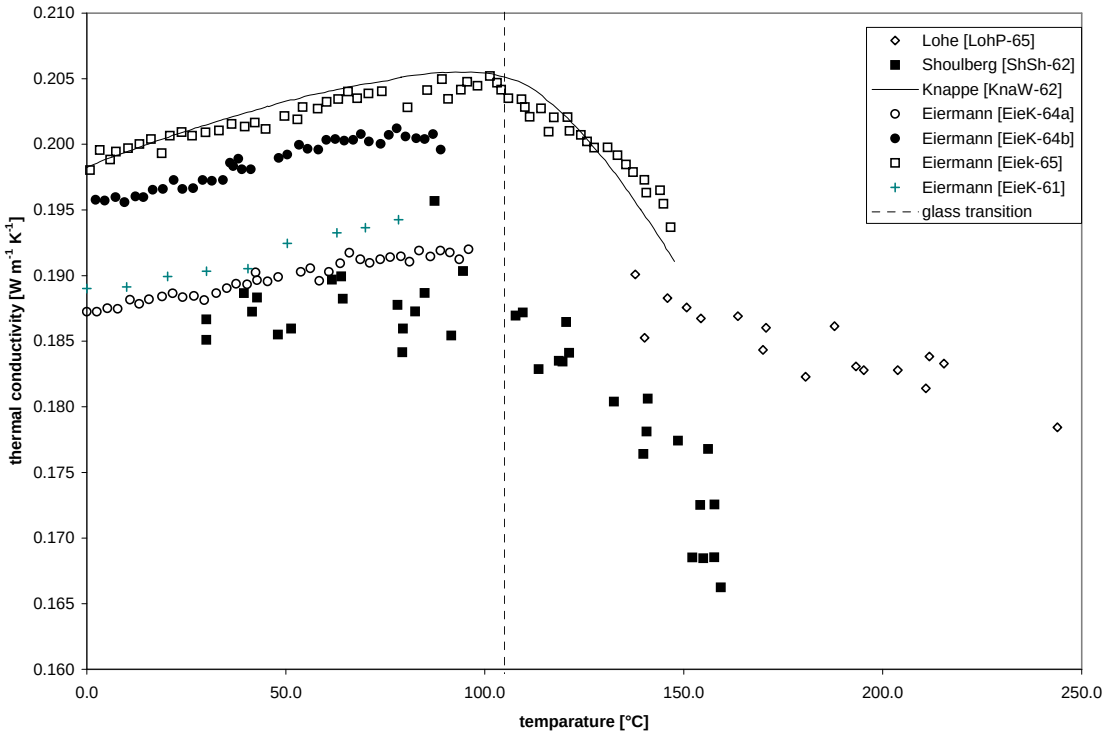

Figure 62 close up thermal conductivity of various solid and molten poly(methyl methacrylate)s

The data presented in Figure 61 shows that, the data, although obtained for different kinds of PMMA's and by means of different measurement techniques, is fairly consistent. Due to this fact and the theory, which says that the region above and below the glass transition point can be described with two straight lines with different slopes [EieK-64a, KnaW-71], a least square best fit line at each side of the glass transition point was chosen to represent the variation of the thermal conductivity with temperature Figure 63.

The mathematical regression process of the "Least Squares Fitting" was chosen, due to the fact, that a best fitting curve from a given set of data points can be

determined. This task is achieved, by minimizing the sum of the squares of the offsets of the data points from the curve. The sum of the squares of the offsets is used instead of the offset absolute values because this allows the residuals to be treated as a continuous differentiable quantity.

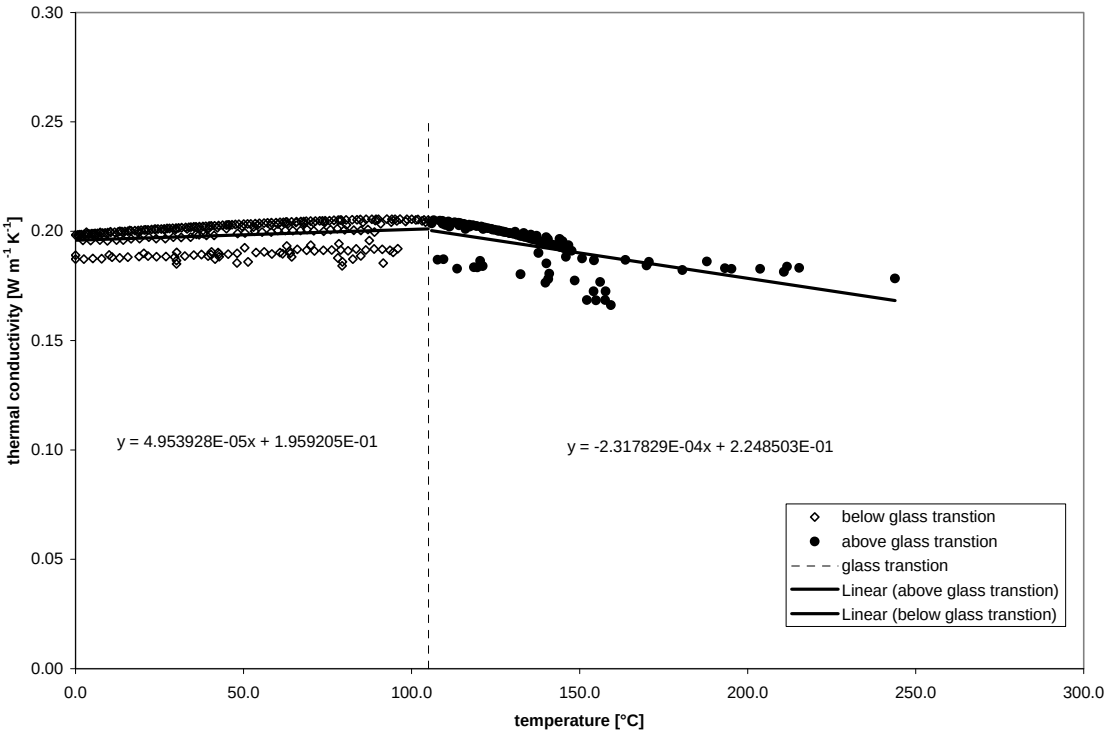

Figure 63 line fit through the heat capacity of various glassy and molten poly(methyl methacrylate)s

The obtained curves for the thermal conductivity as a function of time for the area below the glass transition temperature are presented in Equation (127), while the area above the glass transition temperature is expressed in Equation (128), where T is in degree Celsius.

$$\lambda = 4.954 \cdot 10^{-5} \cdot T + 1.959 \cdot 10^{-1} \left[\frac{W}{m\,°C} \right] \tag{127}$$

$$\lambda = -2.318 \cdot 10^{-3} \cdot T + 2.249 \cdot 10^{-1} \left[\frac{W}{m\,°C} \right] \tag{128}$$

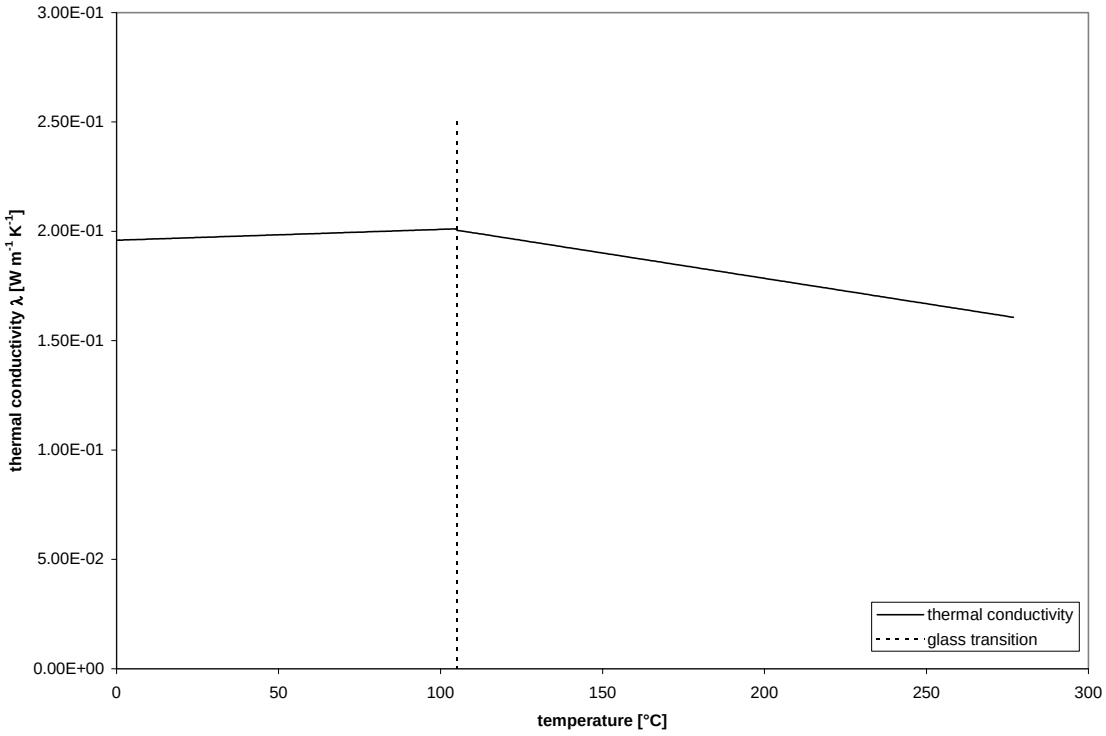

Figure 64 specific heat capacity graph of Equation and (127) and (128)

In Figure 64, the thermal conductivity λ obtained from Equation (127) and (128) are presented to show, how the positive slope changes to a negative one, when increasing the temperature of PMMA over the glass transition temperature.

This jump in the slope of the thermal conductivity can be explained by the following a simplified solution. The thermal expansion of amorphous high polymers

below the glass transition temperature is small compared to the one above. This leads to a different change in the elasticity constant of the atomic bindings with temperature above and below the glass transition temperature, and therefore, a change in the slope of the thermal conductivity.

Subtracting the slope of Equation (127) from the slope of Equation (128) a discontinuous increase of $2.81 \cdot 10^{-4} \left[°C^{-1} \right]$ is obtained. This sudden change is too small, when compared to experimental and theoretical values obtained from the literature [EieK-64a, KnaW-71]. Eiermann [EieK-64c] developed in his dissertation a model for the heat transport of amorphous materials to explain the observed thermal conductivity effects of amorphous plastics. According to his model, each binding between neighboring atoms has a heat resistance which he calls "Elementary Heat Resistance". The total heat resistance of a macroscopic amorphous probe consists of a network of elementary heat resistances, where the atoms resemble the junctions. The elementary heat resistance decreases with a growing elasticity constant of the binding force, which depends on the atom distances, therefore the thermal conductivity and density are interlinked. Following Eiermann [EieK-64c], the following equation is derived:

$$\frac{\Delta\left(\frac{1}{\lambda}\frac{d\lambda}{dT}\right)}{\Delta\alpha} = -5{,}8 \tag{129}$$

Where $\Delta\left(\frac{1}{\lambda}\frac{d\lambda}{dT}\right)$ is the jump in the temperature coefficient of the thermal conductivity λ and $\Delta\alpha$ the jump in thermal expansivity. Due to the fact, that for amorphous high polymers which glass transition temperature T_g is in the order of the room temperature (e.g. PMMA) the jump in thermal expansivity $\Delta\alpha$ is found to be $3\cdot10^{-4}\left[\frac{1}{°C}\right]$. According to Equation (129) the jump in the temperature coefficient of the thermal conductivity λ will then be $1.74\cdot10^{-3}\left[\frac{1}{°C}\right]$. Shima and Boyer [SiBo-62] show that the jump in thermal expansivity $\Delta\alpha$ is inversely proportional to the glass transition temperature T_g leading to the following equation

$$\Delta\left(\frac{1}{\lambda}\frac{d\lambda}{dT}\right)=1.72\cdot10^{-3}\frac{293}{T_g}=\frac{0.51}{T_g}, \tag{130}$$

Where the glass transition temperature T_g is in Kelvin, which would determine, for the here used PMMA, a value of

$$\Delta\left(\frac{1}{\lambda}\frac{d\lambda}{dT}\right)=1.35\cdot10^{-3}\left[\frac{1}{°C}\right] \tag{131}$$

for a glass transition temperature of 105°C. Measured values from range from between $1\cdot10^{-3}\left[\frac{1}{°C}\right]$ to $2\cdot10^{-3}\left[\frac{1}{°C}\right]$ [EieK-64, ShSh-62]. The variance of the theoretical and

experimental results is probably due to the usage of different measurement techniques (more and less sophisticated) and the small amount of data available for the higher temperature region. For an exact determination, the sample would have to be measured with one of the techniques described below to determine the thermal conductivity over a larger temperature range exceeding the glass transition point.

Having found, as described above, an approximate value for the thermal conductivity λ of PMMA as a function of temperature, the rest of this section will deal with the description of different measurement techniques can be used to achieve these data points. The literature review was extensive and not all of the studies were relevant to this work, therefore, only those pertinent will be referred here. Further information and references can be obtained from the references within these studies.

In general it can be said, that the experimental techniques to measure the thermal conductivity can be divided into three different groups. Those groups are the

- Steady State (section 4.6.3.1)
- Quasi Steady State and (section 4.6.3.2)
- Unsteady State (section 4.6.3.3).

All these methods are based on the Fourier differential equation for heat conduction (Equation (132)).

$$c_p \rho \frac{\partial T}{\partial t} = \lambda \left(\frac{\partial^2 T}{\partial x^2} + \frac{\partial^2 T}{\partial y^2} + \frac{\partial^2 T}{\partial z^2} \right) + \dot{q}_i \tag{132}$$

Where c_p is the heat capacity, T is the temperature, ρ is the density, t is the time, and x, y, and z are the Cartesian coordinate directions. The heat source term $\dot{q}_i$ in that equation is for most cases zero. Therefore Equation (132) can be rewritten to Equation (133).

$$c_p \rho \frac{\partial T}{\partial t} = \lambda \left(\frac{\partial^2 T}{\partial x^2} + \frac{\partial^2 T}{\partial y^2} + \frac{\partial^2 T}{\partial z^2} \right) \tag{133}$$

Looking at Equation (133) it can be seen, that an infinite number of solutions exist to determine the thermal conductivity λ. Because of that, a large number of measurement techniques exist to measure the thermal conductivity λ or the thermal diffusivity α , which are both related to each other by the following equation.

$$\alpha = \frac{\lambda}{\rho c_p} \tag{134}$$

With this information the three different thermal conductivity measurement technique groups can be approached.

4.6.3.1. Steady State Technique

The steady state group of the experimental techniques to measure the thermal conductivity λ is based on the steady state principle. That basically means, that the

temperature distribution in the examined sample does not depend on time. Assuming a one-dimensional heat flux and a simple geometric shape of the tested sample Equation (133) can be transformed into Equation (135), as described in [CaJa-76] and [LykA-67].

$$\lambda = \frac{\dot{Q}\, d}{\Delta T\, A} \tag{135}$$

Where $\dot{Q}$ (W) is the time rated heat flow, d (m) is the sample thickness, ΔT (K) is the temperature gradient and A (m^2) is the surface area. The thermal conductivity λ is assumed to be independent of temperature, which can only be assumed, for small temperature gradients. Therefore it is necessary to insure, that the measurements are conducted with small temperature gradients in order to justify that assumption and calculation.

The most widely used steady state thermal conductivity experimental techniques are the guarded hot plate and cylindrical method. The guarded hot plate has the reputation, to be the most accurate for measurement technique of the thermal conductivity for low thermal conductivity materials. The disadvantage of this method is that they require a long time until measurements can be taken, and that the temperature regulation of the guard is fairly complex. Due to this fact here the described apparatus is the two-plate-apparatus without a hot guard which one can see in Figure 65.

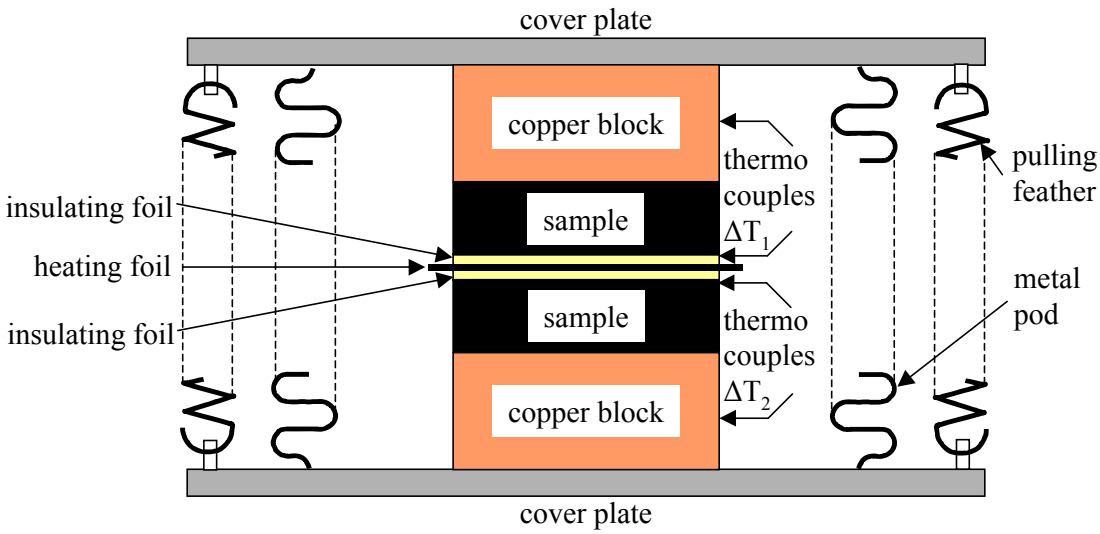

Figure 65 two-plate-apparatus without a hot guard

The two-plate-apparatus, as described in Figure 65, is enclosed by a vacuum-tight container. This container consisting of two cover plates and a metal pod, which allows to dip the whole apparatus in a cooling liquid, such as nitrogen, to also conduct low temperature measurements. The test specimens consist of two identical slabs, placed on either side of the flat heater. To reduce the above described disadvantages that flat heater is nowadays made out of an heating foil consisting of Constantan, instead of a heating plate. Opposed to the heating sides, of the samples cooling plates are placed which are usually made out of copper. As mentioned earlier, the system may include guarded heaters or rings, which have the function to prevent heat losses from the ends of the system. Those guarded heaters or rings make the measurement more accurate, but one has to keep in mind that it also means, that a significantly more effort has to be done, to conduct a measurement. The last major element for the determination of the thermal conductivity is the temperature gradient. This temperature gradient is measured

by means of differential thermocouples, which are mounted on the surface of the heater and the cooling blocks.

This kind of thermal conductivity measuring apparatus for polymers can be used in a temperature range between -180°C to +100°C, while the accuracy is in the order of ±2-3%.

For thermal conductivity measurements at low characteristic temperatures, i.e 0.1°K to 100°K a cylindrical test specimen is used (Figure 66). One end of that test specimen is in contact with a heating unit and the other end is in contact with a cooling unit to insure a thermal conducting connection. This was achieved in Figure 66 with a thread connection. The temperature drop in the axial direction is measured, with measuring elements, which are placed in holes perpendicular to the axis of the cylinder.

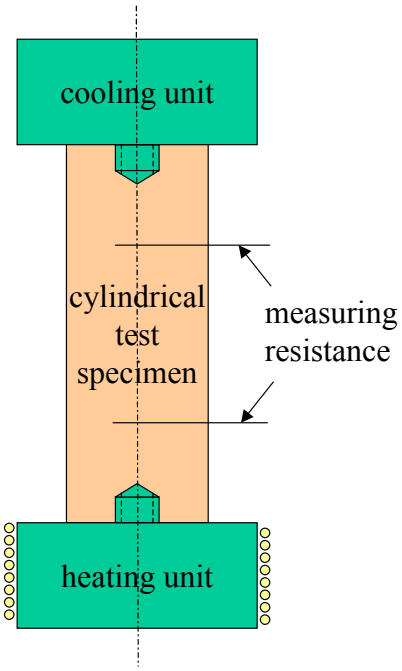

Figure 66 steady state measurement of the thermal conductivity at low temperatures

Looking at polymers (the kind of material used in this work), measurements of the thermal conductivity in the viscoelastic state causes a lot of problems. The above depicted plate measurement techniques can only measure polymers with extremely high molecular weights which do not start to flow under the influence of weak forces above the glass transition or melting point. One might think, that an apparatus for low molecular fluids could be used, but are left aside due to the caused problems, taking in the highly viscous high polymers and bubble creation at high temperatures and long testing times. Therefore an important element which has to be taken into consideration for an appropriate measurement technique is the phenomenon that at high temperatures and long times the thermal conductivity measurements can be distorted by the creation of bubbles. Figure 67 shows the scheme of such an apparatus (cylindrical apparatus) developed for flowable viscous high polymers [LohP-65].

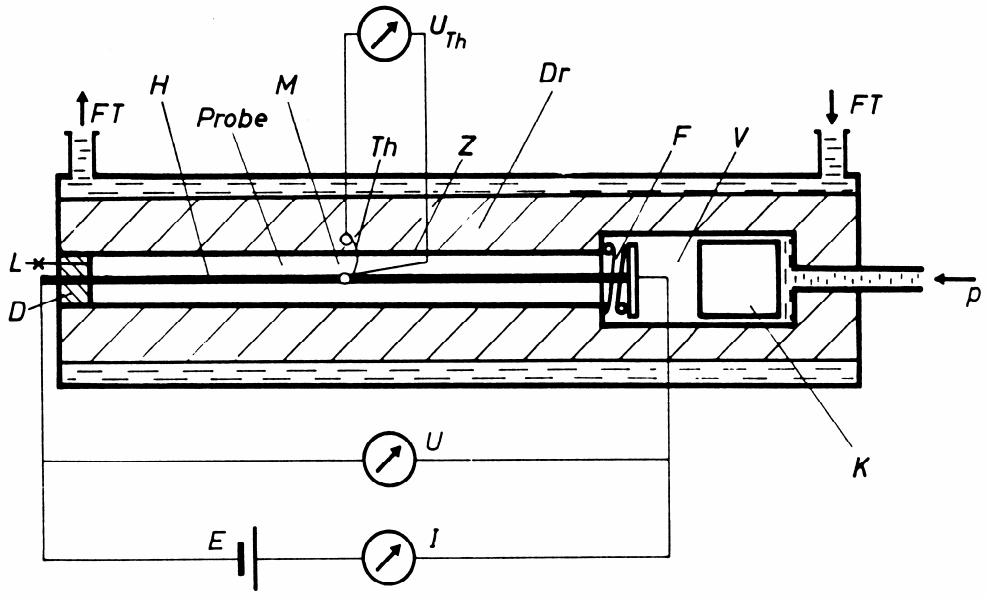

Figure 67 cylindrical apparatus [LohP-65]

A cylindrical heating element (H) consisting of a thin walled pipe made out of stainless steal and through which direct current is lead for heating purposes is enclosed by the viscous sample (Probe). The cylindrical probe room (M), in which the sample material is present, is directly connected to a supply room (V) in which the polymer is kept under constant pressure by means of a piston (K). The pressure container (Dr) is kept at a certain temperature with a liquid thermostat (FT). The temperature difference between the heating pipe (H), which is fed with the constant heating power $U \cdot I$, and the pressure container (Dr), is measured by means of two stationary thermocouples.

With this method the thermal conductivities of polymers in the temperature range between 80°C and 350°C and the pressure range up to 50 MPa can be measured.

4.6.3.2. Quasi Steady State Technique

The quasi steady state experimental techniques to measure the thermal conductivity λ are based on the principle that the system increases its temperature so slowly, that it could be said, that it is almost steady or quasi steady. The big advantage with this kind of measurement technique it is ability to measure the thermal conductivity λ continuously in a relative short period of time.

An example of such a system is depicted in Figure 68, in which the heat, from the heater pair, is conducted through the two probes to the heat reservoir in the middle (metal plate) to slowly heat up (quasi steady) the whole system. The reservoir is, as one can see from Figure 68, enclosed by a guard ring to protect it from heat losses, while the whole system is protected from heat losses by an adiabatic enclosure.

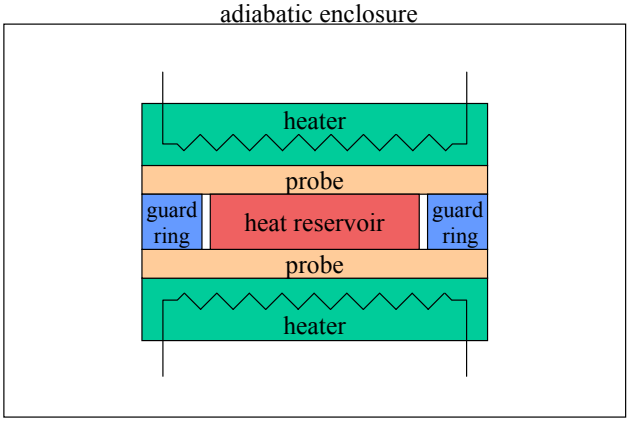

Figure 68 quasi steady two plate apparatus

Compared to the steady state thermal conductivity measurement techniques the temperature distribution in the examined sample depends upon time due to the fact, that

the system is heated with constant power input. The time dependant rise of the temperature in the heat reservoir and the temperature difference ΔT between the heaters and the heat reservoir are measured.

In the quasi steady measurement technique the heaters receive a constant power, which leads to a constant time and local heating speed if the heat capacity stays constant. Therefore, this kind of measurement technique provides generally wrong answers for the thermal conductivity λ, in those temperature regions, where the heat capacity is changing with time. Never the less, one has got the possibility to keep the errors form the changing specific heat capacities small my creating a heat reservoir with a high heat capacity. Therefore, the results are comparable with the steady state techniques.

4.6.3.3. Unsteady State Technique

The last measurement technique, of the above mentioned three techniques, to obtain the thermal conductivity is the unsteady state technique. The distinct feature, of this technique is, as one can imagine, the unsteady state of the system. In addition to that feature, those systems generally obtained the thermal conductivity λ indirect by e.g. actually measuring the thermal diffusivity a and the specific heat capacity to finally calculate the thermal conductivity λ with Equation (134). In the direct measurements of the thermal conductivity, as it was described in Section 4.6.3.1 and 4.6.3.2, it was necessary to find the heat flux, which caused some problems in the measurement

technique while the plain temperature measurements in the indirect measurement technique are much simpler.

Due to the variety of different unsteady state measurement techniques, a list and a brief description is presented below.

Modified Ångstrom Technique

The modified Ångstrom technique is one of those techniques, which are often used to determine the thermal diffusivity a. The thermal power is applied to the test specimen in form of a sinusoidal function of time. The thermal diffusivity a, can than be calculated by measuring the ratio of temperature at two points separated by length, period of thermal wave, and phase difference.

Impulse Technique

The impulse technique is an unsteady technique often used in a layer heat source configuration, similar to the configuration depicted in Figure 65. The calculations however are, in this case, based on the unsteady heating up process. By measuring the temperature difference between the heater, at any point in the sample, or the temperature changes of the heater; the specific heat capacity c_p, thermal conductivity λ and thermal diffusivity a can be simultaneously obtained.

Regular Regime of the First Kind Technique

Those devices, which resemble the regular regime of the first kind, measure the changes in the temperature distribution as a function of time in the sample. In this technique, the sample is placed in a media, which is kept at a constant temperature. Due

to intensive heat exchange on the surface of the sample, the thermal diffusivity values of the sample material can be obtained. To determine the thermal conductivity λ it is necessary to conduct additional measurements of the heat exchange on the surface.

Regular Regime of the Second Kind Technique (constant heating rate)

The main feature of the second kind, regular regime to measure thermal conductivity λ, is that the measurement of the thermal diffusivity α and thermal conductivity λ is conducted with a constant heating rate. By measuring the temperature of two points (separated by a constant length) in the test specimen the thermal diffusivity can be obtained. Because the temperature difference between theses two points is, in the one-dimensional case, inversely proportional to the thermal diffusivity α. To calculate the thermal conductivity it is then necessary to determine the heat flux going through the sample.

Heat Pulse or Flash Technique

The heat pulse or flash technique is quite useful, when it comes to the determination of the thermal diffusivity α. In this method the test sample (consists of a thin sample) is subjected to a very short pulse of radiant energy e.g. laser. The temperature of the back surface of the test sample, induced by this radiant heat pulse, is measured and the thermal diffusivity values are computed. To receive values for the thermal conductivity λ Equation (134) can be used, the values for the specific heat c_p and density ρ have been determined before.

Differential Scanning Calorimetry (DSC) Technique

The differential scanning technique as presented in Section 4.6.2.2 turns out to be an interesting approach to determine the thermal conductivity of polymers. In general one will find three different kinds of methods in the literature as presented by [KhTC-88] which are also depicted in Figure 69.

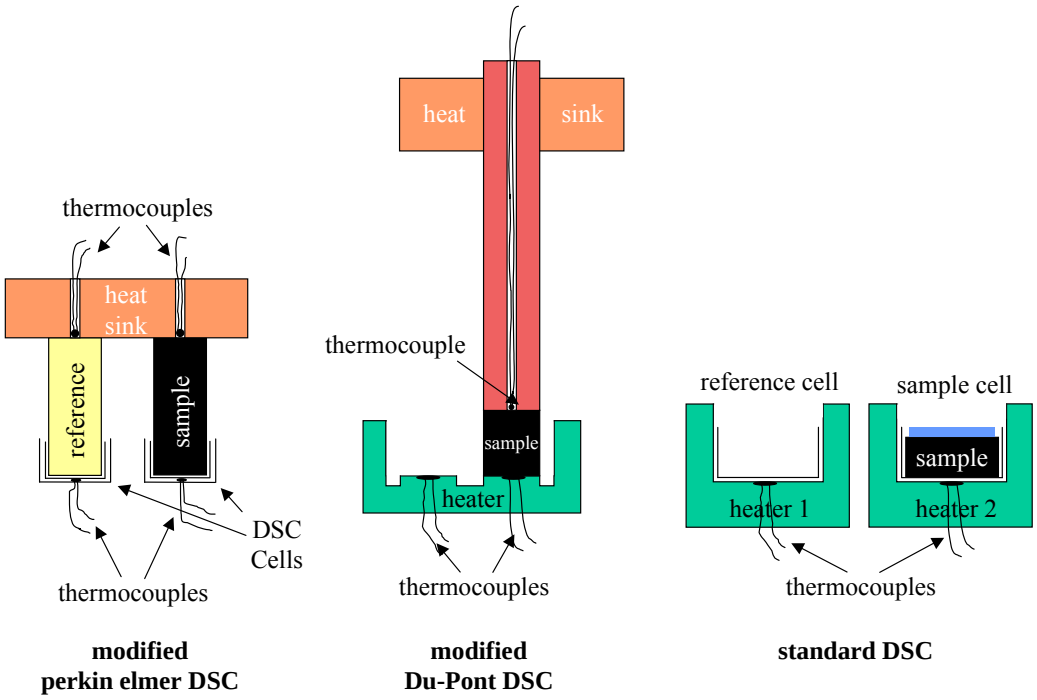

Figure 69 measuring the thermal conductivity with a DSC

Using one of the above depicted measurement methods give reasonable results. The most promising seams to be the standard DSC technique to determine the thermal conductivity, due to the fact, that it gives for different polymers such as PMMA very good results compared to the traditional methods.

In general the usage of the unsteady state techniques lead to shorter measuring times which is a big advantage. When evaluating, which measurement technique would be the most appropriate, totally depends on the specific application, but one should always keep in mind, that generally mistakes occur in the measurement, when in the temperature interval the thermal diffusivity e.g. at the glass transition is not constant.

4.7. Transmittance, Reflectance, Emittance, Absorptance

From the theory of Section 3.2 it is known, that the transmittance, reflectance, emittance, and absorptance are related as expressed in Equation (95) or (96) and the Kirchhoff's Law (Equation (98)). In Section 3.2 it was further mentioned that the reflectance and transmittance of an object, could be found by infrared spectroscopy. This spectroscopy and the principal with which it works is going to be explained later in this section. With these two values it is than possible to determine the absorptance mathematically. The result of such a spectroscopy is the graph presented in Figure 70 for black PMMA, while if one is interested in the angular absorptance behavior of black PMMA they are presented in Figure 71.

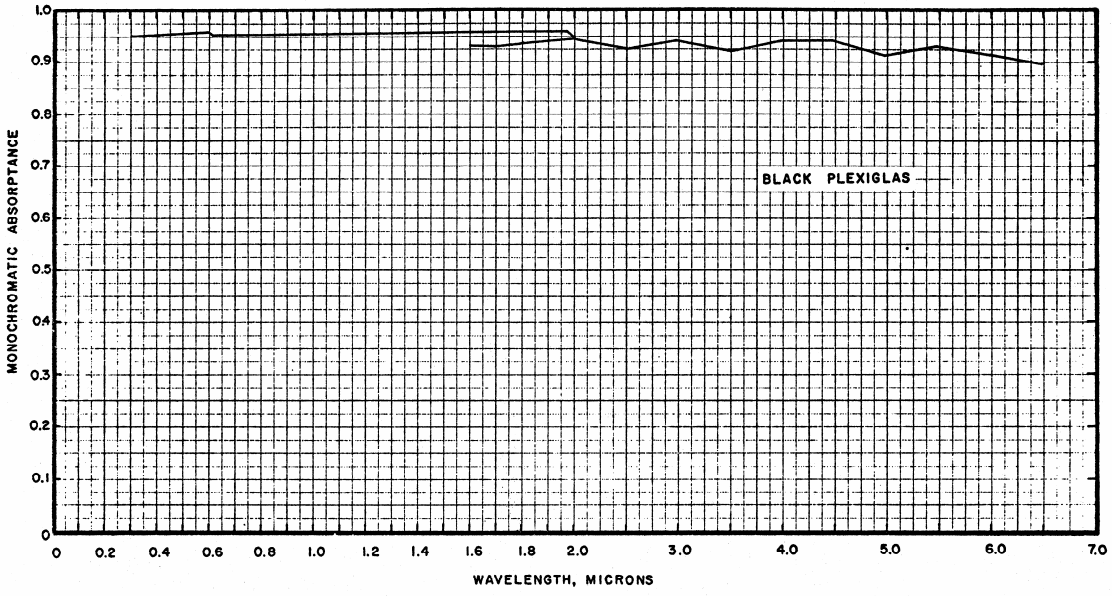

Figure 70 absorptance of poly(methyl methacrylate) versus wavelength [HalJ-71]

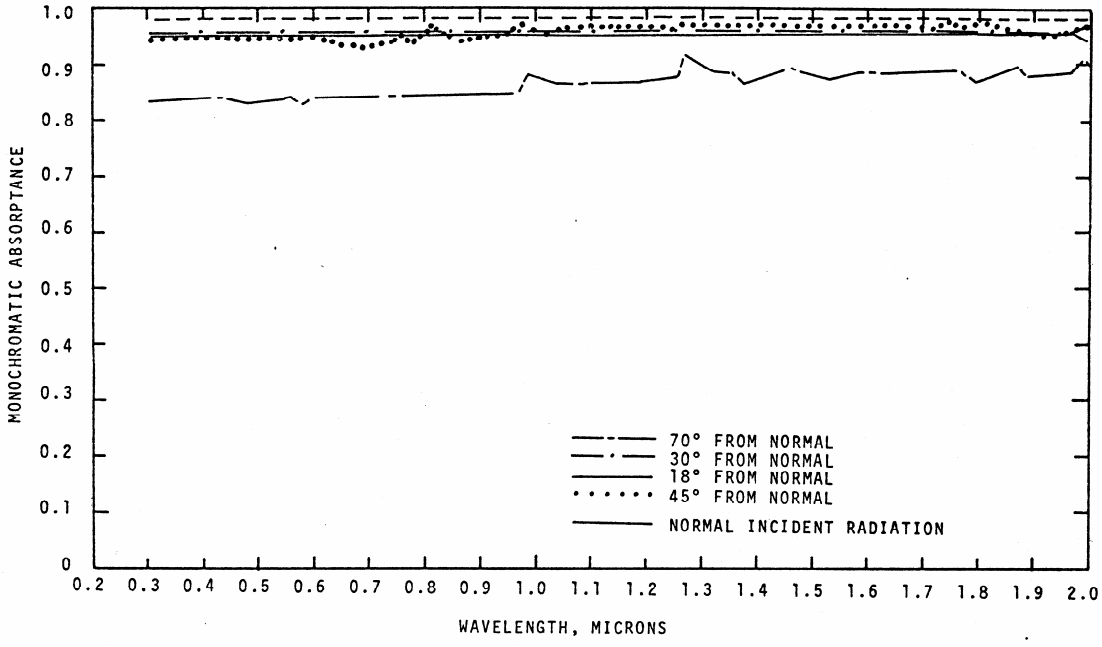

Figure 71 angular absorptance of poly(methyl methacrylate) versus wavelength [HalJ-71]

The depicted absorptance graph by Hallman [HallJ-71] was obtained, from a black colorless poly(methyl methacrylate) (Röhm and Haas) provided by Precision Plastics. That does not necessarily mean, that presented poly(methyl methacrylate) absorptance curve exactly depicting the here used PMMA (AcryliteFF from CYRO Industries), but it is very unlikely, that it differs distinctively from it. From Figure 70 one can determine, that the absorptance of PMMA is a constant value of 0.95 for all wavelength. Furthermore, it is of quite an interest, whether or not the absorptance of PMMA is time or radiation source dependent. The work, conducted by Hallman [HallJ-71] also includes such contemplation. His results are presented in Table 13 which present the average absorptance for several radiation sources, from which one can make the statement, that that no significant change in the absorptance are taking place when changing the temperature or the heat source. Thus it can be assumed, that the absorptance of PMMA has a constant value of 0.95.

PMMA		
Heat source	Temperature	Absorptance value a
Black body	1000 °K	0.94
	1500 °K	0.94
	2000 °K	0.95
	2500 °K	0.95
	3000 °K	0.95
	3500 °K	0.95
Flames		0.94
Solar		0.96

Table 13 average absorptance for several radiation sources

Infrared spectroscopy

The infrared or IR spectroscopy is a spectroscopic technique where molecular vibrations are analyzed and reflections are measured. To understand the concept on which the IR spectroscopy is based the principles of simple harmonic molecular motions have to be understood. Therefore a descriptive introduction into the simple harmonic motion is presented below.

A chemical bond between two atoms can be thought of as a simple harmonic oscillator, which can be imagined by two spheres, or masses, connected with a spring as presented in Figure 72. This system represents a simple harmonic oscillator, as commonly referred to in dynamic observations and models.

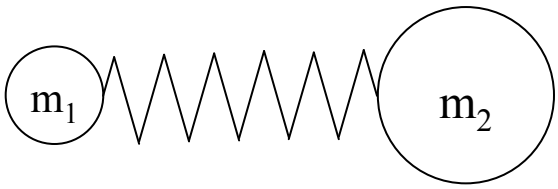

Figure 72 simple harmonic oscillator

Setting this system into motion results in an oscillation, or vibration of, the two sphere on the spring. The back and forth movement of the simple harmonic oscillator, if not disturbed and/or damped, will oscillate infinitely with a certain frequency depending on the masses of the spheres and the stiffness of the spring, according to basic dynamic principles.

Relating the imaginative spring-mass (mechanical) system back to the bondage-atom (chemical) system, one can see, that the springs represented the bond between two atoms, while the masses represented the two atoms, or groups of atoms, connected by the bond. Keeping the model in mind, it is obvious, that when atoms have different masses, and single, double and triple bonds have different stiffnesses, each combination of atoms and bonds has its own characteristic harmonic frequency.

An essential fact for the IR spectroscopy is known from the theory of dynamic system. Having a vibrating object, vibrating at a certain frequency, which encounters another vibration of exactly the same frequency, will absorb that energy. This is also valid for vibration of molecules and is essentially for the further contemplations. Little simple harmonic oscillators, which make up any molecule, at any temperature above absolute zero, vibrate vigorously. It happens to be, that the frequencies of vibrating molecules fall into the same range as infrared light. Therefore, if a vibrating molecule is hit with infrared light, it will absorb those frequencies of the infrared light which exactly match the frequencies of the different harmonic oscillators that make up that molecule. As mentioned above, when this light or energy is absorbed, the little oscillators in the molecule will continue to vibrate at the same frequency, but since they have absorbed the energy of the light, their vibration will have a larger amplitude.

In the infrared spectroscopy, a sample material will be exposed to an infrared light and the remaining light, which was not absorbed by any of the oscillators in the molecule, is transmitted through the sample and recorded by a detector. Furthermore,

the reflectance is measured. Love [LovT-68] as discussed several methods with which the measurement of the surface absorptance can be measured.

A computer analyzes the transmitted light received from detectors to determine what frequencies were absorbed. For a long time good data was only achieved by hitting the molecule with only one frequency of infrared light at a time, which lead to, as one can imagine, a very long testing time due to the big infrared spectrum and the need for several scans to obtain good data. The usage of a Fourier Transform Algorithm (Equation (136) and (137)) made it recently possible to hit the molecules with every frequency of infrared light at once, and get a perfect spectrum in a very short period of time.

$$F(\upsilon) = \int_{-\infty}^{\infty} f(t)\, e^{-i(2\pi)\upsilon t} dt \tag{136}$$

$$f(t) = \int_{-\infty}^{\infty} 2\pi\, F(\upsilon)\, e^{i(2\pi)\upsilon t} dt \tag{137}$$

5. Analysis

The analysis of the collected data is the subsequent part of this work. The data was collected with the purpose of identifying the onset of pyrolysis. As shown in previous sections different signatures, temperature, mass loss and flow visualization where used to identify this event. Characterization of the onset of pyrolysis allows for the determination of t_p, independent of the ignition event. The difference between the ignition and pyrolysis time will determine the mixing time, t_m. From the empirical pyrolysis time the thermal inertia can be extracted and from the ignition time the minimum fuel concentration in the natural boundary layer required for ignition. The following sections will provide a detailed description of this procedure.

The definition of the pyrolysis time, t_p, and temperature, T_P, is not trivial. Two different signatures were correlated to determine this time, mass loss and flow visualization. The onset of the detectable mass loss was deemed to be the pyrolysis time and this time was compared with the time where the first fuel vapors were observed. Having determined the pyrolysis time, the corresponding surface temperature was deemed to be the pyrolysis temperature.

5.1. Mass Loss

The mass loss information extracted from the mass measurements is discussed in this section. Theoretically, deviation from zero of the first derivative of the mass

history, $\frac{dm}{dt}$, would indicate pyrolysis. This is theoretically correct, but is practically difficult to obtain since the relatively small mass loss requires a very sensitive scale to record the changes, which create oscillations due to surrounding conditions. Mass loss measurements were conducted with and without thermocouples and in general comparison showed that thermocouples attached to the surface would interfere with the mass measurements, therefore, those readings were disregarded. The mass loss experiments required extreme caution. Reproducible results could only be obtained when a correct placement of the specimen on the scale was achieved. Appropriate pre-conditioning of the samples was done, air movements were minimized (turning the exhaust hoods off and enclosing the test apparatus) and insuring that nothing but the scale is in touch with the sample and sample-holder (such as thermocouples). Even with these precautions the scatter in the obtained data, is obvious. To reduce the error, the data presented will be average data over a time interval small compared to the total time of the test.

Therefore, even with these errors, it is possible to determine that one of the signatures that mark the onset of pyrolysis is the sudden initiation of weight loss from the sample. Figure 9 and Figure 17 are characterized by an almost constant mass until the attainment of a characteristic temperature, at this point the mass loss recordings can be registered and an increasing slope can be registered until it reaches a steady state value. A single case, for an incident heat flux $\dot{q}_i''$ of $35.6 \frac{kW}{m^2}$, has been used to

illustrate the time evolution of the fuel mass loss per unit are $\dot{m}_f''$ and compare it with two predictions. The exact value of L_v, for the material studied is unknown. Therefore, two representative values from the literature are used to calculate the mass loss evolution. The first one was obtained using a latent heat of vaporization L_v for PMMA of $1620\ \frac{J}{g}$ [DryD-85] and the second one $420\ \frac{J}{g}$ [SKBK-91]. Figure 73 shows that the mass loss falls somewhere in between the predicted values.

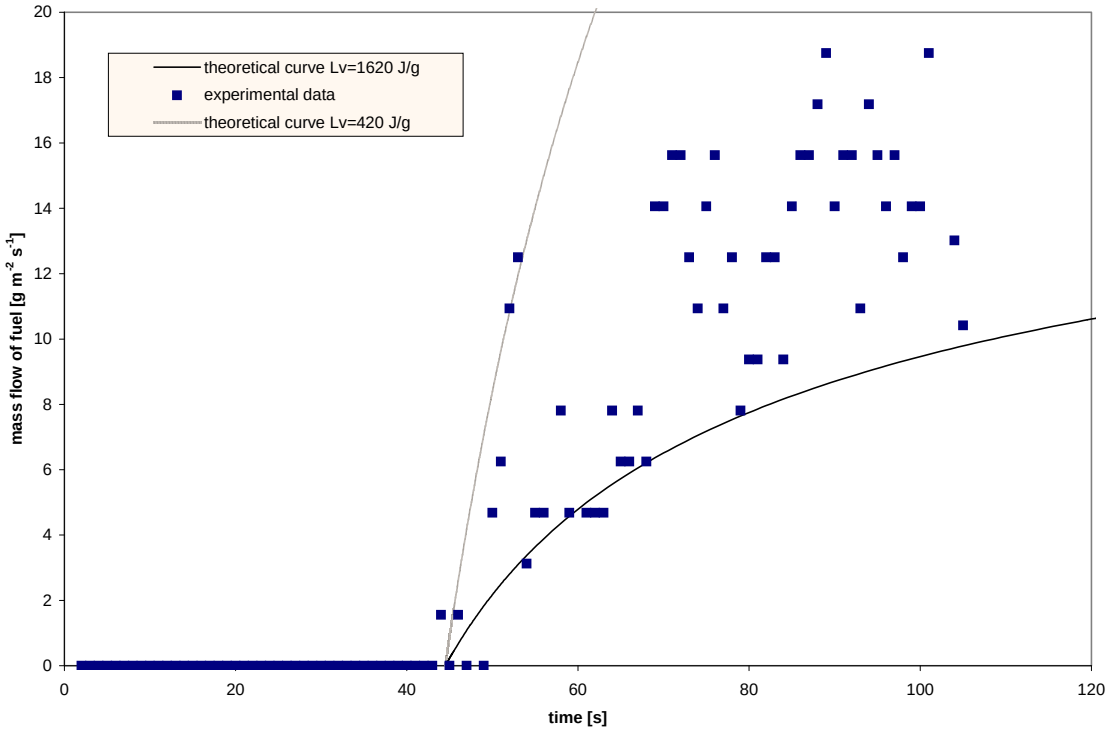

Figure 73 the fuel mass loss per unit are $\dot{m}_f''$ from experimental data compared with two predictions

5.2. Pyrolysis Time t_p

As explicitly described in Section 3.1.1.1 the pyrolysis time, is the time the fuel sample needs to attain the pyrolysis temperature T_p at the exposed sample surface, starting to count from the time, the sample specimen is placed for testing in the test apparatus. The pyrolysis temperature can be obtained from the literature but discrepancies are common and generally attributed to the specific PMMA. In this case the pyrolysis temperature will be determined through the initiation of the mass loss or through the visualization of the first smoke by means of the laser. Discrepancies can be found between both techniques and flow visualization will be preferred since it results in fewer scatters.

The results obtained are presented in Figure 74 as $\frac{1}{\sqrt{t_p}}$ versus the incident heat flux $\dot{q}_i''$, which corresponds to Equation (41). As one can see from Figure 74 the obtained data falls nicely into a straight line. Nevertheless one might also see, that the difference between the acquired data points and the straight line increases with an increasing incident heat flux $\dot{q}_i''$. From the tests themselves (how they are conducted, etc.) the reason for that clearly is, the error in manual time measurement at the onset of pyrolysis. A small error (e.g.1 sec), at high incident heat fluxes $\dot{q}_i''$ (short pyrolysis times t_p (e.g. 20 sec)) lead to relative big measuring error, while an error at low incident heat fluxes $\dot{q}_i''$ (log pyrolysis times t_p (e.g. 200 sec)) leads to a relative small measuring error.

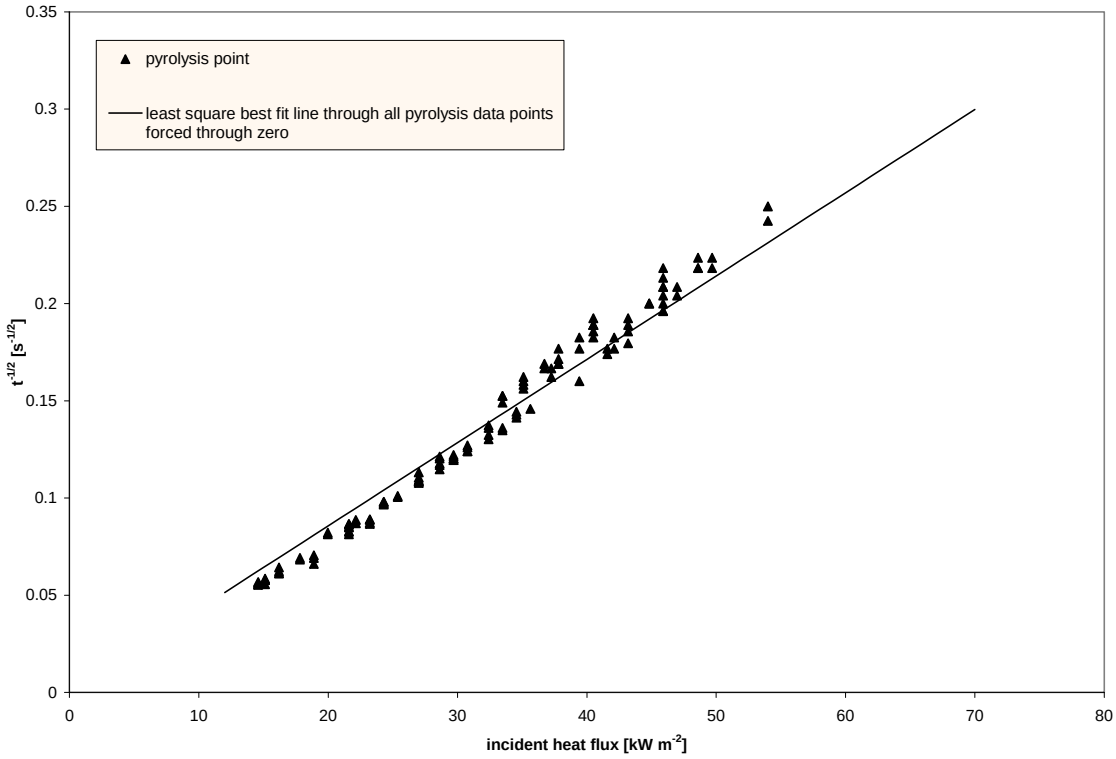

Figure 74 pyrolysis time $\frac{1}{\sqrt{t_p}}$ versus the incident heat flux $\dot{q}_i''$

The linear function for the line presented in Figure 74 was obtained, by conduction a least square best fit analysis, forced through zero (as predicted by Equation (41)), which resulted in the presented line, where the slope gives

$$\text{SLOPE} = \frac{2}{\sqrt{\pi}} \frac{\bar{a}}{\sqrt{\lambda \rho c_p}} \left(T_p - T_\infty\right) \tag{138}$$

Recalling one of the final statements made in Section 3.1.1.1, which concluded, that Equation (41) is valid for incident heat fluxes $\dot{q}_i''$, which are higher than the critical

heat flux. Therefore, for the here conducted tests it is safe to say, that Equation (41) can be used over the whole rage of conducted tests, where the incident heat flux $\dot{q}_i''$ ranged from around $15\frac{kW}{m^2}$ up to $55\frac{kW}{m^2}$. For the least square best fit line depicted in Figure 74, for the sample specimen consisting of the in Section 4.3 described PMMA, the slope was found to be:

$$SLOPE = 4.283 \cdot 10^{-3} \left[\frac{m^2}{kW\sqrt{s}} \right] \tag{139}$$

Assuming, that the absorptivity is close to unity, $\bar{a} \approx 1$ [HalJ-71], leaves the global property, $\overline{\lambda \rho c_p}$, which referred to as the global thermal inertia, as the single material property determining the time for attainment of pyrolysis. For the PMMA used here this single global material property is:

$$\overline{\lambda \rho c_p} = 1156405 \left[\frac{W^2 s}{m^4 K^4} \right] \tag{140}$$

With this property it is now possible to determine the pyrolysis time t_p for every incident heat flux, which is reasonably above the critical heat flux $\dot{q}_{i,cri}''$.

5.3. The Pyrolysis Temperature (T_p)

The pyrolysis temperature is therefore defined as the temperature at t_p. As it was presented in Section 2.1, Figure 8 represents a typical temperature versus time graph. It

is important to note again, that IR-measurements showed that the temperature during pyrolysis does not change significantly. This is in contrast with thermocouple measurements. It was also mentioned that the thermocouples did not remained attached to the surface, thus errors can be expected.

The pyrolysis temperature obtained is presented in Figure 75. The temperatures presented are mostly from thermocouple measurements. As one can see from the figure, the scatter for the first tests is relatively big compared to the rest of the tests. The tests are presented chronologically to show the differences between the two fixation methods used. For the earlier tests the thermocouple was only slightly embedded into the sample surface, which contributes to the above-described problems resulting in a larger scatter. After imbedding the thermocouples deeper under the surface of the sample specimen, the measuring scatter decreased, but the average pyrolysis temperature T_p stabilized slightly under 265°C, which is the pyrolysis temperature given by the manufacturer.

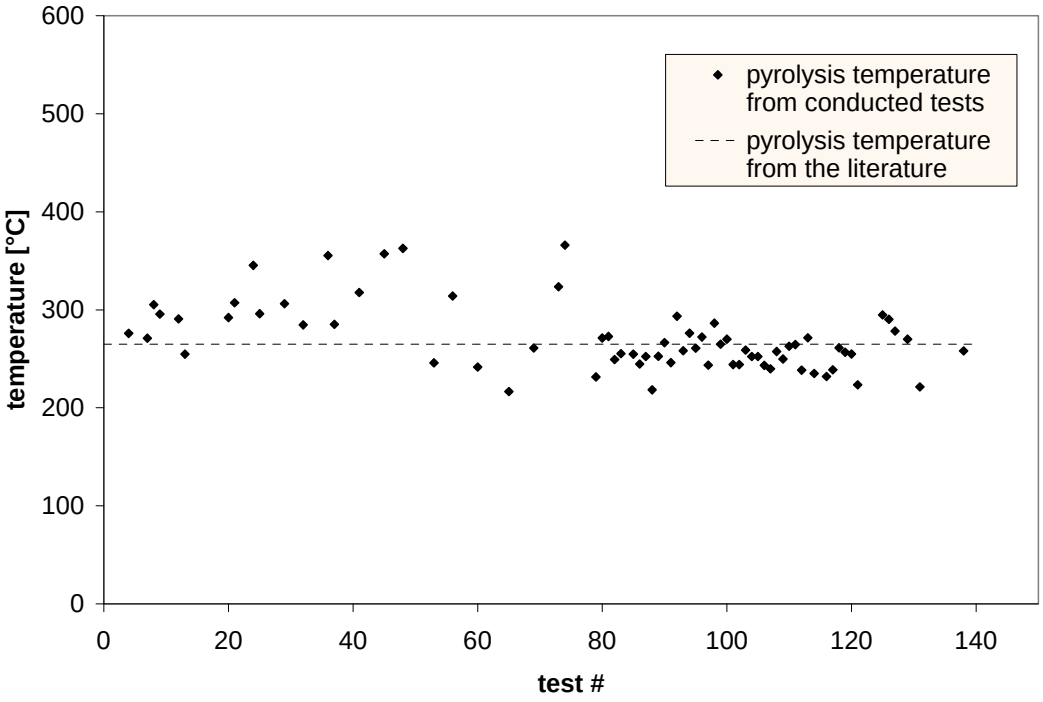

Figure 75 thermocouple reading on the surface of the sample at the onset of pyrolysis (t_p)

5.4. Discrepancies between Ignition and Pyrolysis Time

The above information allows to conclude, that until pyrolysis occurs, the fuel heats as an inert solid with no combustible gases escaping the surface. Therefore this period can be considered to be independent of the environment, leading to a thermal inertia value that can be extrapolated to different environmental conditions. In contrast, once the fuel begins to release volatiles, environmental conditions will determine the mixing time, t_m. Therefore, the thermal inertia value that can be extracted from the ignition time will somehow depend on the particular testing conditions.

Under the particular conditions of these experiments, t_m can be extracted in an attempt to obtain further information that can be considered to depend on the material and not on the environment. Furthermore, an estimation of the influence of environmental conditions on the value of the thermal inertia, as extracted from the ignition delay time, can be determined.

This section will address the comparison of the ignition and pyrolysis delay time. Both times are initiated at the time when the sample material is placed in the experimental apparatus. The pyrolysis time t_p ends at the point, when flammable gases leave the surface of the sample material, while the ignition time t_{ig} ends, when the flammable gases ignite as described in depth in Chapter 3.

In the past a large number of tests have been conducted using the LIFT apparatus (ASTM E1321) to determine flammability characteristics, such as the ignition time t_{ig}, of different materials. The distinct feature of that testing apparatus is the strong pilot flame, which is used to eliminate the induction time t_i in the ignition process as described in Chapter 3. Long [LonR-98] and Quintere [QuHa-84] have used this apparatus to determine the ignition properties for PMMA and used Equation (41) to determine the global thermal inertia $\overline{\lambda\rho c_p}$. Long and Quintere assumed that the mixing time t_m and induction time t_i could be neglected due to their small magnitude relative to the pyrolysis time t_p.

A major part of this work is dedicated to assess this assumption, therefore, a well known sample material, poly(metyl metacrylate) (PMMA), was used as a reference test specimen. Looking at Figure 76, where the results of Long [LonR-98], Quintere [QuHa-84] and this work are presented the obvious discrepancy between the ignition time t_{ig} (Long and Quintere) and pyrolysis time t_p can be seen.

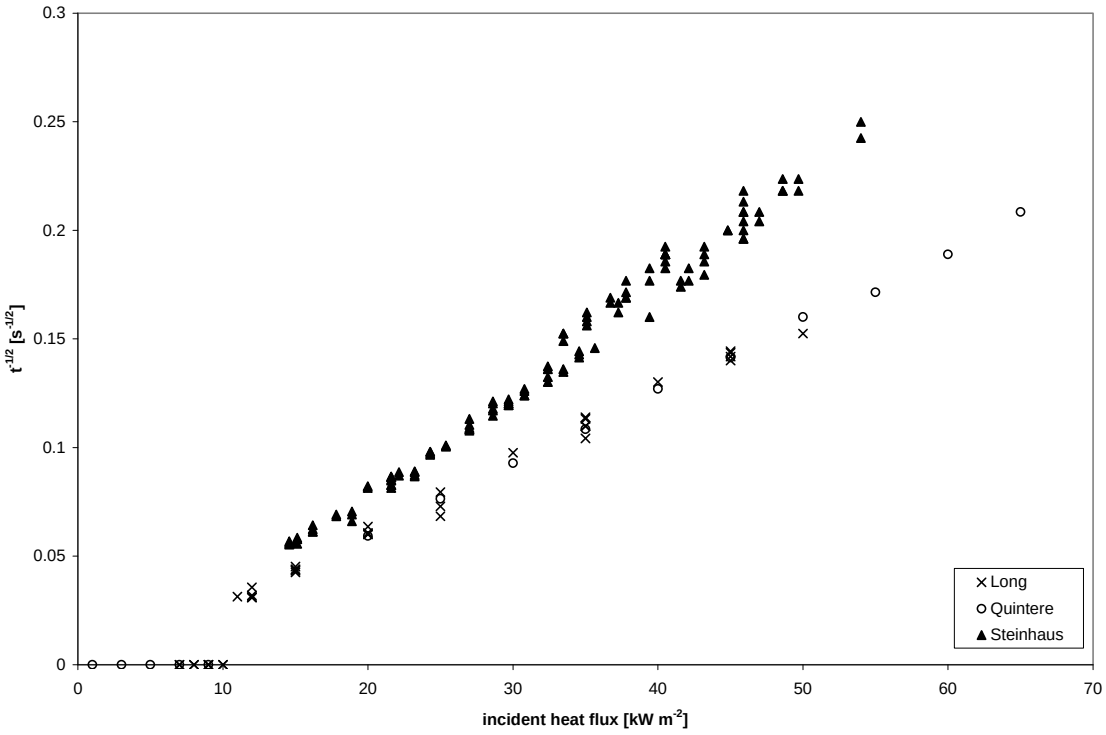

Figure 76 discrepancies between ignition and pyrolysis data points

It is clear, looking at Figure 76, that both the ignition and pyrolysis time results seem to be linear and therefore the use of Equation (41) is not unreasonable. When solving for $\overline{\lambda\rho c_p}$ the solution does not resemble the real global thermal inertia $\overline{\lambda\rho c_p}$

which is a material constant. Applying the same rules to the data points acquired by Long [LonR-98] and Quintere [QuHa-84] as described in Section 5.1, one obtains the slope as sown below

$$\left.\mathrm{SLOPE}\right|_{t_p=t_{ig}} = 3.102\cdot 10^{-3}\left[\frac{m^2}{kW\sqrt{s}}\right] \tag{141}$$

and the global thermal inertia $\overline{\lambda\rho c_p}$

$$\left.\overline{\lambda\rho c_p}\right|_{t_p=t_{ig}} = 2204290\left[\frac{W^2 s}{m^4 K^4}\right]. \tag{142}$$

Looking at the values for that global thermal inertia $\overline{\lambda\rho c_p}$ found with the pyrolysis time t_p and than with the ignition time t_{ig} shows two distinct different values as presented in Equation (140) and (142). This fact leads to the assumption, that there is a definite difference between the two analyses on the order of a factor of 2. The introductory remarks of ASTM-E-1321 that stress that the results from the LIFT provide appropriate parameters for comparison but do not represent absolute values that can be extrapolated to different scenarios, are thus justified.

When analyzing Figure 76 by drawing a least best fit line, through the ignition and pyrolysis data of Figure 76 forced through zero, the result is Figure 77.

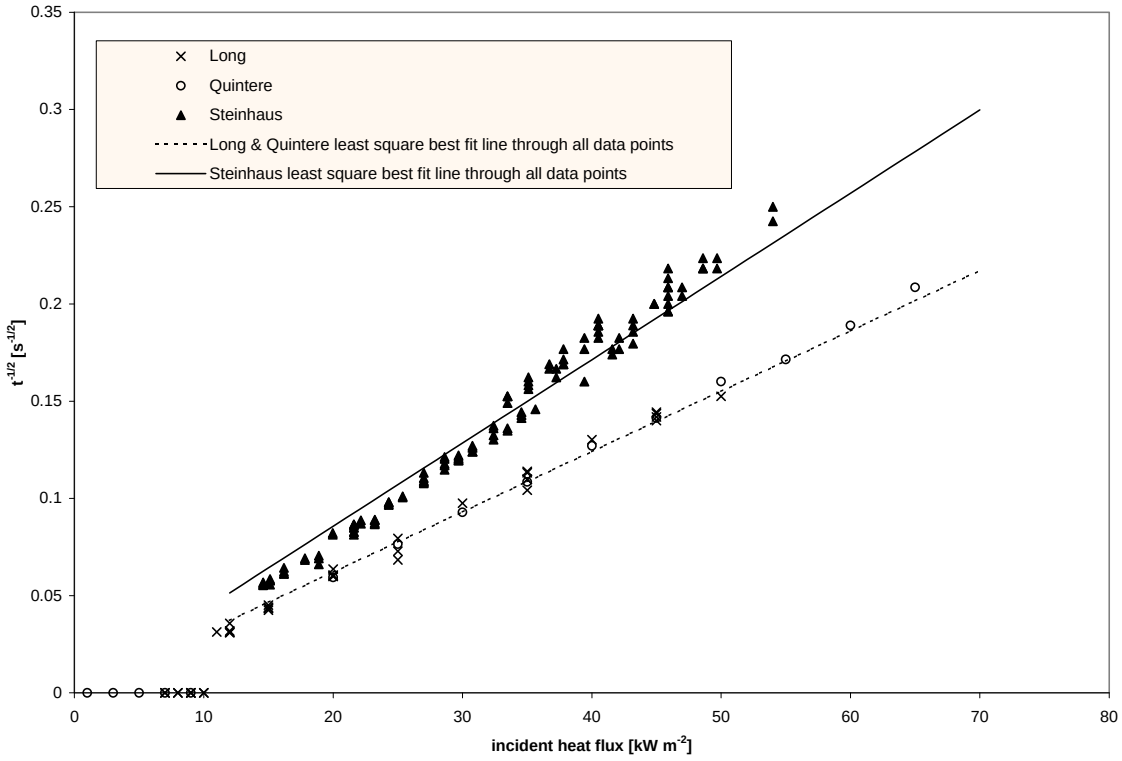

Figure 77 least square best fit lines through the ignition and pyrolysis data points

When subtracting ignition time t_{ig} from the pyrolysis time t_p it can be seen, as presented in Figure 78, that the difference between them decreases with a rising incident heat flux $\dot{q}_i''$.

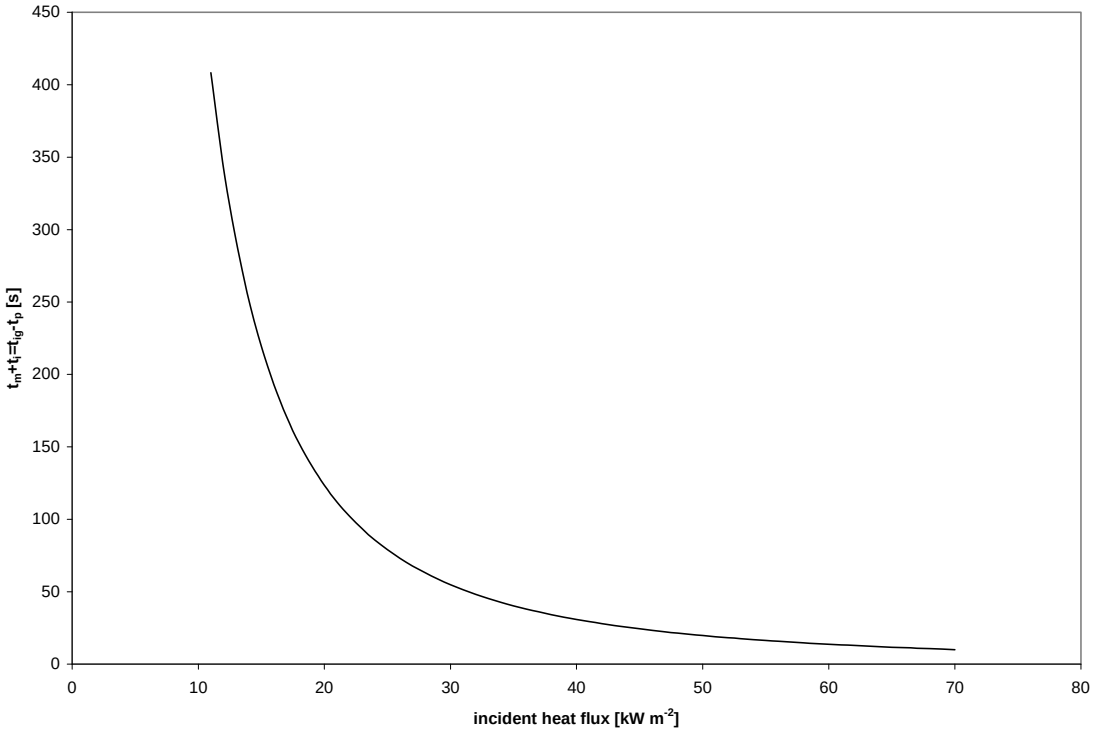

Figure 78 mixing and induction time ($t_m + t_i$) or ignition minus pyrolysis time ($t_{ig} - t_p$) versus incident heat flux $\dot{q}_i''$

Plotting the mixing and induction time ($t_m + t_i$) or ignition minus pyrolysis time ($t_{ig} + t_p$) of Figure 78 as one over square root of t ($\frac{1}{\sqrt{t_m + t_i}} = \frac{1}{\sqrt{t_{ig} - t_p}}$) leads to the following figure.

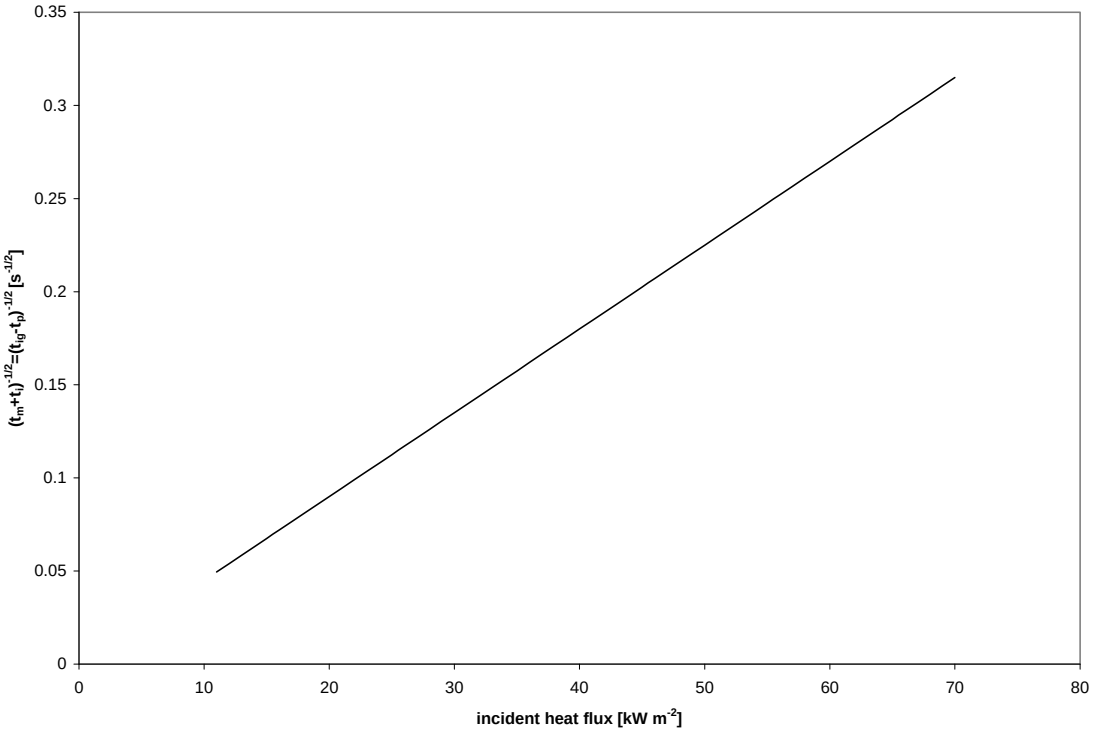

Figure 79 one over the square rout of mixing and induction time ($t_m + t_i$) or ignition minus pyrolysis time ($t_{ig} - t_p$) ($\frac{1}{\sqrt{t_m + t_i}} = \frac{1}{\sqrt{t_{ig} - t_p}}$) versus incident heat flux $\dot{q}_i''$

5.5. Mixing and Induction Time

The distinct differences between the pyrolysis time t_p and ignition time t_{ig} as depicted in the previous section lead to an analysis of the post pyrolysis process as described theoretically in Section 3.1.2. To proceed with that aim, the following values as presented in Table 14 were therefore chosen to represent Long's [LonR-98] and Quintere's [QuHa-84] test setup (LIFT(ASTM-E-1321)) results to which the present data is compared to.

Description	Symbol	Value	Units	References
Pyrolysis temperature of PMMA	T_p	538.15	K	
Ambient temperature	T_∞	294.15	K	
Absorptivity of PMMA	a	1	-	
latent heat of evaporation of PMMA	L_v	1620	J g^{-1}	[DryD-85]
Characteristic length	L	0.13	m	ASTM E 1321
Prandel number	Pr	1	-	
Thermal inertia of PMMA	$\lambda\rho c_p$	1156406.2	W^2 s m^{-4} K^{-2}	Section 5.2
Density of air @ 538.15 K	ρ	696.4	g m^{-3}	[BeeH-92]
Specific heat capacity of air @ 538.15 K	c_p	1.03	J $g^{-1}K^{-1}$	[BeeH-92]
Thermal conductivity of air @ 538.15 K	λ	0.0407	W m^{-1} K^{-1}	[BeeH-92]
Distance from the leading edge	x	0.155	M	ASTM E 1321
total heat transfer coefficient	h_t	11	W m^{-2} K^{-1}	[LonR-98]

Table 14 post pyrolysis process calculations

With the values from Table 14 it is possible to calculate the mass flow rate per unit length $\dot{m}'_f(\tau)$ which is depicted in Figure 27 per unit area and the mass flow rate of the oxidizer per unit length $\dot{m}'_o(x)$ as depicted in Figure 29. With those values one can calculate the mass fraction of fuel Y_f using Equation (72), which results in the curves as presented in Figure 80.

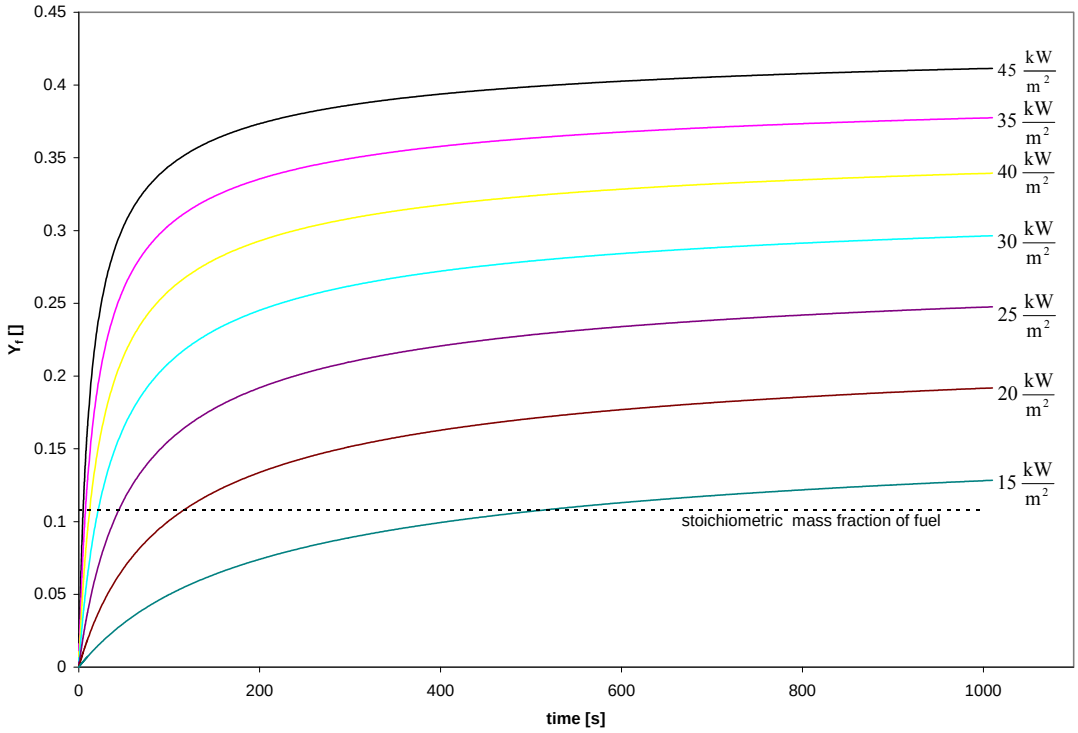

Figure 80 mass fraction of fuel Y_f versus time

From by Long [LonR-98] and Quintere [QuHa-84] the ignition times t_{ig} and thus one can determine the minimum fuel mass fraction necessary for piloted ignition to occur, $Y_{f,L}$. The results obtained for the following incident heat fluxes $\dot{q}_i''$= 15, 20, 25, 30, 35, 40, and 45 $\left[\frac{kW}{m^2}\right]$ are presented in Figure 81, where a least square best fit line is laid through the data points, which leads to the Equation (143).

$$Y_{f,L} = 8.569 \cdot 10^{-3} + 5.180 \cdot 10^{-3} q_i'' \qquad (143)$$

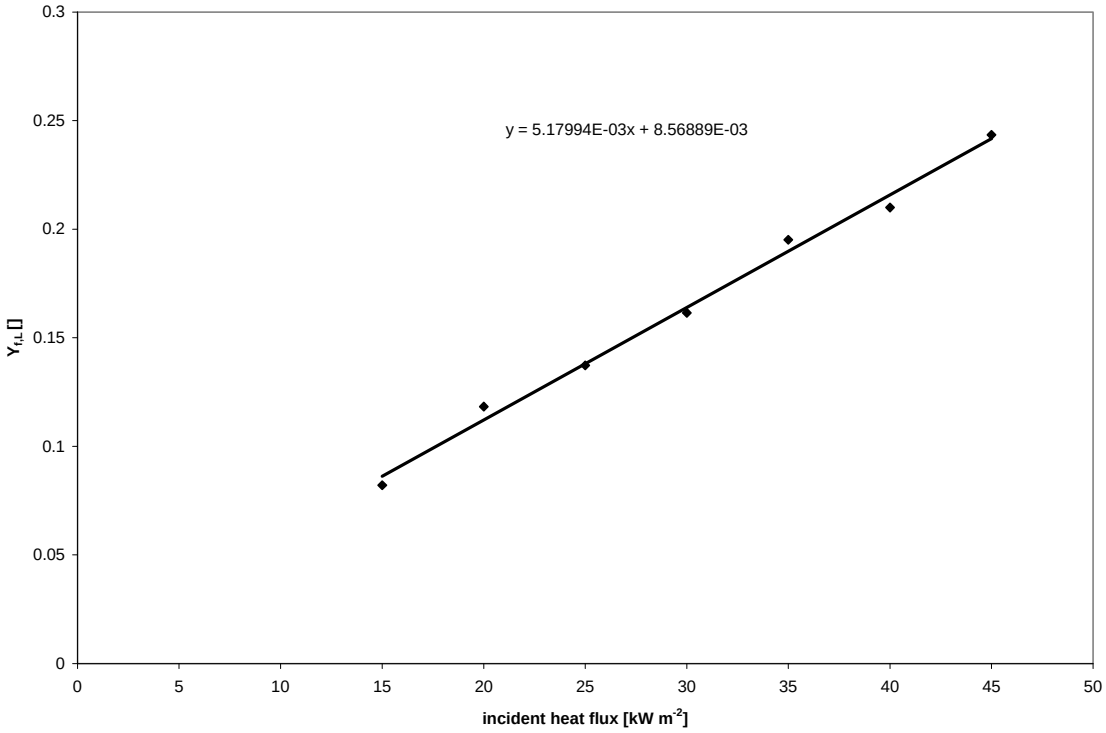

Figure 81 lean flammability mass fuel fraction $Y_{f,L}$.

These results differ from those presented, following a similar analysis, by Long [LonR-98]. The main difference is the use of a different global thermal inertia. Long showed an almost constant lean flammability fuel mass fraction $Y_{f,L}$, that only increased for heat fluxes greater than 30 kW/m^2.

The dependency of $Y_{f,L}$ on the external heat flux show the need to further explore the different stages of the ignition process after onset of pyrolysis. The mass loss curve shows a lag with respect to the pyrolysis time (as obtained from the laser),

this lag seems to be a function of the external heat flux and might be the origin of this discrepancy. This issue could be a subject of future work.

Thus the lean flammability mass fuel fractions $Y_{f,L}$, for the LIFT apparatus (ASTM E1321) and PMMA follows the curve depicted in Figure 81. Therefore with the obtained lean flammability mass fuel fractions $Y_{f,L}$ it is possible to determine the characteristic time between the onset of pyrolysis and ignition, for every incident heat flux $\dot{q}_i''$. The results are presented graphically in Figure 82 and Figure 83.

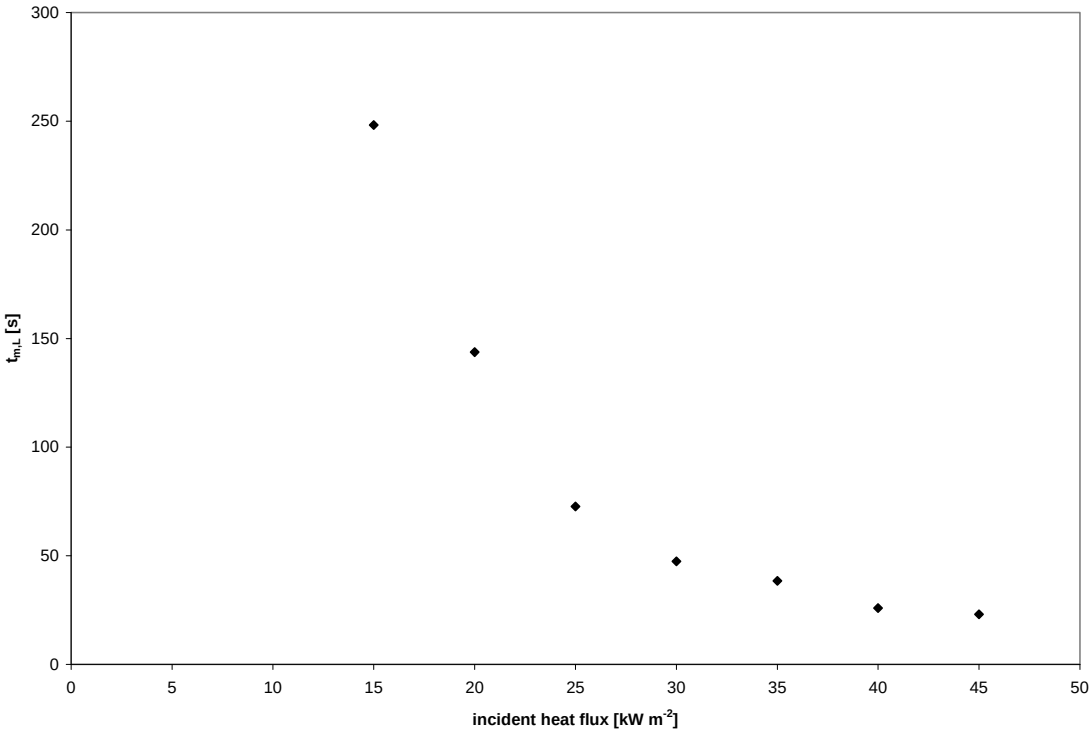

Figure 82 lean flammability mixing time $t_{m,L}$ versus incident heat flux $\dot{q}_i''$

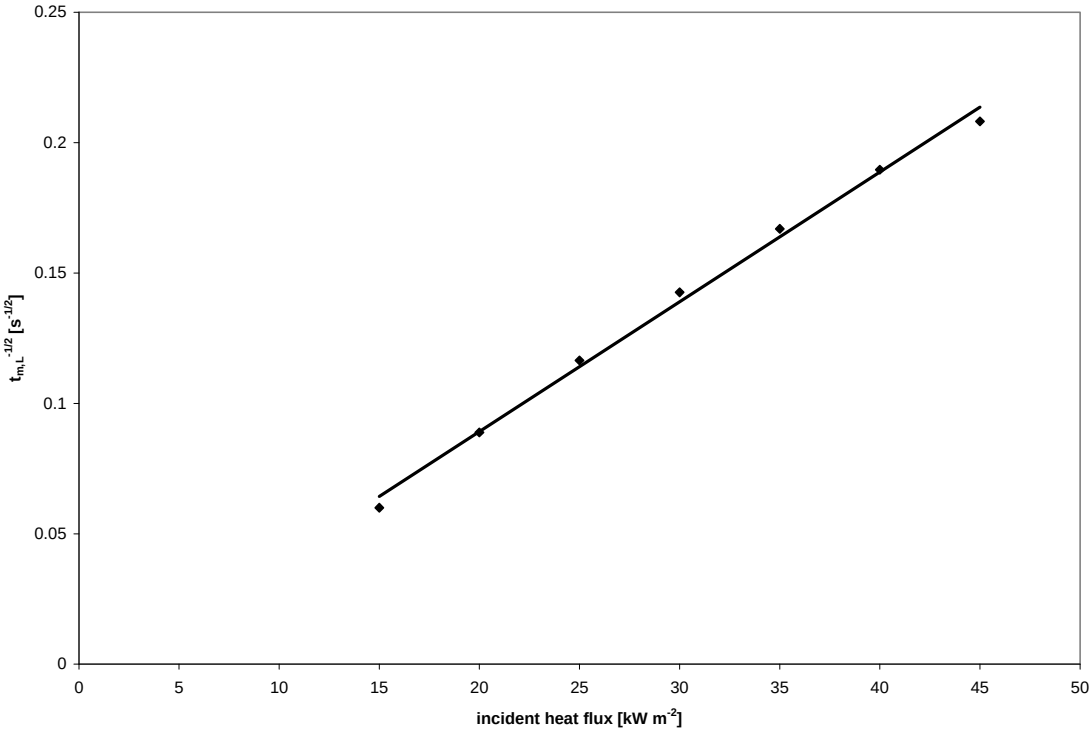

Figure 83 lean flammability mixing time ($\frac{1}{\sqrt{t_{m,L}}}$) versus incident heat flux $\dot{q}_i''$

5.6. Calculated Ignition Time

As it was determined, from Section 5.2 and 5.5, where the material property $\overline{\lambda\rho c_p}$ (global thermal inertia) was determined (Equation (140)) and a material and apparatus dependant function for the lean flammability mass fuel fraction $Y_{f,L}$ was found (Equation (143)). With these values it is now possible to calculate the ignition delay time. The pyrolysis time t_p is obtained using Equation (140) and the mixing time t_m by means of Equation (143). It is assumed that the induction time t_i is zero and, therefore, Equation (8) applies. The results are presented in Figure 84.

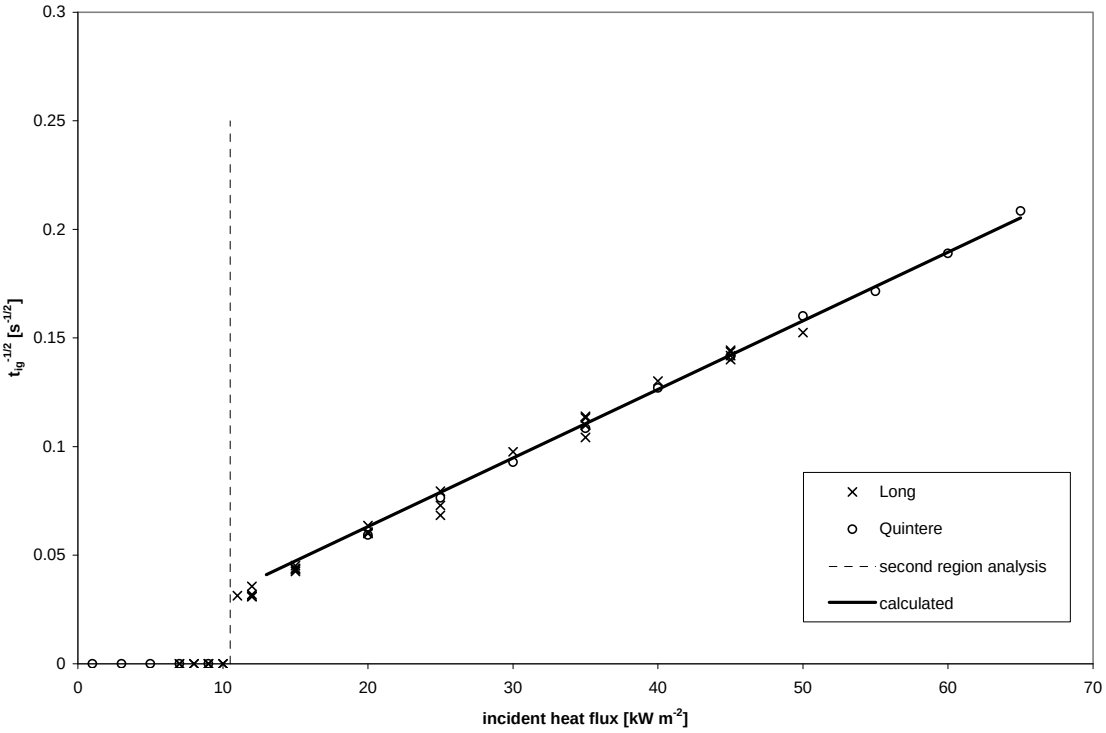

Figure 84 calculation and reality comparison of the ignition times t_{ig} versus incident heat flux $\dot{q}_i^{"}$ calculation

5.7. Thermal Inertia $\lambda\rho c_p$ Considerations

The thermal inertia $\lambda\rho c_p$ of Section 3.1 is one of the basic parameters in the determination of the ignition or pyrolysis time (t_{ig} or t_p), thus its value, for each material, plays an important role in the fire characterization process of a material. Of particular interest are the ways, which are available to determine the value for the thermal inertia $\lambda\rho c_p$ as used in Section 3.1. From e.g. Long [LonR-98] and Quintere [QuHa-84] it becomes clear, that their results for thermal inertia $\lambda\rho c_p$ of a material can predict, according to the theory in Section 3.1, the ignition time for an incident heat flux

$\dot{q}_i''$. The question, which one might ask, is whether or not it is possible to predict the ignition or pyrolysis time (t_{ig} or t_p) with or without having to conduct ignition or pyrolysis tests.

Literature result

From the literature as presented in Section 4.6 it is possible to experimentally determine the thermal conductivity λ, density ρ, and specific heat c_p as a function of temperature. Multiplying the values of the thermal conductivity λ, density ρ, and specific heat c_p as they were presented in (Figure 50, Figure 54, and Figure 64), for each temperature, leads to the following graph, presented in Figure 85.

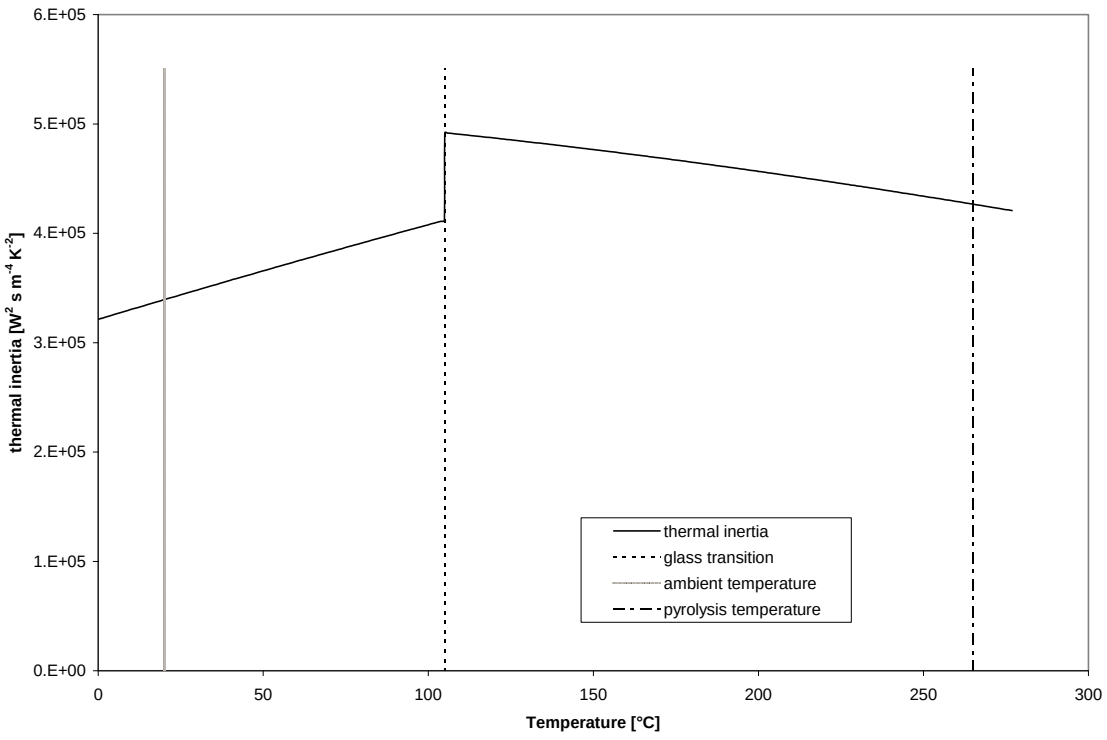

Figure 85 thermal inertia $\lambda\rho c_p$ from the literature

Experimental results

By tracking the history of the surface temperature and using Equation (41) it is possible to follow the evolution of the global thermal inertia over time.

$$\left(\lambda\rho c_p\right)_j = \left(\frac{2}{\sqrt{\pi}}\frac{a}{}\frac{\sqrt{t_j}\ \dot{q}_i''}{\left(T_j - T_\infty\right)}\right)^2 \tag{144}$$

Where t_j is the time measured from the point of the sample placement in front of the heater, $\left(\lambda\rho c_p\right)_j$ is the measured global thermal inertia up to that point and T_j is the temperature recorded at that point in time. When plotting the $\left(\lambda\rho c_p\right)_j$ versus T_j a typical curve is depicted in the following figure. The accuracy of the low temperature values is not clear since the temperature difference in the initial stages of the heating process are very small therefore tend to magnify the value of the thermal inertia. Thus the comparison will be of a qualitative nature and the specific values should be taken only as a reference.

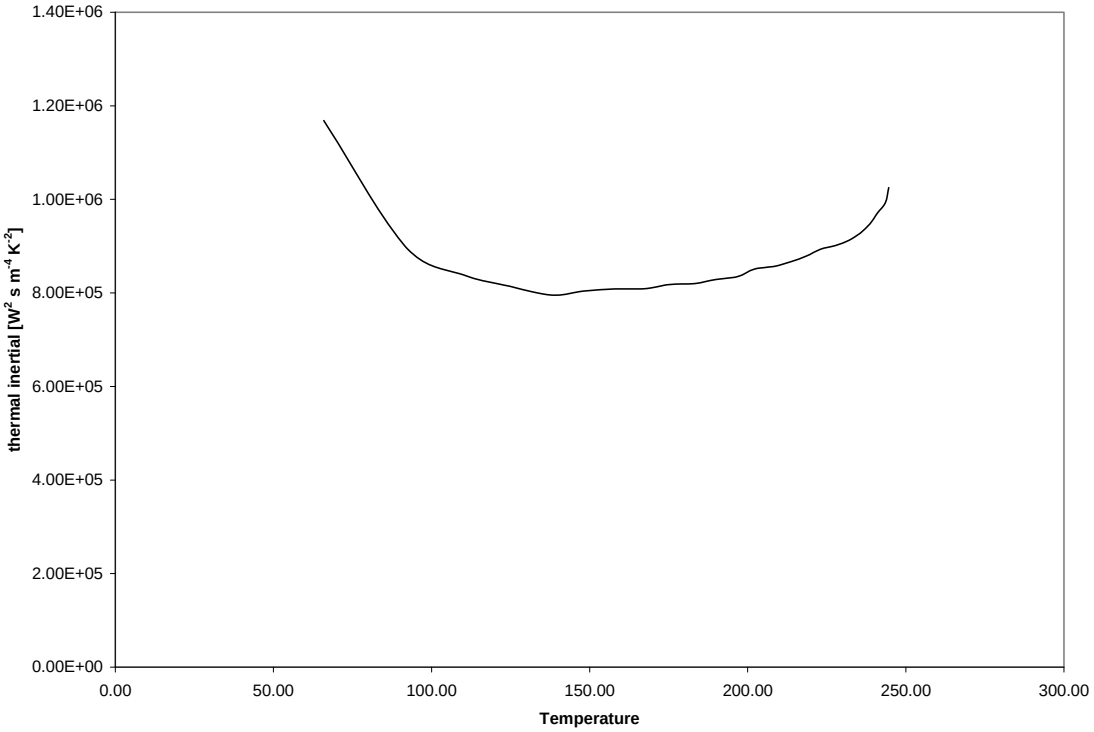

Figure 86 typical $\left(\lambda\rho c_p\right)_j$ versus T_j curve

Literature experimental result comparison

To compare the results form the literature with the results from the experiments conducted here, the following figure presents the thermal inertia from Figure 85 and global thermal inertia Figure 86.

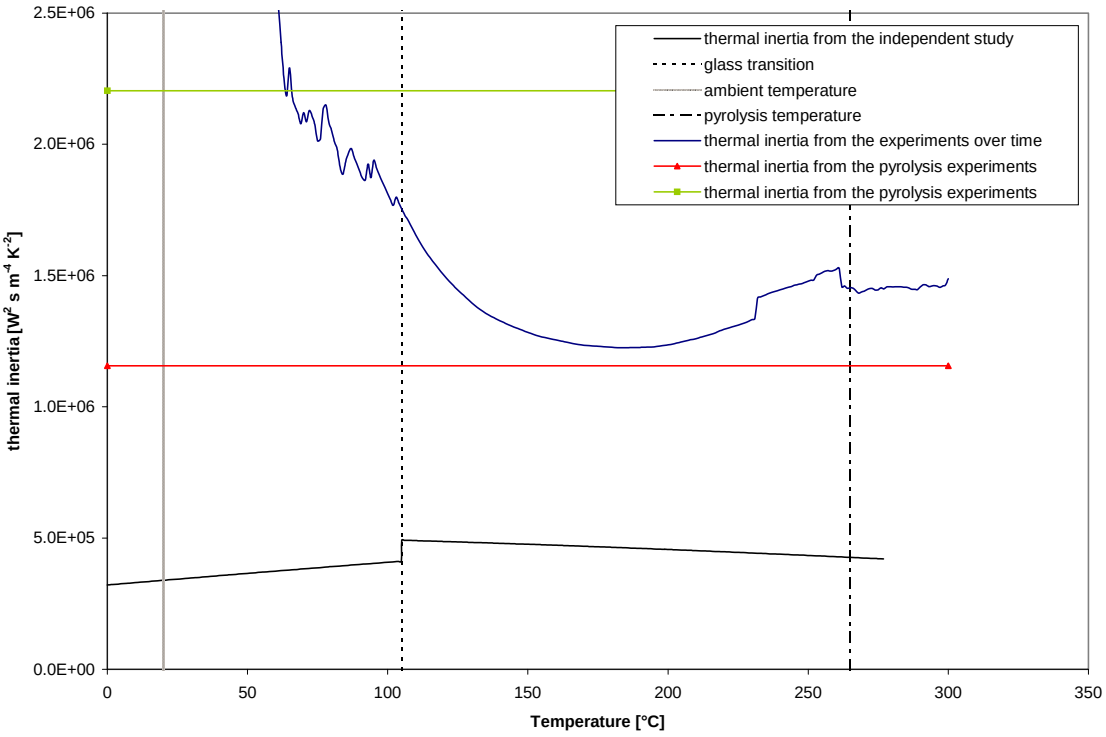

Figure 87 comparative values of the thermal inertia as obtained from global evaluation (literature and present work) and as obtained from the product of the temperature dependent material properties.

The thermal inertia as obtained from pyrolysis tests seems to always be larger than what is predicted from the product of the time dependent functions of the material properties. A further correction can be obtained by including the absorptivity in the determination of the thermal inertia, but still a factor of 2 remains. Proper determination of a global thermal properties by means of a variable property thermal analysis should provide more accurate results but, these will vary between the ranges presented by the bottom curve of Figure 88, thus never match those values obtained from the ignition tests.

6. Conclusions

The main objective of this work was to validate the determination of the thermal inertia, $\lambda\rho c_p$, by means of the LIFT methodology. Three different means were thought to independently obtain the thermal inertia, by the use of the time to ignition t_{ig} (LIFT methodology), from the time to pyrolysis t_p and by independent determination of each property as a function of temperature (thermal conductivity λ, density ρ and specific heat c_p). In this work it was determined, that the three approaches determined three different values, from which the following conclusions can be drawn.

- From the determination of time to ignition t_{ig} and time to pyrolysis t_p two different values for the global thermal inertia $\lambda\rho c_p$ were calculated. Although different values were obtained, it was possible to correlate the time to pyrolysis t_p with the time to ignition t_{ig} by means of a mixing time, t_m.
- The time difference between the onset of pyrolysis t_p and ignition t_{ig} was observed to be dependant on the incident heat flux $\dot{q}_i''$ and revealed a minimum fuel mass fraction $Y_{f,L}$ for ignition. In contrast with previous work, this mass fraction shows a linear dependency with the incident heat flux $\dot{q}_i''$.
- The source of this linear dependency seems to be the definition of the pyrolysis time. Discrepancy between the onset of detectable mass loss and the first

- No correlation could be found between the time to pyrolysis t_p or ignition t_{ig} and the independent determination of the fuel properties. The value of $\lambda\rho c_p$ obtained following the LIFT methodology was consistently larger than that predicted by independent evaluation of the fuel properties. The over prediction was generally of a factor of two, therefore could not be explained by using correct radiative properties. Further work needs to be conducted to fully explain this phenomena.

References

AlMa-71 Alvares, N., J.; Martin, S., B.
Thirteenth Symposium (International) on Combustion
The Combustion Institute, 905-914 (1971)

AndD-66 Anderson, D., R.
Thermal Conductivity of Polymers
Chemical Reviews 66, 667-690 (1966)

AUON-97 Agari, Y.; Ueda, A.; Omura, Y.; Nagai, S.
Thermal diffusivity and conductivity of PMMA/PC blends
Polymer, Vol. 38, 4 (1997)

BaGr-92 Babrauskas, V.; Grayson, S., J.
Heat Release in Fires
Elsvier Applied Science (1992)

BaWu-73 Bares, V.; Wunderlich,B.
Heat capacity of molten polymers.
Journal of Polymer Science Polymer Physics, Ed. 11, 861 (1973)

BeeH-92 Beer, H.
Verlesung Thermodynamik !, II, III
Fachgebiet Technische Thermodynamik, Technische Hochschule Darmstadt (1992)

BejA-84 Bejan, A.
Convection Heat Transfer
John Wiley and Sons (1984)

BolW-48 Bolles, W., L.
Measurement of Gas Temperatures by means of thermocouple
Petroleum Refiner, 27, 2 (1948)

BrIm-89 Brandrup, J.; Immergut, E., H.
Polymer Handbook, 3rd ed.
John Wiley & Sons, New York (1989)

BrSe-79 Bronstein, I., N.; Semendjajew, K., A.
Taschenbuch der Mathematik

BSB B. G. Teubner Verlagsgesellschaft, Leibzig and Nauka Verlag, Moskau, 24 (1979)

CaJa-76 Carslaw, H., S.; Jager, J., C.
Conduction of Heat in Solids
Clarendon Press Oxford (1976)

CreH-93 Creel, H.
Trends in Polymer Science, 1(11), 366-342 (1993)

DanG-68 Daniels, G., E.
Measurement of Gas Temperature and the radiation Compensating Thermocouple
Journal of applied Meteorology, 7, 1026-1035 (1968)

DryD-85 Drysdale, D.
An Introduction to Fire Dynamics
John Wiley & Sons Ltd. (1985)

EieK-61 Eiermann, K.
Kunststoffe 51, 512 (1961)

EieK-64a Eiermann, K.
Modellmäßige Deutung de Wärmeleitfähigkeit von Hochpolymeren Teil 1: Amorphe Hochpolymere
Kolloid-Zeitschrift & Zeitschrift für Polymere 198, 5-16 (1964)

EieK-64b Eiermann, K.
Modellmäßige Deutung de Wärmeleitfähigkeit von Hochpolymeren Teil 2: Verstreckte amorphe Hochpolymere
Kolloid-Zeitschrift & Zeitschrift für Polymere 199, 125-128 (1964)

EieK-64c Eiermann K.
Dissertation at the Technische Hochschule Darmstadt
Bestimmung und modellmäßige Deutung der Wärmeleitfähigkeit von Hochpolymeren.
Published: Journal of Polymer Science, C6 (1964)

EieK-65 Eiermann, K.
Wärmeleitfähigkeit von Kunststoffen in festem und geschmolzenem Zustand
Kunststoffe 55, 335 (1965)

EPIX-96 EPIX, Inc.
User's Manual PIXCI Revision 0.1

EPIX, Incorporated, 26 April (1996)

FaeG-89 Faeth, G.
Closing Remarks
Space Station Freedom Modular Combustion Facility Assessment Workshop, NASA LeRC, Cleveland, OH, MAY (1989)

FerA-95 Fernandez-Pello, A., C.
Combustion Fundamentals of Fire, Chapter2, The Solid Phase , Academic Press Limited (1995)

FHSL-3 Fernandez-Pello, A., C.; Hasega wa, H.; Staggs, K.; Lipska-Quin, A.; Alvares, N., J.
Fire Safety Science – Third International Symposium, 237

GaWW-82 Gaur, U.; Lau, S.; Wund erlich, B., B.; Wunderlich, B.
Heat capacity and other thermodynamic properties of linear macromolecules. VI. Acrylic polymers.
Journal of Physical and Chemical Reference Data, 11, 4, (1982)

GlSS-56 Glawe, G., E.; Simmons, F., S.; Stickney, T., M.
Radiation and recovery corrections and time constants of several chromel-alumel thermocouple probes in high-temperature, high-velocity gas streams
National Advisory Committee for Aeronautics, Technical Note 3766, October (1956)

GodK-92 Godovsky, Y., K.
Thermophysical properties of polymers
Springer-Verlag, Berlin Heidelberg New York London Paris Tokyo Hnog Kong Barcelona Budapest (1992)

HalJ-71 Hallman, J., R.
Ignition Characteristics of Plastics and Rubber
Dissertation at the University of Oklahoma, Norman, Oklahoma (1971)

HeHK-63 Hellwege, K.-H.; Hennig, J.; Knappe, W.
Anisotropie der Wärmeausdehnung und Wärmeleitung in einachsig verstreckten amorphen Hochpolymeren
Kolloid-Zeitschrift & Zeitschrift für Polymere 188, 121 (1963)

HoKn-71 Hoffmann, R.; Knappe, W.
Heat capacity of polyacrylates and poly(methacrylates) in the range -180 to +160 degree.

Kolloid-Zeitschrift & Zeitschrift für Polymere, 247, 763 (1971)

HumD-91 Hummer, D., O.
Atlas of Polymer and Plastics Analysis / Atlas der Polymer- und Kunststoffanalyse
Carl Hanser Verlag, Munich and VCH Verlangsgesellschaft mbH, Weinheim (1991)

InDe-96 Incropera, F., P.; DeWitt, D., P.
Fundamentals of Heat and Mass Transfer
John Willey & Sons, 4 (1996)

JalY-80 Jaluria, Y.
Natural Convection Heat and Mass Transfer
Pergamon Press, New York (1980)

JanM-3 Janssens, M.
A Thermal Model for Piloted Ignition of Wood Including Variable Thermophysical Properties
Fire Safety Science – Third International Symposium, 167-176.

JeNC-79 Jeffrey, S., Newman; Paul, A., Croce
A simple aspirated thermocouple for use in fires
Journal of Fire & Flammability, 10, 326-336 October (1979)

KaOm-88 Kashiwagi, T.; Omori, A.
Effects of Thermal Stability and Melt Viscosity of Thermoplastics on Piloted Ignition
22nd International Symposium on Combustion, 1329-1338 (1988)

KhTC-88 Khanna, Y., P.; Taylor, T., J.; Chomin, G.
Poly. Eng. Sci. 28, 1034 (1988)

KIBH-86 Kashiwagi, T.; Inaba, A.; Brown, J., E.; Hatada, K.; Kitayama, T.; Masuda, E.
Effects of Weak Linkages on the Thermal and Oxidative Degradation of Poly(methyl methacrylates)
Macromolecules, 19, 2160-2168 (1986)

KnaW-60 Knappe, W.
Bestimmung der thermischen Kenngrößen schlecht wärmeleitender Stoffe mit Zweiplattenapparatur ohne Schutzring
Zeitschrift für angewandte Physik 12, 508 (1960)

KnaW-71 Knappe, W.

Wärmeleitung in Polymeren
Advanced Polymer Science, 7, 477-535 (1971)

KreD-90 Krevelen van, D., W.
Properties of Polymers
Elsevier Science B.V., Amsterdam, The Netherlands, 3rd Edition (1990)

KWLW-69 Knappe, W.; Lohe, P.; Wutschig, R.
Kettenaufbau und Wärmeleitfähigkeit bei amorphen Linearpolynomen
Die Angewandte Makromolekulare Chemie, 7, 181-193 (1969)

LeRa-67 Rabinovich, I., B.; Lebedev, B., V.
Thermodynamics of vinyl monomers and polymers. IV. Thermodynamic functions of methyl acrylate, methyl methacrylate, methacrylamide, and α-methylene.
Tr. Khim. Tekhnol. 2, 30 (1967)

LeRa-71 Rabinovich, I., B.; Lebedev, B., V.
Heat capacities and thermodynamic functions of methyl methacrylate and poly(methyl methacrylate).
Tr. Khim. Tekhnol. 1971, 8 (1971)

LohP-65 Lohe P.;
Wärmeleitfähigkeit von hochpolymeren Schmelzen
Dissertation Technische Hochschule Darmstadt (1965)

LonR-98 Long, R., T.
An Evaluation of the Lateral Ignition and Flamespread Test for Material Flammability Assesment for Micro-Gravity Environments
Master of Science Theses conducted at the Department of Fire Protection Engineering at the University of Maryland (1998)

LovT-68 Love, T. J.
Radiative Heat Transfer
Merrill Publishing Co., Columbus, Ohio (1968)

LykA-67 Lykov, A., V.
Theory of Thermal Conductivity (in Russian)
Vysshaya Shkola Moscow (1967)

MSFC-98 *Material Selection List for Space hardware Systems*
MSFC-HDBK-527-REV F, 30th September (1998)

NASA-81 *Flammability, Odor, Offgassing, and Compatibility Requirements Test*

Procedures for Materials in Environments that Support Combustion
NASA document No. NHB 8060.1B, Washington, D.C. (1981)

OhVi-91 Ohlemiller, T., J.; Villa, K., M.
Materials Flammability Test Assessment for Space Station Freedom
National institute of Standards and Technology, NISTIR-4591 (1991)

OJKB-64 O'Reilly, J., M.; Karasz, F., E.; Bair, H., E.
Thermodynamic properties of amorphous and crystalline isostatic poly(methyl methacrylate). Thermodynamic properties of amorphous syndiotic and atactic poly(methyl methacrylate).
Bulletin American Physics Society 9, 285 (1964)

OJKF-66 O'Reilly, J., M.; Karasz, F., E.
Specific heat studies of transition and relaxation behavior in polymers.
Journal of Polymer Science, C14, 49 (1966)

ÖziM-80 Özişik, M., N.
Heat Conduction
John Wiley & Sons (1980)

PalH-87 Palmer, H.
Closing Remarks
International Microgravity Combustion Workshop, NASA LeRC, Cleveland, OH, January (1987)

ParW-82 Parker, W., J.
An Assessment of Correlations Between Laboratory and Full Scale Experiments for the FAA Aircraft Fire Safety Program, Part 3: ASTM E84
National Bureau of Standards, NBSIR-82-2564 (1982)

PROA-67 Pavlinov, L., I.; Rabinovich, I., B., Okladnov, N., K.; Arzhakov, S., A.
Heat capacity of copolymers of methacrylate with methacylic acid in the region 25-190°C.
Vysokomolekul. Soedin. Ser. A9, 483 (1967)

QuHa-84 Quintiere, J., G.; Harkleroad, M.
New Concepts for Measuring Flame Spread Properties
NBSIR 84-2943, National Bureau of Standards (1984)

QuHH-86 Quintere, J., G.; Harkleroad, M.; Hasemi, Y.
Wall Flames and Impacts for Upward Flame Spread
Combustion Science and Technology, 48, 191-222 (1986)

QuHW-83 Quintiere, J., G.; Harkleroad, M.; Walton, D.
Measurements of Material Flame Spread Properties
Combustion Science and Technology, 32, 67 (1983)

QuiJ-81 Quintiere, J.G.,
A Simplified Theory for Generalizing Results from a Flame Spread Apparatus
Fire and Materials, 5, 2 (1981)

QuiJ-82 Quintiere, J., G.
An Assesment of Correlations Between Laboratory and Full Scale Experiments for the FAA Aircraft Fire Safety Program, Part 4: Flammability Tests
National Bureau of Standards, NBSIR-82-2525 (1982)

QuIq-94 Quintiere, J., G.; Iqbal, N.
An Approximate Integral Model for the Burning Rate of a Thermoplastic-like Material
Fire and Materials, 18, 89-98 (1994)

RaLe-67a Rabinovich, I., B.; Lebedev, B., V.
Thermodynamics of vinyl monomers and polymers. V. Measurement of heat capacity and a calculation of the thermodynamic functions of poly(methyl acrylate), poly(methyl methacrylate), poly(methylacrylamide), poly(α-methylstyrene) and poly(vinyl alcohol).
Tr. Khim. Tekhnol. 2, 36 (1967)

SaGr-75 Sparrow, E., M.; Gregg, J., L.
Laminar Free Convection from a Vertical Flat Plate
International Journal Heat Mass Transfer, 18, 1323 (1975)

ShSh-62 Shoulberg, R., H.; Shetter, J., A.
The Thermal Conductivity of Poly(methyl Methacrylate)
Journal of Applied Polymer Science, 23, S32 (1962)

SiBo-62 Simha, R.; Boyer, R., F.
Journal of Chemical Physics, 37, 1003 (1962)

SKBK-91 Steckler, D., K.; Kashiwagi, H., R.; Baum, H., R.; Kanemaru, K.
Analytical model for transient gasification of non charring thermoplastic materials
Fire Safety Science Proceedings of the Third International Symposium, ed. By Cox G. and Landford B. 895-904, Elsevier Applied Science, London (1991)

SocI-64 Sochava, I.,V.
Specific heat of poly(methyl methacrylate) and polystyrene at low temperatures.
Vestn. Leningr. Univ. 16, Ser. Fiz. i Khim. 2, 70 (1964)

SoTr-58 Sochava, I.,V.; Trapeznikova, O., N.
International rotation and heat capacity of a few polymers at low temperatures.
Vestn. Leningr. Univ. 13, Ser. Fiz. i Khim. 65 (1958)

SoTr-65 Sochava, I.,V.; Trapeznikova, O., N.
Rotation of methylene groups in poly(methyl methacrylate) at low temperatures.
Vestn. Leningr. Univ. 20, Ser. Fiz. i Khim. 4, 71 (1965)

StKB-3 Steckler, K., D.; Kashiwagi, T.; Baum, H., R.
Analytical Model for Transient Gasification of Noncharring Thermoplastic Materials
Fire Safety Science – Third International Symposium, 895-904

VDRB-87 Vovelle, C.; Delfau, J.; Reuill on, M.; Bransier, J.; Laraqui, N.
Experimental and Numerical Study of the Thermal Degradation of PMMA
Combustion Science and Technology, 53, 187-201 (1987)

WaWa-95 Waggener, W., J.; Warburg, E.
Über die Messung von Flammentemperaturen durch Thermoelemente, insbesondere über die Temperaturen im Bunsen'schen Blaubrenner.
Verhandlungen der Physikalischen Gesellschaft zu Berlin, Sitzung vom 15. November (1895)

WilR-76 Williamson, R., B.
Fire Performance Under Full Scale Test Conditions-A State Transition Model
The Combustion Institute, 1357-1371 (1976)

WuGa-81 Wunderlich, B.; Gaur, U.
Differential scanning calorimetry of flexible, linear macromolecules.
Polymer Division of the American Chemical Society, Preprints 22 (1), 308 (1981)